Delft University of Technology

Pressure-assisted CU sintering for SiC Die-attachment application

Liu, X.

DOI
10.4233/uuid:291baefe-c4b9-46ea-b250-a6c8f4e6ece8

Publication date
2023

Document Version
Final published version

Citation (APA)
Liu, X. (2023). *Pressure-assisted CU sintering for SiC Die-attachment application*. [Dissertation (TU Delft), Microelectronics, Delft University of Technology]. https://doi.org/10.4233/uuid:291baefe-c4b9-46ea-b250-a6c8f4e6ece8

Important note
To cite this publication, please use the final published version (if applicable).
Please check the document version above.

Copyright
Other than for strictly personal use, it is not permitted to download, forward or distribute the text or part of it, without the consent of the author(s) and/or copyright holder(s), unless the work is under an open content license such as Creative Commons.

Takedown policy
Please contact us and provide details if you believe this document breaches copyrights.
We will remove access to the work immediately and investigate your claim.

This work is downloaded from Delft University of Technology.
For technical reasons the number of authors shown on this cover page is limited to a maximum of 10.

PRESSURE-ASSISTED CU SINTERING FOR SIC DIE-ATTACHMENT APPLICATION

PRESSURE-ASSISTED CU SINTERING FOR SIC DIE-ATTACHMENT APPLICATION

Dissertation

for the purpose of obtaining the degree of doctor
at Delft University of Technology
by the authority of the Rector Magnificus prof. dr. ir. T.H.J.J. van der Hagen
chair of the Board for Doctorates
to be defended publicly on
Monday, 30 January 2023 at 12:30 o'clock

by

Xu LIU

Master of Science in Metallurgical Engineering,
RWTH Aachen University, Aachen, Germany,
born in Inner Mongolia, China.

This dissertation has been approved by

Promotor: prof. dr. G.Q. Zhang

Composition of the doctor committee:

Rector Magnificus,	Chairperson
Prof. dr. G.Q. Zhang,	Delft University of Technology, promotor
Prof. dr. H.Y. Ye,	Southern University of Science & Technology, copromotor
Independent members:	
Prof. dr. R. S. W. Lee,	Hong Kong University of Science & Technology
Prof. dr. ir. G. Rietveld,	University of Twente
Prof. dr. R. Ross,	Institute for Science & Development
Prof. dr. ir. W.D. van Driel,	Delft University of Technology
Prof. dr. P. J. French,	Delft University of Technology
Prof. dr. ir. P.M. Sarro,	Delft University of Technology, reserve member

Keywords: Nano Cu Sintering, Silicon Carbide Power Electronics Packaging, Shear Strength, Mechanical Reliability, Static and Dynamic Test, Thermal Conductivity, Nanoindentation, Molecular Dynamics

Printed by: Ipskamp printing

Front & Back: Cover art work of copper element, copper nanoparticles and Cu-sintered SiC die-attachment samples, by Xu Liu. Based on the "Trama A" artwork by Luis Medina©, under his permission.

Copyright © 2023 by X. Liu

All rights reserved. No part of this publication may be reproduced, stored in a retrieval system or transmitted in any form or by any means without the prior permission in writing from the copyright owner. ISBN 978-94-6473-018-0

An electronic version of this dissertation is available at
http://repository.tudelft.nl/.

To my parents and xiazi

CONTENTS

Summary **xi**

Samenvatting **xv**

List of Abbreviations **xix**

1 Introduction **1**
- 1.1 Merits of SiC Material and Device . . . 2
- 1.2 Die Attachment Technologies for Power Electronics Packaging Application . 4
  - 1.2.1 Reflow Soldering . . . 4
  - 1.2.2 Transient Liquid Phase Method . . . 5
  - 1.2.3 Single-Metal Sintering . . . 6
- 1.3 Copper Sintering Technique . . . 8
  - 1.3.1 Material Treatment . . . 8
  - 1.3.2 Paste Formulation and Sintering Process. . . . 10
- 1.4 Challenges and Research Objectives . . . 12
  - 1.4.1 For Atomic-Scale Sintering Mechanism . . . 12
  - 1.4.2 For Cu Particles Treatment Method and Sintering Process Effect . . . 13
  - 1.4.3 For Mechanical, Thermal and Electrical Properties Evaluation 13
  - 1.4.4 For Die-attachment Application of SiC Devices . . . 13
- 1.5 Thesis Outline . . . 14
- References . . . 15

2 Molecular Dynamics Study of Cu NPs Sintering Between Substrates **23**
- 2.1 Introduction . . . 24
- 2.2 Methods . . . 25
  - 2.2.1 Simulation Model . . . 25
  - 2.2.2 Temperature Profile . . . 26
  - 2.2.3 Data Recording and Analyzing Methods . . . 27
- 2.3 Coalescence Kinetics of NPs-Substrates Model . . . 28
  - 2.3.1 Stage I . . . 29
  - 2.3.2 Stage II . . . 32
  - 2.3.3 Stage III . . . 33
- 2.4 Pores Evolution and Rotation Behavior . . . 35
  - 2.4.1 Pores Evolution Between NPs and Substrates . . . 35
  - 2.4.2 Rotation Behavior of NPs Affected by the Substrate . . . 35
- 2.5 Size Effect of NPs on the Sintering Mechanism . . . 38
- 2.6 Conclusion . . . 40
- References . . . 41

3 Die-attach Performance Evaluation and Mechanisms Study of Cu Sintering Technology 45
3.1 Introduction . . . 46
3.2 Materials and Methodologies . . . 46
    3.2.1 Cu Particles and Other Materials . . . 46
    3.2.2 Cu QNPs Treatment and Paste Formulation . . . 47
    3.2.3 The Die-attach Samples and Shear Strength Measurement . . . 47
    3.2.4 Samples for Thermal and Electrical Properties Measurement . . . 49
    3.2.5 Thermal Conductivity Measurement Method . . . 49
    3.2.6 Electrical Resistivity Measurement Method . . . 50
3.3 Characterization of Cu QNPs and Cu Paste . . . 51
    3.3.1 SEM, TEM and XRD Characterization of the Cu QNPs . . . 51
    3.3.2 FT-IR Spectroscopy of the Cu QNPs . . . 53
    3.3.3 TG/DSC Characterization of the Cu NPs . . . 53
    3.3.4 TG/DSC Characterization of the Cu Paste . . . 54
3.4 Study on The Effects of Process Parameters on the Key Properties . . . 55
    3.4.1 Thermal and Electrical Properties . . . 55
    3.4.2 Shear Strength . . . 56
3.5 Effects of Process Parameters on the Evolution of Microstructure . . . 58
    3.5.1 Fracture Mode . . . 58
    3.5.2 Interface Evolution . . . 63
    3.5.3 Bonding Mechanism . . . 66
3.6 Conclusion . . . 68
References . . . 69

4 Mechanical Properties and Creep Behavior of Cu Sintered Material 73
4.1 Introduction . . . 74
4.2 Methodology . . . 75
    4.2.1 Sample Preparation . . . 75
    4.2.2 Nanoindentation Test and Displacement-load Curve . . . 76
    4.2.3 Indentation Hardness and Elastic Modulus Calculation . . . 77
    4.2.4 Constitutive Model . . . 77
    4.2.5 Creep Behavior . . . 78
4.3 Nanoindentation Study at Room Temperature . . . 79
    4.3.1 Effects of Peak Load at Room Temperature . . . 79
    4.3.2 Effects of Loading Rate at Room Temperature . . . 82
    4.3.3 Effect of Sintering Pressure at Room Temperature . . . 83
    4.3.4 Constitutive Modeling Derivation . . . 83
4.4 Nanoindentation Study at High Temperature . . . 85
    4.4.1 Displacement-load Curves at High Temperature . . . 85
    4.4.2 Hardness and Elastic Modulus at High Temperature . . . 86
    4.4.3 Creep Effect at High Temperature . . . 89
4.5 Conclusion . . . 90
References . . . 91

5 Application and Characterization of Cu Sintered SiC Power Modules 95
5.1 Introduction . . . 96
5.2 Methodology . . . 97
5.2.1 Cu-Sintered Cu DA Units. . . . 98
5.2.2 Cu-Sintered SiC DA Units . . . 98
5.2.3 Cu-Sintered SiC Power Modules . . . 99
5.3 TCT and HTS Reliability of Shear Strength . . . 100
5.4 HTS Reliability of R_{DSon}. . . . 102
5.5 TCT Reliability of R_{th} . . . 103
5.6 Static and Dynamic Test of SiC Power Modules . . . 106
5.6.1 Static Test (I-V Characteristics) of SiC Power Modules . . . 106
5.6.2 Dynamic Test of SiC Power Modules . . . 107
5.7 Conclusion . . . 110
References . . . 110

6 Conclusions and Recommendations 115
6.1 Conclusions. . . . 115
6.2 Recommendations in Future Works . . . 118

A Supporting Information Chapter 2 119
References . . . 122

B Supporting Information Chapter 3 125

C Supporting Information Chapter 4 129

D Supporting Information Chapter 5 131

Acknowledgements 133

Curriculum Vitæ 137

List of Publications 139

SUMMARY

TYPICAL wide bandgap (WBG) semiconductor materials such as silicon carbide (SiC) and gallium nitride (GaN) contain larger bandgap, higher critical electric field and higher thermal conductivity than silicon (Si). These features ensure that power devices operate at much higher power levels (> 100MW), faster switching speed (> 100 kHz), and higher temperatures (> 300°C). However, the increased performance on the chip side has also led to higher requirements for package structures and materials. To support the stable performance of power chips under harsh conditions, the high-temperature reliability of die-attach materials is also critical. In recent years, copper sintering has emerged as one of the most promising solutions in the industry due to its excellent material properties. However, until now, academic and industrial research on copper sintering is still in its infancy. Therefore, a systematic study of copper sintering technology in combination with materials, processes, simulations, applications and tests is of great importance in promoting the industrial application of this technology.

In this dissertation, firstly, a molecular dynamic (MD) simulation was carried out to study the coalescence kinetics and microstructure evolution of Cu nanoparticles sintering between two substrates at low temperatures. A sandwich structure model with two substrates and multiple particles in between was constructed to simulate the real die-attach structure. The crystal structure, atomic diffusion, dislocation behavior and porous defects were studied by using OVITO tools, MSD curves, CNA and DXA analysis. It was found that the dominant sintering mechanism for the particles without applied pressure, the sintering mechanism at low temperatures was mainly surface diffusion. However, when the pressure effect of the upper substrate on the particles was introduced, the dominant sintering mechanism of the particles changed to plastic flow induced by dislocation production and motion in the particles. In addition, the spontaneous rotation of particles occurred during the coalescence to eliminate the interparticle lattice mismatch. Meanwhile, the passive rotation behavior of the bottom-layer particles also occurred due to the pinning effect of the substrate. Besides, the pinning effect of the substrate also caused giant pores between particles and substrates. Some of these pores can be filled via both plastic deformation and surface diffusion of atoms for the smaller particles. Finally, to investigate the size effect on the sintering kinetics, the atomic motion and microstructural evolution of 3 nm, 4 nm and 5 nm models were compared. It was found that the models of smaller size particles typically contained higher shrinkage ratios, larger sintering necks and smaller pores. More severe atomic motion and more drastic crystal structure transitions at each stage were found in smaller size particles. The research results show that the sintering densification and pores structure can be improved by using the applied pressure in the sintering process. Particle sintering progress is greatly accelerated by enhancing the plastic flow mechanism. However, attention should also be paid to the problems such as rotational residual stresses brought about by the pinning effect of the substrate, which may require further heat treatment to

eliminate.

In the next chapter, a self-developed Cu paste was fabricated with predefined printing, and drying workability. A reductive pretreatment was conducted in advance to the raw Cu particles to remove the original oxidation. Then, laser flash measurements and four-probe measurements were carried out on the Cu sintered sample prepared by various temperatures, pressure and time, to evaluate the impact of the sintering process parameters on thermal and electrical properties. It was found that when the sintering process was at 250°C and 10 MPa with only 1 minute, the thermal (5.82 W/m·K) and electrical conductivity (0.003 /($\mu\Omega$·cm)) of the sample is extremely small and cannot satisfy the semiconductor packaging requirements. Increasing the sintering time to 4 minutes can effectively improve the conductivity characteristics to 231.15 W/m·K and 0.255 /($\mu\Omega$·cm). There is a similar trend for the effect of temperature. From 210°C to 270°C, both properties are improved from 126.53 W/m·K and 0.124 /($\mu\Omega$·cm) to 272.87 W/m·K and 0.282 /($\mu\Omega$·cm). Among them, however, the effect of pressure is minimal. Then, in order to evaluate the impact of the Cu sintering process parameters on the joining performance and microstructure evolution of the die-attach samples, the shear test was conducted. It was also found that sintering temperature between 210°C and 230°C, or assisted pressure less than 10 MPa could provide bonding strength of around 30 MPa. Such low strength is due to both the partially burnt-out of organics and incomplete Cu particles sintering. By increasing pressure to 20 MPa and 30 MPa, it shows the enhanced die shear strength of 100.1 MPa and 116 MPa, accomplished with a sintering temperature of 250°C for 3 min. When increased temperature to 270°C, the shear strength was further enhanced to over 120 MPa. Moreover, time can insignificantly affect the microstructure and bonding strength in less than 4 min. Material microstructural characterization demonstrates that high bonding is coming from the positive effect of pressure and temperature on promoting the necking growth, sintering networking formation, pores isolation and brittle-ductile fracture transition. Considering the small improvement effect by further increasing of temperature and pressure, 250°C/3 min/20 MPa process recipe is well recommended for the application.

Next, in order to verify the robustness of this technique for application in die attachment processes, key mechanical properties such as indentation hardness, elastic modulus and creep behavior of Cu-sintered samples were evaluated separately. First of all, the peak load (from 10 mN to 150 mN) and loading rate (from 0.1 mN/s to 1.5 mN/s) effect on the indentation hardness and elastic modulus were investigated. The indentation size effect was found to be evident when the indentation depth was below 500 nm and the corresponding peak load was less than 10 mN. But after 70 mN of peak load (1500 nm of maximum depth), the changing trend was no more evident. Loading rate had a similar effect on these parameters. As it increased from 0.1 mN/s to 0.9 mN/s, both the indentation hardness and the elastic modulus gradually increased as well. But from 0.9 mN/s, the two properties started to become stable at around 1.59 ± 0.154 GPa and 99.5 ± 0.86 GPa. The potential causes were mainly work hardening effect, pores densification, and pile-up phenomena during the indentation test. Therefore, to ensure stable experimental results, an indentation depth of more than 1500 nm and a loading rate over 0.9 mN/s are necessary. By using the stable testing parameters, the constitutive models (yield stress, strain hardening exponent factors) for samples sintered via different

applied pressure were obtained, which can be used to describe the room-temperature mechanical properties of the Cu sintered joint. Next, the effects of temperature ranging from 150°C to 240°C on the indentation hardness and elastic modulus were investigated. The temperature dependence of both parameters was fitted to account for this effect. In addition, the creep behavior including the initial creep curves was studied and compared for samples sintered with different applied pressures. Higher testing temperatures were found to result in more severe creep deformations. However, higher sintering pressure can effectively improve the creep resistance against plastic deformation. But the increasing effect comes to a marginal over 20 MPa, which provides a hint to the selection of the sintering process parameters in practice.

Finally, a pressure-assisted Cu sintering die-attachment process (250°C/3 min/20 MPa) was adopted to prepare die-attach units and several SiC power modules. For the power module, the packaging process was conducted on an industrial standard packaging production line. The shear strength, R_{DSon} and thermal resistance reliability was investigated through 150°C/1000 hours high temperature storage test and -40°C~150°C /1000 cycles thermal cycling test. Then, the static and dynamic tests of the Cu-sintered SiC module were conducted. As a benchmark, the same SiC module that was die-attached by Ag sintering process was set in parallel. The experimental results indicated that both of the output characteristics switching performance of Cu-sintered SiC module are at the same level as Ag-sintered module did and consistent with the standard commercial one. Considering the comprehensive cost-performance balance, the presented Cu sintering technology is quite promising for WBG power electronics packaging application. At the end of the thesis, the main conclusions and contributions are summarized, and the outlook for future work in this field is proposed.

SAMENVATTING

Typische Halfgeleidermaterialen met brede bandkloof (WBG) zoals siliciumcarbide (SiC) en galliumnitride (GaN) hebben een grotere bandkloof, een hoger kritisch elektrisch veld en een hoger warmtegeleidingsvermogen dan silicium (Si). Deze eigenschappen kunnen ervoor zorgen dat vermogensapparaten werken bij veel hogere vermogensniveaus (> 100MW), een hogere schakelsnelheid (> 100 kHz) en een hogere temperatuur (> 300^{circ}C). Om de stabiele prestaties van vermogenselektronica te ondersteunen in omstandigheden met een hoog vermogen, is de betrouwbaarheid bij hoge temperatuur van het materiaal van de matrijsbevestiging van cruciaal belang. In de afgelopen jaren is kopersintering naar voren gekomen als een van de meest veelbelovende oplossingen in de industrie vanwege de potentiële voordelen van hoge-temperatuureigenschappen. Tot nu toe stond de studie van kopersintering echter nog in de kinderschoenen in de academie en in de industrie. Daarom is een systematische studie van kopersinteringstechnieken in combinatie met materialen, proces, simulatie, toepassingen en testen van groot belang om de toepassing van deze techniek in industriële toepassingen te stimuleren.

In dit proefschrift werd eerst een moleculair dynamische (MD) simulatie uitgevoerd om de coalescentiekinetiek en microstructuurevolutie van Cu-nanopartikels die bij lage temperatuur tussen twee substraten sinteren te bestuderen. Een sandwichstructuurmodel met twee substraten en meerdere deeltjes ertussen werd geconstrueerd om de echte die-attach structuur te simuleren. De kristalstructuur, atoomdiffusie, dislocatiegedrag en poreuze defecten werden bestudeerd met behulp van OVITO, MSD-curven, CNA en DXA-analyse. Het bleek dat de dominante sintermechanismen voor de deeltjes zonder toegepaste druk, het sintermechanisme bij lage temperatuur voornamelijk oppervlaktediffusie was. Wanneer echter het drukeffect van het bovenste substraat op de deeltjes werd ingevoerd, verandert het dominante sintermechanisme van de deeltjes in plastische stroming, veroorzaakt door dislocatieproductie en beweging in de deeltjes. Bovendien kwam de spontane rotatie van de deeltjes voor tijdens de coalescentie om de slechte afstemming tussen de deeltjesroosters te elimineren. Ondertussen kwam het passieve rotatiegedrag van de L3-deeltjes ook voor door het pinning-effect van het substraat. Bovendien veroorzaakte het pinning-effect van het substraat ook reusachtige poriën tussen de deeltjes en het substraat. Sommige van deze poriën kunnen worden gevuld via zowel plastische vervorming als oppervlaktediffusie van atomen voor de kleinere deeltjes. Om het grootte-effect op de sinterkinetiek te onderzoeken, werden ten slotte de atoombeweging en de microstructuurevolutie van modellen van 3 nm, 4 nm en 5 nm vergeleken. Het bleek dat de modellen van kleinere deeltjes doorgaans hogere krimpverhoudingen, grotere sinterhalzen en kleinere poriën bevatten. Bij kleinere deeltjes werd een sterkere atomaire beweging en drastischer kristalstructuurovergangen in elk stadium gevonden.

In het volgende hoofdstuk werd een zelfontwikkelde Cu-pasta gefabriceerd met vooraf gedefinieerde bedrukking, droging en sintering. Er werd vooraf een reductieve voorbehandeling uitgevoerd op de ruwe Cu-deeltjes om de oorspronkelijke oxidatie te verwijderen. Vervolgens werden laserflitsmetingen en metingen met vier sondes uitgevoerd op het Cu-gesinterde monster, bereid door verschillende temperaturen, druk en tijd, om de impact van de parameters van het sinterproces op thermische en elektrische eigenschappen te evalueren. Er werd vastgesteld dat met slechts 1 minuut sinterproces de thermische (5,82 W/m·K) en elektrische geleidbaarheid (0,003/($\mu\Omega$·cm)) van het monster extreem klein is en niet kan voldoen aan de eisen aan de verpakking van halfgeleiders. Door de sintertijd tot 4 minuten te verlengen, kunnen de geleidbaarheidskenmerken effectief worden verbeterd tot 231,15 W/m·K en 0,255/($\mu\Omega$·cm). Er is een vergelijkbare trend voor het effect van temperatuur. Van 210°C tot 270°C zijn beide eigenschappen verbeterd van 126,53 W/m·K met 0,124/($\mu\Omega$·cm) tot 272,87 W/m·K met 0,282/($\mu\Omega$ ·cm). Onder hen is het effect van druk echter minimaal. Om vervolgens de impact van de Cu-sinterprocesparameters op de verbindingsprestaties en microstructuurevolutie van de matrijs-attach-monsters te evalueren, werd de afschuiftest uitgevoerd met verschillende sintertemperaturen, druk en tijd. Er werd ook gevonden dat een sintertemperatuur tussen 210°C en 230°C, ofeen geassisteerde druk van minder dan 10 MPa, een hechtsterkte van ongeveer 30 MPa kon verschaffen. Een dergelijke lage sterkte is te wijten aan zowel het gedeeltelijk uitgebrande organische materiaal als het onvolledige sinteren van Cu-deeltjes. Door de druk te verhogen tot 20 MPa en 30 MPa, vertoont het de verbeterde afschuifsterkte van de matrijs van 100,1 MPa en 116 MPa, bereikt met een sintertemperatuur van 250°C gedurende 3 minuten. Wanneer de temperatuur werd verhoogd tot 270°C, werd de afschuifsterkte extreem verbeterd tot meer dan 120 MPa. Bovendien kan tijd de microstructuur en hechtsterkte in minder dan 4 minuten onbeduidend beïnvloeden. Microstructurele materiaalkarakterisering toont aan dat een hoge hechting het gevolg is van het positieve effect van druk en temperatuur op het bevorderen van de insnoeringgroei, de vorming van sinternetwerken, poriënisolatie en bros-ductiele breukovergang. Gezien het kleine verbeteringseffect door verdere verhoging van temperatuur en druk, wordt het procesrecept van 250°C/3 min/20 MPa goed aanbevolen voor de toepassing.

Vervolgens worden de belangrijkste mechanische eigenschappen zoals indrukkinghardheid, elasticiteitsmodulus en kruipsnelheid van Cu gesinterde monsters afzonderlijk geëvalueerd om de haalbaarheid van deze techniek voor toepassing in matrijsbevestigingsprocessen te verifiëren. Eerst werd het effect van de piekbelasting (van 10 mN tot 150 mN) en de belastingssnelheid (van 0,1 mN/s tot 1,5 mN/s) op de indrukkinghardheid en de elasticiteitsmodulus onderzocht. De geteste verplaatsing-belastingskrommen werden gebruikt om de elastisch-plastische eigenschappen te analyseren en deze belangrijke mechanische parameters te berekenen. De ISE blijkt duidelijk wanneer de indrukkingdiepte minder dan 500 nm is en de overeenkomstige piekbelasting minder dan 10 mN bedraagt. Maar na 70 mN piekbelasting (1500 nm maximale diepte) is de veranderende trend niet meer duidelijk. De belastingssnelheid heeft een vergelijkbaar effect op deze parameters. Naarmate deze toeneemt van 0,1 mN/s tot 0,9 mN/s, nemen zowel de indrukkinghardheid als de elasticiteitsmodulus geleidelijk toe. Maar vanaf 0,9 mN/s beginnen de twee eigenschappen stabiel te worden rond 1,59 ± 0,154 GPa en 99,5 ± 0,86 GPa. De mogelijke oorzaken zijn voornamelijk het uithardingseffect, poriënverdichting en stapelverschijnselen tijdens de indrukkingstest. Om stabiele experimentele resultaten te verkrijgen zijn daarom een indrukdiepte van meer dan 1500 nm en een belastingssnelheid van meer dan 0,9 mN/s noodzakelijk. Door gebruik te maken van de stabiele testparameters werden de constitutieve modellen (vloeispanning, de exponent van de deformatieharding) voor monsters die onder verschillende toegepaste druk werden gesinterd, verkregen, die kunnen worden gebruikt om de mechanische eigenschappen bij kamertemperatuur van de Cu-sinterverbinding te beschrijven. Vervolgens werden de effecten van de temperatuur van 150 tot 240°C op de indrukkinghardheid en de elasticiteitsmodulus onderzocht. De temperatuurafhankelijkheid van beide parameters werd aangepast om dit effect te verklaren. Bovendien werd het kruipgedrag, inclusief de kruipreksnelheid in stationaire toestand, bestudeerd en vergeleken voor monsters die werden gesinterd met verschillende toegepaste drukken. Hogere temperaturen bleken te resulteren in ernstigere kruipvervormingen. Een hogere sinterdruk kan echter de kruipweerstand tegen plastische vervorming effectief verbeteren. Het toenemende effect is echter marginaal boven 20 MPa, hetgeen een aanwijzing is voor de praktische keuze van de sinterprocesparameters.

Tenslotte werd een drukgesteund Cu-sinterproces (250°C/3 min/20 MPa) toegepast om die-attach-eenheden en verscheidene SiC-vermogensmodules te bereiden. Voor de vermogensmodule werd het verpakkingsproces uitgevoerd op een industriële standaard verpakkingslijn. De afschuifsterkte, R_{DSon} en de betrouwbaarheid van de thermische weerstand werden onderzocht aan de hand van een opslagtest bij hoge temperatuur van 150°C/1000 uur en een thermische cyclustest bij -40°C~150°C /1000 cycli. Dan, werden de statische en dynamische tests van Cu-gesinterde SiC module uitgevoerd. Als benchmark, werd een zelfde SiC module die door Ag-sintering proces werd die-vastgemaakt parallel geplaatst. De experimentele resultaten gaven aan dat zowel de uitgangskenmerken als de schakelprestaties van de Cu-sintered SiC module op hetzelfde niveau liggen als de Ag-sintered module en overeenkomen met de standaard commerciële module. Gezien de uitgebreide kosten-prestatie balans, de gepresenteerde Cu sinteren technologie is veelbelovend voor WBG vermogenselektronica verpakking toepassing. Aan het einde van het proefschrift worden de belangrijkste conclusies en bijdragen samengevat, en de vooruitzichten voor toekomstig werk op dit gebied worden voorgesteld.

LIST OF ABBREVIATIONS

α	Thermal diffusion coefficient
A_C	Project area of the contact surface, for hardness measurement
a_{fcc}	Lattice constant of the FCC (face-centered cubic)
AMB	Active metal brazing
B	Temperature sensitivity factor of hardness
C	Indentation curvature
CNA	Common Neighbor Analysis
c_p	Specific heat capacity
CTE	Coefficient of thermal expansion
D	Sample diameter, for resistivity measurement
DA	Die-attachment
DBC	Direct bonded copper
DPT	Double pulse test
DSC	Differential scanning calorimetry
DUT	Device under testing
DXA	Dislocation Extraction Algorithm
e	Temperature sensitivity factor of elastic modulus
E	Elastic modulus
EAM	Embedded atom method

EDS	Energy disperse spectroscopy
E_i	Elastic modulus for the Berkovich indenter, 1140 GPa
EG	Ethylene glycol
E_{off}	Turn-OFF loss
E_{on}	Turn-ON loss
E_r	Reduced elastic modulus
ETM	Electrical test method
FCC	Face-centered cubic
$F_{(D/S)}$	Sample diameter correction factor
$F_{(W/S)}$	Sample thickness correction factor
F_{max}	Peak load in the nanoindentation test
FT-IR	Fourier transformed infrared
GaN	Gallium nitride
H	Specimen thickness, for calculation
H	Indentation hardness
HCP	Hexagonal close-packed
h_c	Contact depth, for the indentation hardness measurement
h_{max}	Maximum indention depth, for the indentation hardness measurement
h_r	Residual depth, for the indentation hardness measurement
HTP	High melting-temperature phase
HTS	High temperature storage
IGBT	Insulated Gate Bipolar Transistor
I_H	Heating current
I_M	Measurement current

λ	Thermal conductivity
K factor	Temperature sensitivity parameter, TSP
LTP	Low melting-temperature phase
IMC	Intermetallic compounds
LAMMPS	Large-scale Atomic Molecular Massively Parallel Simulator
MD	Molecular dynamics
MOSFET	Metal-Oxide-Semiconductor Field-Effect Transistor
MSD	Mean-squared displacement, <d^2 >
N	Number of atoms
Nv	Number of vacancies
v	Poisson ratio
v_i	Poisson ratio for the Berkovich indenter, 0.07
n	Work hardening coefficient
NPs	Nanoparticles
OFC	Oxide-free copper
OM	Optical microscope
ρ	Density of the sample, g/cm^3, $for \lambda$ measurement
ρ_0	Density of the liquid, g/cm^3, $for \lambda$ measurement
ρ_{air}	Density of the air (0.0012 g/cm^3), $for \lambda$ measurement
PC	Power cycling
PVD	Physical vapor deposition
Q	Activation energy required for vacancy generation
QNPs	Quasi-nanoparticles
r$_{com}$	Centroid coordinates of the particle

r_{cut}	Cutoff radius
R	Resistivity
R	Universal gas constant
R_{DSon}	Drain-source on-state resistance
R_{th}	Thermal resistance
$\mathrm{R}_{th(jc)}$	Junction-to-case thermal resistance
S	Probe spacing, for resistivity measurement
S	Stiffness of the contact, the initial slope of the unloading curve
SAC	Sn-Ag-Cu
SEM	Scanning electron microscope
SF	Stacking fault
Si	Silicon
SiC	Silicon carbide
σ	Shear strength
σ	Stress
σ_y	Yield strength
$\sigma_{0.29}$	Characteristic stress when strain is 0.29
SLID	Solid-liquid interdiffusion
T	Temperature
TCT	Thermal cycling test
TEM	Transmission electron microscope
TGA	Thermogravimetric analysis
TIM	Thermal interface material
T_j	Junction temperature

TLPB	Transient liquid phase bonding
TLPS	Transient liquid phase sintering
$T_{melting}$	Melting temperature
$T_{process}$	Process temperature
TS	Thermal shock
TSP	Temperature sensitivity parameter, K factor
t_0	Initial time
$t_{1/2}$	The time required for the backside temperature to reach half of the maximum value
V_{DS}	Drain-source voltage
V_{GS}	Gate-source voltage
$V_{GS(th)}$	Threshold voltage
W	Sample thickness, for resistivity measurement
WB	Wire bonding
WBG	Wide bandgap
XRD	X-ray diffraction
XPS	X-ray photoelectron spectroscopy
Y	Strength coefficient
ϵ	Total strain
ϵ_p	Actual plastic strain
ϵ_y	Yield strain
$\epsilon_{0.29}$	Characteristic strain
Z_{th}	Transient thermal resistance
ζ_x	Shrinkage ratio

1

INTRODUCTION

In recent centuries, excessive emission of greenhouse gases has been causing long-term, severe and pervasive influence on human beings and ecosystems [1]. It has been realized that shifting to a low-carbon economy on a global scale is necessary for sustainable development for each country[2]. Over the decades, the share of electricity in the world's final energy consumption has steadily risen with the development of electrification applications such as electric cars, high-speed rail, smart grids and photovoltaics. By 2040, Electrical energy is estimated to account for more than 40% of the rise in final energy consumption[3]. Therefore, improving the efficiency of electrical energy utilization and conversion is key in the economic transformation process. In this context, power electronics technology is becoming increasingly relevant. A power electronics device is a greatly integrated solid-state semiconductor electronics being employed to control and converse the high-power electric power to the demanding form for end user [4]. Thanks to the outstanding properties of wide bandgap (WBG) semiconductors, the performance and efficiency of power devices could be further expanded when the conventional Si-based device reaches its physical limits.

1.1. MERITS OF SIC MATERIAL AND DEVICE

As one of the most representative WBG semiconductor materials, silicon carbide (SiC) has larger band gap, higher critical electric field and higher thermal conductivity compared with silicon (Si)[5]. As shown in Fig.1.1a and b, these properties are particularly vital for allowing power devices to operate at considerably high-power levels and high-temperature conditions with high-efficiency [6]–[8]. Additionally, it can also help to reduce the size of the power module, which enables a more lightweight and low-cost system.

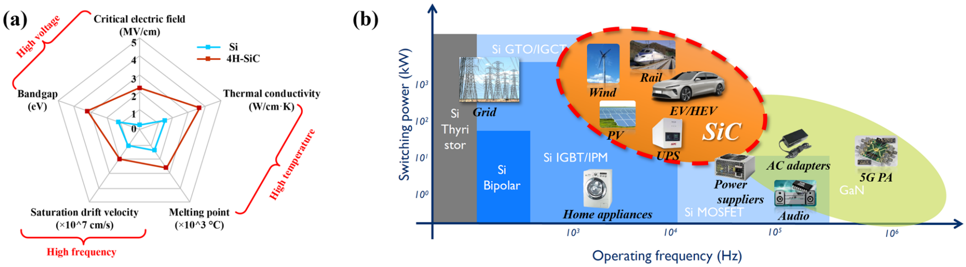

Figure 1.1: (a) Key properties comparison between Si and 4H SiC materials.[5] (b) Typical applications of different power devices. The highlighted region is where SiC power devices show advantages.[9]

In the past, to lower down the driving current and output impedance for the device, the bipolar device Insulated Gate Bipolar Transistor (IGBT) was invented [10]. However, due to the bipolar characteristics, the switching loss during turning on (E_{on}) and turning off (E_{off}) is elevated at high switching speed. In contrast with IGBT modules, SiC Metal-Oxide-Semiconductor Field-Effect Transistor (MOSFET) module can dramatically reduce the total loss by 70% due to its low-loss characteristics [11]–[13], as shown in Fig.1.2a. Such benefit is more pronounced at high temperatures [14], [15]. As a result, SiC MOSFET is more appropriate for medium and high voltage and frequency applications in high-temperature scenarios than Si.

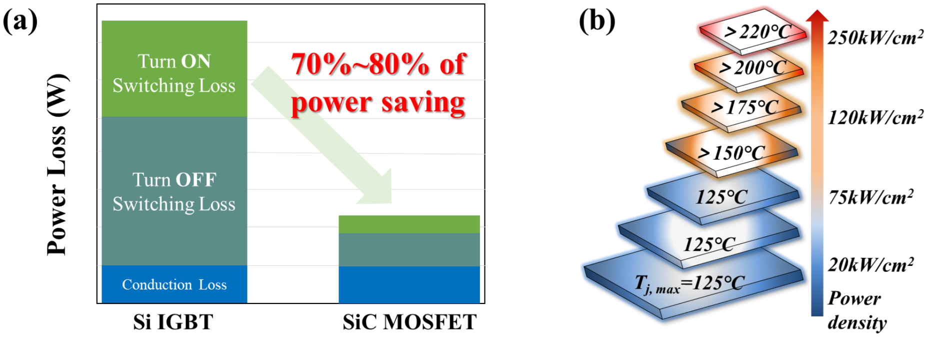

Figure 1.2: (a) Performance advantages of SiC MOSFETS compared with IGBTs at high-speed switching conditions. (b) The schematic diagram for the evolution of chip size, junction temperature and power density for power electronics. [16]

However, as shown in Fig.1.2b, along with the excellent properties of SiC devices comes a reduction in chip size, an increase in power density, and an increase in junction temperature when replacing Si-based devices [17]. This will result in a greater challenge to the reliability of the entire module. Therefore, it is crucial to improve the current carrying and heat dissipation capabilities of the module to ensure superior performance of the SiC devices. This can be achieved through the innovation of packaging materials and technologies.

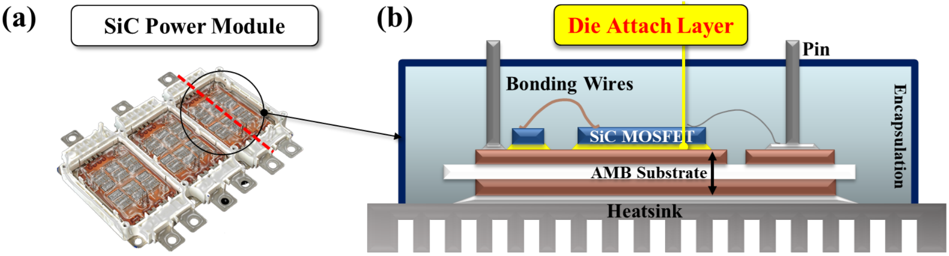

Figure 1.3: (a) A typical power module and (b) the schematic diagrams of the packaging internal structure.

Fig.1.3 shows a photo of a typical power module and a schematic of its internal structure. The materials and techniques used in these components are as follows:

- First, for mechanical supporting, heat dissipation and electricity carrying, the power die are attached onto the power substrate by a die-attachment (DA) layer, as highlighted in Fig.1.3b. Typical techniques applied in this region include reflow soldering, transient liquid phase bonding and sintering depending on the performance and cost requirement.
- The power substrate is a metal-ceramic substrate between the power chip and the heatsink (or sometimes baseplate) for realizing electrical insulation and heat dis-

sipation along the vertical direction. Normally, when considering the cost, the alumina Direct-Bonded-Copper (DBC) substrate is applied, whereas for better thermal conductivity and reliability, silicon nitride Active-Metal-Brazing (AMB) substrate with a thicker copper plate are adopted by the industry recently.
- Then, different power die are interconnected through wire bonds. In general, aluminum wires are used here. For higher reliability, copper wire bonding or clip bonding has also been proposed in recent years.
- Finally, the die-attached substrate is protected by a plastic housing case and encapsulated by silicon gel. There is a heatsink under the module for heat dissipation.

Among all package structures, the DA material is the first layer directly connected to the power chip and hence, it is one of the most critical components that directly affect the performance of the power module. Also, since the power module has to operate under high temperature and power fluctuation conditions, the DA layer will not only transmit a huge amount of heat and electrical signals, but also undergo large thermal stress brought by the power chip and the substrate. Therefore, an in-depth study of DA materials and processes is necessary for both the industry and the academy. In the next section, four of the most commonly used die attachment techniques are reviewed and compared.

1.2. DIE ATTACHMENT TECHNOLOGIES FOR POWER ELECTRONICS PACKAGING APPLICATION

1.2.1. REFLOW SOLDERING

REFLOW soldering is the most widely used method for attaching power devices to substrates. During this process, the soldering paste undergoes melting, flow, and solidification to form metallurgical interconnects with the parts to be connected, as shown in Fig.1.4. The key ingredient for soldering paste is a metallic powder, which can contain different eutectic compositions and thus determine the solidus temperature. High-lead solders (Pb content >85 wt%, for example, 95Pb-5Sn) have been widely used for DA applications for decades due to their reasonably good thermal, electrical and mechanical performance. By the end of the last century, however, the toxicity of lead solder to humans and the environment was realized and investigated. Then from 2000 onwards, the application of lead-based soldering materials was scheduled to be gradually restricted, and lead-free solder alloys became popular as an alternative to electronic packaging.

Various lead-free solder alloys have been developed for different applications. Examples are the Sn-Bi eutectic alloy (139°C), the Sn-Ag eutectic alloy (221°C), and the Sn-Cu eutectic alloy (227°C). The most widely used one is Sn-Ag-Cu (SAC) alloy, which can provide outstanding performance(~60 W/mK) with a low-cost[18]. However, the relatively low remelting temperature limits its application for SiC power module which always operates at a temperature above 175°C, or even 200°C [19].

Au-Sn soldering alloys have higher reflowing temperatures which have been seen as the primary choice of DA materials for high-power LED applications [20]. However, the cost-benefit ratio is questionable given the high cost of eutectic Au-Sn soldering materials. In addition, for all reflow soldering materials, there are always stiff interfacial intermetallic compounds (IMCs). Such high brittleness phase precipitation can lead to inevitable reliability problems [21]. Therefore, in some cases, Ni, Pd, or Pt may be needed as diffusion barriers for preventing the formation of IMCs. Furthermore, Kirkendall voids may also form after the reaction between the liquefied solder and metallization surface, which would reduce the effective bonding area at the interface [22].

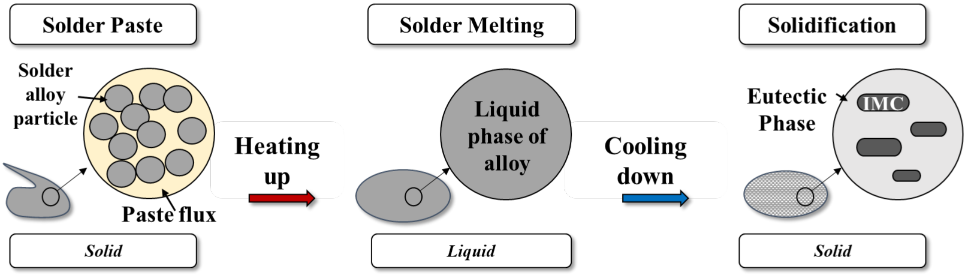
Solder Paste
Solder Melting
Solidification
Solder alloy particle
Paste flux
Heating up
Liquid phase of alloy
Cooling down
Eutectic Phase
IMC
Solid
Liquid
Solid

Figure 1.4: The schematic illustration of the reflow soldering process in a microscopic view.

1.2.2. TRANSIENT LIQUID PHASE METHOD

When traditional solder alloys cannot meet the high-temperature reliability requirements for the WBG semiconductors, transient liquid phase bonding (TLPB) has been developed because of its "low processing temperature and high operating temperature" performance. The terms “transient liquid phase sintering” (TLPS), “liquid phase diffusion bonding” (LPDB), and “solid-liquid interdiffusion” (SLID) are also being applied to describe this method [23]. In this method, a low-melting temperature phase (LTP), such as Sn, and high-melting temperature phases (HTP) such as Cu, are utilized to form the metallurgical bonding. At temperatures above the liquidus line of the LTP, the melted LTP will diffuse into the solid state HTP and wet the particle surface to be joined. Along with the isothermal solidification, some IMC is formed in the joint to provide robust connection [24].

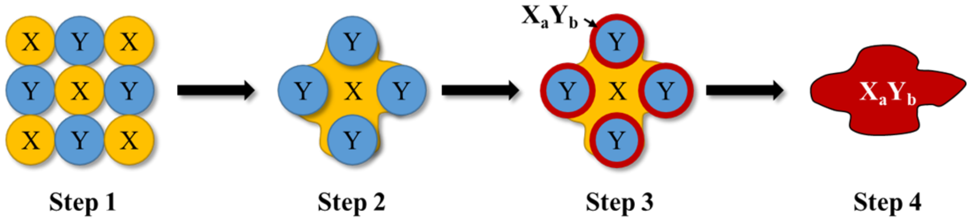
X
Y
X_aY_b
X_aY_b
Step 1
Step 2
Step 3
Step 4

Figure 1.5: The schematic diagram of TLPB process.

As shown in the Fig.1.5, the TLP method can be divided into four steps in general: heating, melting, interdiffusion and IMC formation [25]:

- In Step 1, the organics in the TLP paste are evaporated first. At the same time, the LTP (particles X) and HTP (particles Y) will approach each other with the temperature ramping up and solid-to-solid interdiffusion starts to occur.
- In Step 2, a liquid phase of X is formed when the temperature is above the melting temperature of X. The formation of the liquid phase is crucial at this point, as it will wet the surface of particle Y, accelerating mass transportation.
- Next in Step 3, the interdiffusion from the solid phase Y to the liquid phase X will occur. For better-joining performance, an auxiliary pressure and vacuum can be applied to guarantee the dense contact and promote interdiffusion of X and Y.
- Finally, at a certain point, when sufficient Y is diffused into X, IMC X_aY_b in the joint will form via an isothermal solidification process. The newly formed X_aY_b will provide robust bonding to the joint and contain a higher melting temperature than X.

As an example, the Cu-Sn binary system is a classical TLPB system. In this system, the LTP is Sn with a melting temperature of 232°C. After TLPB process, the remelting temperature of as-formed IMC Cu_6Sn_5 is increased up to 415°C[26]. However, the TLPB technique suffers from various non-negligible problems that limit its wide range of applications [27]. The as-formed IMC Cu_6Sn_5 is a brittle phase which will deteriorate the mechanical strength and reliability of the joint. Second, since TLPB is a reaction-based process, it is necessary to maintain accurate stoichiometry as well as long-lasting reaction times. This will increase the control difficulty of the process. In addition, pore formation and incomplete wetting of the LTP also occur from time to time, which may decrease the electrical and thermal conductivity.

1.2.3. SINGLE-METAL SINTERING

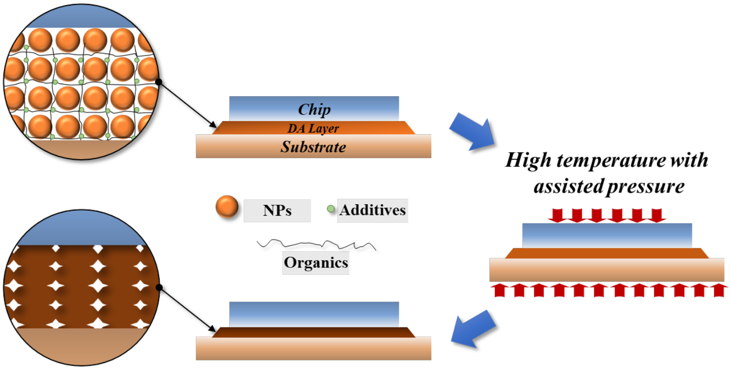

Figure 1.6: A schematic diagram of single metal sintering process.

As introduced in the previous section, WBG semiconductor devices have been extensively developed over the past decades and are gradually replacing Si-based devices in most high switching frequency, high power density and high temperature applications. However, the use of conventional lead-free solutions such as reflow soldering and

TLPB for WBG die attachment is limited due to their low melting point, low creep resistance, low thermal and electrical conductivity, and IMC precipitate problems [28]. To overcome these issues, low-temperature sintering techniques have been proposed and developed over the past two decades [29]–[33]. Here is a schematic diagram of the pressure-assisted sintering technique as shown in Fig.1.6.

Generally speaking, sintering is the process of compacting and forming a powdery material into a solid bulk material by heat and pressure at temperatures well below the point of liquefaction [34]. After the formation and densification of the sintered body, it will obtain the excellent physical properties (melting temperature, thermal conductivity, mechanical strength) that is close to its corresponding bulk material. Therefore, sintering is also a technology with "low processing temperature and high operating temperature" advantage. The driving force for sintering is the reduction of the surface area and decreasing of the surface free energy during the densification process. On a microscopic scale, such process occurs through atomic transportation (mass transportation) at the contact area of particles [35], such as surface, grain boundary, and lattice diffusion. A schematic diagram of the material transport during the sintering process is illustrated in Fig.1.7.

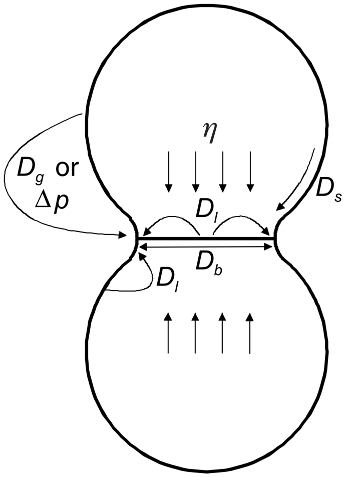

Figure 1.7: A schematic diagram of the material transport during the sintering process.[35]

Silver and copper have excellent electrical and thermal conductivity and high melting points (960°C and 1083°C, respectively) and are very suitable materials for sintering technology in power semiconductor packaging [36], [37]. Nano-silver sintering has emerged as a promising technique to form the die-attach joint for power devices. However, there are two significant limitations of sintered Ag joint, namely high material costs [38] and electrochemical migration [39]. Recently, nano copper sintering is receiving great attentions because of its much lower material cost (about 1~10% of the Ag price), lower ion migration tendency, as well as sufficiently high thermal conductivity (398 W/mK for bulk material) [40]–[44]. The material properties can be easily found from the Table1.1 below.

Table 1.1: Material properties of different die-attach techniques.

	SAC	$Au_{80}Sn_{20}$	TLP Cu-Sn	Ag Sintering	Cu Sintering
$T_{process}$(°C)	217–221	308 (278+30)	280, 30 min	250	250
$T_{melting}$(°C)	217	278	415	960	1084
CTE ($10^{-6}K^{-1}$)	20	16	/	18–23	16-21
σ * (MPa)	~45	65~130	20~40	20~80	20~80
λ ** (W/(mK))	60	57	34~70	>100	>100
Cost	Lowest	Highest	Midium	High	Low
Ref.	[18], [19]	[20], [45], [46]	[23], [47], [48]	[29]–[33]	[40]–[44]

*: shear strength
**: thermal conductivity

1.3. COPPER SINTERING TECHNIQUE

IN this section, a comprehensive review of related studies on Cu sintering techniques is given. Firstly, the state-of-art Cu particles pretreatment methods are reviewed. Then typical sintering paste formulations and the important studies of Cu sintering process and sintering mechanisms are summarized. Finally, a brief review for MD simulation of the Cu NPs coalescence is given. For each topic, questions and challenges are summarized as well.

1.3.1. MATERIAL TREATMENT

DIFFERENT synthesis methods of Cu particles were proposed to obtain small-size NPs with low-temperature sintering ability. Most of them were based on the modified polyol method applying different precursor and reducing agent. However, the biggest challenges that nano copper material encountered for the industrial application are the high oxidation risk, strong agglomeration tendency, and complex sintering process[49], [50]. Different approaches have been attempted to address these issues. First of all, the most effective way to avoid copper oxidation and to guarantee the good bonding performance was by injecting reducing atmosphere with specific concentration during sintering [51], [52]. The similar scheme also included by setting an intentional oxidation-reduction process of copper NPs during the sintering process [49], [53]–[55]. However, from an industrial/practical application point of view, the reduction gas and oxidation-reduction reactions may increase the cost as well as the complexity of the process.

For this reason, a protective treatment for Cu nano particles (NPs) in advance combined with applying of inert atmosphere during sintering can be a better way [56]. First of all, some groups have attempted to incorporate an in-situ coating process in addition to the copper particles producing process. These synthesis methods were also based on the modified polyol method with specific reducing agent, such as hydrazine [57], [58], citric acid[57], PVP[59], [60], L-ascorbic acid[61], [62], formic acid[63].

Other groups preferred to develop the post-treatment process after the production of copper particles, in order to reduce the difficulties on the precise control of both the NPs preparation and the coating treatment at the same time. Gao et al.[64] used ascorbic acid to treat the as-produced NPs. After the treatment, the NPs obtained the self-reductive ability. Then by sintering at 250°C for 30 min with 0.4 MPa the joint showed over 15 MPa bonding strength. Zhao et al.[65] synthesized 30 nm mono-dispersed copper NPs and then did treatment process on the particles. The joint could have 17 MPa shear strength after sintering at 240°C. Mou et al.[56] reported that they used carboxylic acid (formic acid and oxalic acid) to modify the surface of Cu NPs(150~200 nm) and obtained over 20 MPa bonding performance by sintering at 250°C for 60 min in Ar-H_2 (5%H_2) with 10 MPa assisted pressure.

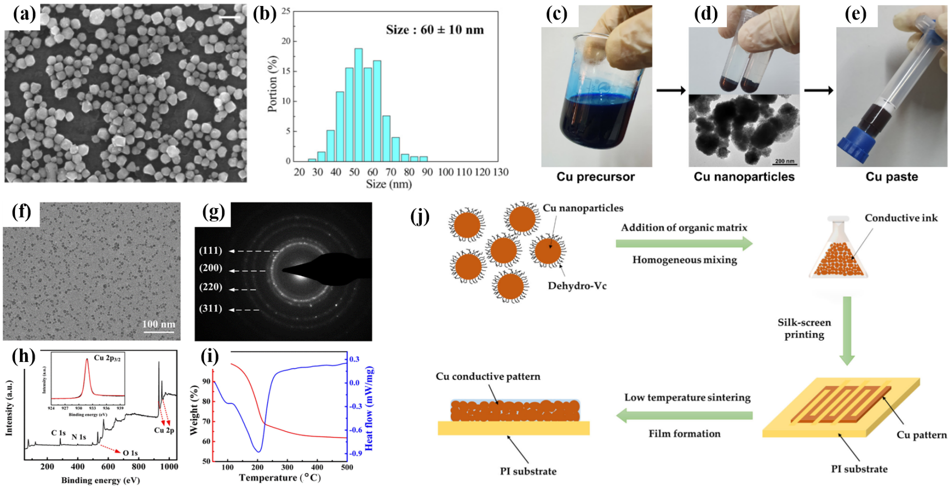
(a)
(b)
Size : 60 ± 10 nm
Portion (%)
25
20
15
10
5
0
20 30 40 50 60 70 80 90 100 110 120 130
Size (nm)
(c)
(d)
(e)
Cu precursor
Cu nanoparticles
Cu paste
200 nm
(f)
100 nm
(g)
(111)
(200)
(220)
(311)
(h)
Cu 2p3/2
Intensity (a.u.)
924 927 930 933 936 939
Binding energy (eV)
C 1s
N 1s
O 1s
Cu 2p
200 400 600 800 1000
Binding energy (eV)
(i)
Weight (%)
90
80
70
60
50
Heat flow (mW/mg)
0.3
0.0
-0.3
-0.6
-0.9
100 200 300 400 500
Temperature (°C)
(j)
Cu nanoparticles
Dehydro-Vc
Addition of organic matrix
Homogeneous mixing
Conductive ink
Silk-screen printing
Cu pattern
PI substrate
Low temperature sintering
Film formation
Cu conductive pattern
PI substrate

Figure 1.8: (a) The SEM photo and (b) the size distribution plot of the synthesized Cu NPs by using the modified polyol method in[66]. (c) to (e) The preparation process from Cu precursor to Cu NPs then to Cu paste[67]. (f) to (i) The SEM photo, TEM diffraction photo, XPS and DSC/TG results of the Cu NPs[68]. (j) The Cu NPs treatment and the corresponding sintering preocess[69].

It has also been found that the reduction of Ag and Cu particle size could effectively lower the sintering temperature to obtain the desired sintered joint[65], [70], [71]. However, smaller particle size can also increase the risk of particle spontaneous oxidation and agglomeration [72]. In our previous research[73], [74], it was found that, via proper particle treatment and sintering process, the particle with around 100 nm of size could already be sintered well. Therefore, applying Cu quasi-nanoparticles (QNPs, average diameter is between 100 nm and 200 nm) could be another option[56], [75], [76]. From the above discussion, the specific particle size, material treatment methods, and sintering conditions need to be comprehensively designed based on the sintering performance requirements.

1.3.2. PASTE FORMULATION AND SINTERING PROCESS

After the preparation of metallic particles, the organic components will be added and blended to form a viscous slurry that has specific viscosity, workability and preservation properties. The selection and the amount of organic components are crucial to modulate the performance of the paste. Normally, very small amounts of different functional additives can be added into the organic solvents to form the so-called vehicle, as shown in Fig.1.8j and Fig.1.9a. A common vehicle contains resins, solvents, thickeners and acid reductants. The resin mainly controls the rheology of the paste and greatly affects the printing performance. The solvent controls the evaporation of the vehicle and facilitates interparticle contact during printing and sintering. The thickener improves the rheological properties of the paste; and the acid reductant promotes sintering by reducing the oxides during the heating process. In the recent study[77], more than 50 different formulations were optimized: fluxes containing methyl ethyl ketone, isopropyl alcohol, methyl pyrrolidone, butyl fibrinolyte, pine alcohol, Tektros D85, Troy rheology additive, and malonic acid performed best. The prepared nanoparticles are then added to the as-prepared vehicle by stirring, three-roll milling and ultrasonic oscillation to formulate a homogeneous mixed copper paste.

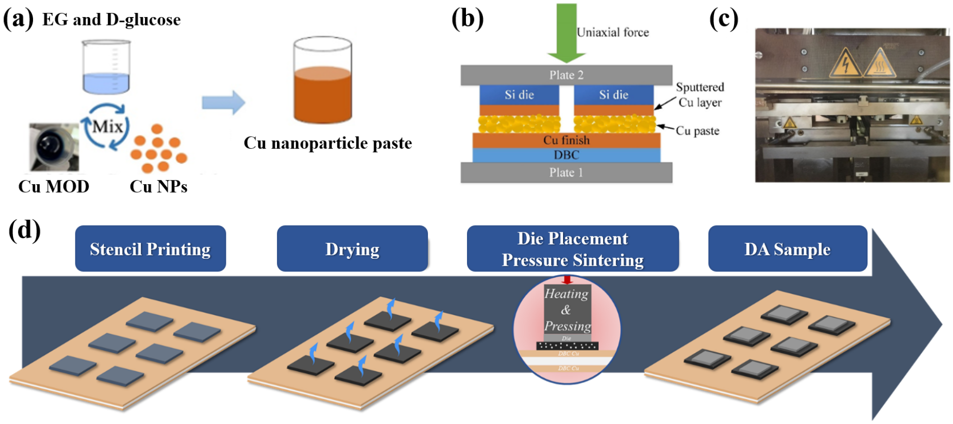

Figure 1.9: (a) The pringting, drying and die-attach process flow[78]. (b) A schematic diagram and (c) a real sintering tool of the pressure-assisted sintering process[79]. (d) Schematic illustration of typical pressure-assisted sintering process.

Normally, the stencil printing process will be used to apply the paste. The substrate is loaded under the stencil, and a squeegee is used to move the paste on the stencil surface. Then the paste will be deposited through the stencil mask to form the designed pattern on the substrate. The paste volume is a function of the stencil, the printing process and equipment, paste properties. Next, the as-printed substrate needs to be delivered to a vacuum oven for a drying process, in which the organic solvent will be evaporated, as shown in Fig.1.9d. Then, the chip will be accurately placed on the as-dried pattern pad by the so-called pick & place process. Finally, the sample is sent into a nitrogen oven or a heat press sintering oven to conduct sintering process. To improve the performance and reliability of sintered joints, the pressure-assisted sintering method is developed in the industry [80], [81]. By applying moderate external pressure to the die-attached samples, not only the metallic particles will be pushed together for better atomic diffusion, but also the porosity of the die-attach layer is reduced. Moreover, thanks to the development of advanced pressure-assisted sintering machine (or so-called sintering press) in the past few years, it is possible to provide precise pressure control to multiple samples simultaneously, as shown in Fig.1.9b and c. Therefore, fast sintering process (less than 5 min per batch) is achieved in the industry. As a result, copper materials will not be exposed to oxygen for too long, which considerably reduces the risk of oxidation during sintering[70], [82].

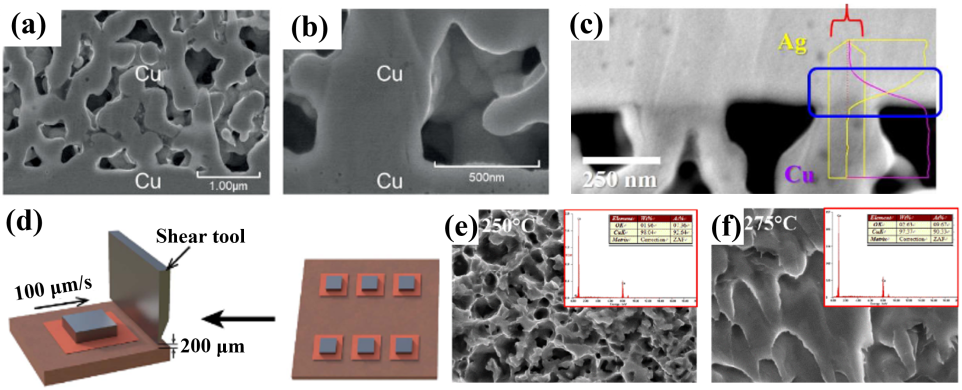

Figure 1.10: (a) and (b) Typical SEM images of the cross-section view of the die-attach region[83]. (c) The EDX analysis on the die-attach interface between the dice and the sintering layer[84]. (d) A schematic of die shear test[67]. (e) and (f) Typical SEM images of the sheared-off fracture surface of the die-attach sample[85].

For the evaluation of material properties, sintered joint performance and packaging device reliability, different methodologies have been applied from macroscopic to nanoscale. First, for material properties characterization, scanning electron microscope (SEM), transmission electron microscope (TEM), X-ray diffraction (XRD), Optical Microscope (OM), X-ray photoelectron spectroscopy (XPS) and Fourier transformed infrared (FTIR) spectroscopy are applied. OM, SEM and TEM are mostly used for observing the microstructural morphology of the NPs at different magnification levels, as shown in Fig.1.10a and b. Besides, energy disperse spectroscopy (EDS) can be further applied to analyze the elemental content at specific positions, as displayed in Fig.1.10c. XRD and XPS are used for checking oxidation condition at different thicknesses of the material. FTIR is used for investigation of the functional groups of organics present in a material system. Moreover, thermogravimetric analysis (TGA) and differential scanning calorimetry (DSC). can be used to study the phase transformation behavior of materials at different temperatures.

Then for sintered joints, the most important evaluation objects include: mechanical strength, failure modes, functional properties and reliability performance. The shear test is the most popular test applied both in the industry and academia for testing bonding strength, see Fig.1.10d. Then the SEM can be applied to observe the fracture surface as well as cross-section of the sintered joint, as displayed in . For functional material properties, four-point probe tester and laser-flash tester are always used for testing electrical resistivity and thermal conductivity of sintered bulk. Next, in order to test the reliability of the die-attached sample, there are hot temperature storage (HTS) test, thermal cycling test (TCT), thermal shock (TS) test and power cycling (PC) test. Normally the shear strength and thermal resistance are evaluated at the point before and after the reliability test to reveal the material properties degradation and failure modes.

When experimental method is difficult to conduct, the simulation method is also utilized for the fundamental investigation of the NPs coalescence mechanism at atomic-scale. One of the most applied simulation methods is Molecular Dynamics (MD), which can help to analyze the atomic movement and interaction of the material. By numerically solving Newton's equations of motion for the particles system, it allows us to obtain the microstructural evolution, dislocation behavior and diffusion process during the sintering[86]–[90]. Additionally, it can also help to analyze sintering mechanisms at various temperatures, including grain boundary diffusion, matrix diffusion, surface diffusion, plastic deformation mechanism [91]–[93].

1.4. CHALLENGES AND RESEARCH OBJECTIVES

THE previous introduction demonstrated that copper sintering technique has many potential advantages over silver sintering, TLPB technique, and reflow soldering regarding the performance, reliability, and cost for SiC power electronics packaging. However, a review of literature reveals that the research on copper sintering is still in its preliminary stages. Few studies and reports did comprehensive research on the raw materials, processes, microstructure evolution, sintering performance, reliability, and application validation. Therefore, it is important to study the copper sintering technique starting from a material point of view, in combination with the sintering process, microstructural mechanisms and packaging applications:

1.4.1. FOR ATOMIC-SCALE SINTERING MECHANISM

WHEN considering the sintering behavior of the nano-sized materials, it is a challenge to use experimental methods to study the nano-scale sintering mechanisms. In this context, MD simulation is often used to fundamentally investigate the NPs coalescence mechanism during the sintering process. However, most of the current MD research is based on two-particle or multi-particle models, which focus on neck formation and crystal rearrangement of the free-standing particles. In fact, in a practical semiconductor packaging scenario, nanoparticles need to be sintered between a backside metallization layer of the chip and a metallic surface of the substrate. Thus, the interaction between the NPs and the components around may not be negligible, which may significantly affect processes such as contact of particles, formation of the necks, distribution of stress, and generation of the pores. It was found that the interactions between different components at each sintering stage and the corresponding coalescence kinetics have not been discussed yet. Therefore, more simulation studies including these factors should be conducted in the future.

1.4.2. FOR CU PARTICLES TREATMENT METHOD AND SINTERING PROCESS EFFECT

THE in-situ treatment methods for Cu particles mentioned in the previous sections rely on the precise control of the additives amount in order to control the particle diameter and to prevent particle from aggregating in organic solvents simultaneously. Therefore, for industrial-scale applications such in-situ treatment method during the Cu NPs generation process is problematic. Correspondingly, creating protective capping after the synthesis of copper nanoparticle can be a more feasible solution. The effect of the post-treatment method on the oxidation removal and sintering performance enhancement need to be proved. Moreover, sintering temperature, pressure, and time are the three dominant factors that determine the sintering properties. In order to guarantee the performance of the sintering at short times, it is first necessary to investigate the effect of the process parameters on the microstructural evolution and bonding mechanism. In the field of Ag sintering, there has been a great deal of research on the effect of the parameters of the sintering process. However, few researchers have reported on the effect of sintering parameters while incorporating microstructural analysis for Cu sintering techniques.

1.4.3. FOR MECHANICAL, THERMAL AND ELECTRICAL PROPERTIES EVALUATION

MECHANICAL strength, thermal conductivity and electrical resistivity are the three most important functional properties of the Cu-sintered joint, which can reflect the ability of DA layer on device bonding, heat dissipation and electrical signal transmission. In material science, hardness is the resistance to locally plastic deformation, and elastic modulus is the resistance to the elastic deformation. Both of them are important mechanical parameters to evaluate the mechanical properties of DA joints. However, up to now, the mechanical reliability of Cu-sintered DA material at various temperatures has yet to be thoroughly studied in the academy and industry. Apart from that, due to the porous microstructure, the resistivity of the sintered joints is several times higher than that of the corresponding metallic bulk material. Optimizing the sintering parameters to obtain lower resistivity is a viable way to improve the applicability of Cu sintering techniques. However, few researchers have reported on the effect of sintering parameters on these properties while incorporating microstructural analysis. Therefore, a comprehensive study of the mechanical strength, resistivity, and thermal conductivity of the microstructure of sintered samples with different process parameters is significantly necessary.

1.4.4. FOR DIE-ATTACHMENT APPLICATION OF SIC DEVICES

NANO-silver sintering technology is relatively mature and has been applied to large-scale products. Considering the importance of efficiency-performance balance in industrial production, the use of inert-atmospheric conditions and pressure-assisted sintering can be a reasonable solution. In contrast, copper sintering technology research is still in the laboratory stage and there are very few demonstrations of nano Cu-sintering technology in functional packaging modules. In practical applications, in addition to the performance of the die-attachment material itself, it is also necessary to consider the adaptability of the packaging material to the packaging process, the switching performance, the thermal performance and the reliability of the power module after the packaging process. Therefore, a systematic study of Cu-sintering techniques in combination with materials, process, simulation, and testing is of great importance to boost the application of such techniques to industrial applications.

1.5. THESIS OUTLINE

This dissertation is divided into six chapters, as shown in Fig.1.11. In Chapter 2, a MD simulation was carried out to study the coalescence kinetics and microstructure evolution of Cu nanoparticles sintering at various temperatures. A sandwich structure model with two substrates and multiple particles in between was constructed to simulate the practical die-attach structure. The size effect of nanoparticles and pressure effect of the substrate at 500K low-temperature sintering process of this structure was thoroughly studied. Furthermore, the microstructure change, crystalline evolution, the dislocation generation and annihilation were monitored by carrying out Common Neighbor Analysis (CNA), and Dislocation Extraction Algorithm (DXA) analysis. Then the atomic diffusion activities were studied by analyzing the corresponding atomic Mean-Squared Displacement (MSD) diagrams. In addition, particle rotation phenomena and pore evolution during sintering have been extensively studied. Based on the studies in this chapter, the positive and negative effect of the substrate on the evolution of the nanoparticles sintering mechanism and the generation of the microscopic pores were deeply discussed.

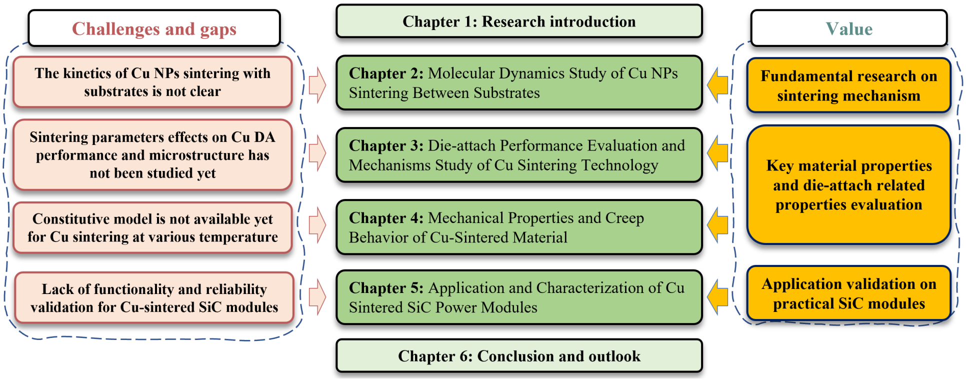
Challenges and gaps
The kinetics of Cu NPs sintering with substrates is not clear
Sintering parameters effects on Cu DA performance and microstructure has not been studied yet
Constitutive model is not available yet for Cu sintering at various temperature
Lack of functionality and reliability validation for Cu-sintered SiC modules
Chapter 1: Research introduction
Chapter 2: Molecular Dynamics Study of Cu NPs Sintering Between Substrates
Chapter 3: Die-attach Performance Evaluation and Mechanisms Study of Cu Sintering Technology
Chapter 4: Mechanical Properties and Creep Behavior of Cu-Sintered Material
Chapter 5: Application and Characterization of Cu Sintered SiC Power Modules
Chapter 6: Conclusion and outlook
Value
Fundamental research on sintering mechanism
Key material properties and die-attach related properties evaluation
Application validation on practical SiC modules

Figure 1.11: The outline of the thesis.

In Chapter 3, a self-developed Cu paste was fabricated with the predefined printing, drying and sintering workability. A reductive pretreatment was conducted in advance to the raw Cu particles to remove the original oxidation. Laser flash measurements, four-probe methods, and die shear tests were performed to obtain the thermal, electrical, and bonding properties of Cu-sintered die attachment techniques. The effects of temperature, pressure, and time on the integrated properties and the microstructural evolution of the sinter joints are then investigated in depth. The neck formation, pore development, and fracture surface of the associated sintering joints were investigated. The sintering mechanism is obtained together with the optimized sintering process parameters, which can be used in practical applications.

In Chapter 4, the key material mechanical properties such as indentation hardness, elastic modulus and creep effect of Cu sintered sample were evaluated by nanoindentation test respectively, to verify the long-term application feasibility of this technique. The tested displacement-load curves were used to analyze the elastic-plastic behavior and to calculate the key mechanical parameters. At the beginning, a series of indentation tests were performed with various peak loads and loading rates to remove the effect of indentation depth on the measured values of hardness and elastic modulus. Then the constitutive models (yield stress, strain hardening exponent factors) for samples sintered via different applied pressure were obtained, which can be employed to describe the room-temperature mechanical properties of the Cu-sintered joint. The effects of temperature ranging from 150°C to 240°C on these values were investigated. The high-temperature creep behavior was studied and compared for samples sintered with different applied pressures. The results obtained in this chapter can be applied in evaluating the feasibility of the application of the Cu sintering technique at various temperatures in the semiconductor packaging industry.

Finally, in Chapter 5, the optimized pressure-assisted Cu sintering die-attachment process was adopted to fabricate several SiC power modules. The same sintering process (250°C/3 min/20 MPa) as in previous chapters was used here and the rest of packaging process was conducted on an industrial standard packaging production line. The reliability of shear strength, on-resistance (R_{DSon}) and thermal resistance ($R_{th(jc)}$) was investigated through 150°C / 1000 hours high temperature storage test and -40°C to 150°C / 1000 cycles thermal cycling test. Then, the static and dynamic tests of Cu-sintered SOT227 and 62mm SiC module were conducted. As a benchmark, a commercial silver-sintered SiC module was set in parallel. The experimental results indicated that both the output characteristics and switching performance of Cu-sintered SiC module were at the same level as that of Ag-sintered module. Considering the comprehensive cost-performance balance, the presented Cu sintering technology is quite promising for WBG power electronics packaging application in the coming future.

REFERENCES

[1] R. Pachauri and L. Meyer, “Climate change 2014: Synthesis report. contribution of working groups i, ii and iii to the fifth assessment report of the intergovernmental panel on climate change”, 2014.

[2] M. Koh *et al.*, *Green infrastructure financing*. Springer, 2018.

[3] M. A. Destek and A. Sinha, “Renewable, non-renewable energy consumption, economic growth, trade openness and ecological footprint: Evidence from organisation for economic co-operation and development countries”, *Journal of Cleaner Production*, vol. 242, p. 118 537, 2020.

[4] M. Rashid, *Power electronics handbook: devices, circuits, and applications, ed.* Academic Press. Elsevier, 2010.

[5] J. Millan, P. Godignon, X. Perpiñà, A. Pérez-Tomás, and J. Rebollo, “A survey of wide bandgap power semiconductor devices”, *IEEE transactions on Power Electronics*, vol. 29, no. 5, pp. 2155–2163, 2013.

[6] M. Bhatnagar and B. J. Baliga, “Comparison of 6h-sic, 3c-sic, and si for power devices”, *IEEE Transactions on electron devices*, vol. 40, no. 3, pp. 645–655, 1993.

[7] A. Ibrahim, J.-P. Ousten, R. Lallemand, and Z. Khatir, “Power cycling issues and challenges of sic-mosfet power modules in high temperature conditions”, *Microelectronics Reliability*, vol. 58, pp. 204–210, 2016.

[8] L. Zhang, X. Yuan, X. Wu, C. Shi, J. Zhang, and Y. Zhang, “Performance evaluation of high-power sic mosfet modules in comparison to si igbt modules”, *IEEE Transactions on Power Electronics*, vol. 34, no. 2, pp. 1181–1196, 2018.

[9] Y. Développement, *Power module packaging: Ev/hev changes the rules of game*. `https://www.yolegroup.com/iso_upload/News/2020/PR_POWER_`, accessed on 2020-07-27, 2020.

[10] B. J. Baliga, *The IGBT device: physics, design and applications of the insulated gate bipolar transistor*. William Andrew, 2015.

[11] C. D. Fuentes, S. Kouro, and S. Bernet, “Comparison of 1700-v sic-mosfet and si-igbt modules under identical test setup conditions”, *IEEE Transactions on Industry Applications*, vol. 55, no. 6, pp. 7765–7775, 2019.

[12] G. Wang, F. Wang, G. Magai, Y. Lei, A. Huang, and M. Das, “Performance comparison of 1200v 100a sic mosfet and 1200v 100a silicon igbt”, in *2013 IEEE Energy Conversion Congress and Exposition*, IEEE, 2013, pp. 3230–3234.

[13] L. D. Stevanovic, K. S. Matocha, P. A. Losee, J. S. Glaser, J. J. Nasadoski, and S. D. Arthur, “Recent advances in silicon carbide mosfet power devices”, in *2010 Twenty-Fifth Annual IEEE Applied Power Electronics Conference and Exposition (APEC)*, IEEE, 2010, pp. 401–407.

[14] S. Hazra, S. Madhusoodhanan, G. K. Moghaddam, K. Hatua, and S. Bhattacharya, “Design considerations and performance evaluation of 1200-v 100-a sic mosfet-based two-level voltage source converter”, *IEEE Transactions on Industry Applications*, vol. 52, no. 5, pp. 4257–4268, 2016.

[15] C. Chen, F. Luo, and Y. Kang, “A review of sic power module packaging: Layout, material system and integration”, *CPSS Transactions on Power Electronics and Applications*, vol. 2, no. 3, pp. 170–186, 2017.

[16] C. Qian, A. M. Gheitaghy, J. Fan, *et al.*, “Thermal management on igbt power electronic devices and modules”, *IEEE Access*, vol. 6, pp. 12 868–12 884, 2018.

[17] J. O. Gonzalez, R. Wu, S. Jahdi, and O. Alatise, “Performance and reliability review of 650 v and 900 v silicon and sic devices: Mosfets, cascode jfets and igbts”, *IEEE Transactions on Industrial Electronics*, vol. 67, no. 9, pp. 7375–7385, 2019.

[18] C.-J. Chen, C.-M. Chen, R.-H. Horng, D.-S. Wuu, and J.-S. Hong, “Thermal management and interfacial properties in high-power gan-based light-emitting diodes employing diamond-added sn-3 wt.% ag-0.5 wt.% cu solder as a die-attach material”, *Journal of electronic materials*, vol. 39, no. 12, pp. 2618–2626, 2010.

[19] K. S. Siow, "Die-attach materials for high temperature applications in microelectronics packaging", *Materials, Process, Equipment, and Reliability, Springer International Publishing*, pp. 181–196, 2019.

[20] J. Doesburg and D. Ivey, "Microstructure and preferred orientation of au–sn alloy plated deposits", *Materials Science and Engineering: B*, vol. 78, no. 1, pp. 44–52, 2000.

[21] J. Chen, Y. Yin, J. Ye, and Y. Wu, "Investigation on fatigue behavior of single snagcu/snpb solder joint by rapid thermal cycling", *Soldering & Surface Mount Technology*, 2015.

[22] A. Paul, A. A. Kodentsov, and F. J. van Loo, "Intermetallic growth and kirkendall effect manifestations in cu/sn and au/sn diffusion couples", *International Journal of Materials Research*, vol. 95, no. 10, pp. 913–920, 2004.

[23] S. M. Choquette and I. E. Anderson, "Liquid-phase diffusion bonding: Temperature effects and solute redistribution in high-temperature lead-free composite solders.", *International Journal of Powder Metallurgy*, vol. 51, no. 4, 2015.

[24] V. Vuorinen, A. Rautiainen, and M. Paulasto-Kröckel, "Design for reliability of au-sn and cu-sn based slid bonds", in *2015 European Microelectronics Packaging Conference (EMPC)*, IEEE, 2015, pp. 1–6.

[25] X. Qiao and S. Corbin, "Development of transient liquid phase sintered (tlps) sn–bi solider pastes", *Materials Science and Engineering: A*, vol. 283, no. 1-2, pp. 38–45, 2000.

[26] J. Li, P. Agyakwa, and C. Johnson, "Interfacial reaction in cu/sn/cu system during the transient liquid phase soldering process", *Acta materialia*, vol. 59, no. 3, pp. 1198–1211, 2011.

[27] G. O. Cook and C. D. Sorensen, "Overview of transient liquid phase and partial transient liquid phase bonding", *Journal of materials science*, vol. 46, no. 16, pp. 5305–5323, 2011.

[28] B.-S. Lee, Y.-H. Ko, J.-H. Bang, *et al.*, "Interfacial reactions and mechanical strength of sn-3.0 ag-0.5 cu/ni/cu and au-20sn/ni/cu solder joints for power electronics applications", *Microelectronics Reliability*, vol. 71, pp. 119–125, 2017.

[29] C. Chen, Z. Zhang, Q. Wang, *et al.*, "Robust bonding and thermal-stable ag–au joint on enepig substrate by micron-scale sinter ag joining in low temperature pressureless", *Journal of Alloys and Compounds*, vol. 828, p. 154 397, 2020.

[30] J. Li, X. Li, L. Wang, Y.-H. Mei, and G.-Q. Lu, "A novel multiscale silver paste for die bonding on bare copper by low-temperature pressure-free sintering in air", *Materials & Design*, vol. 140, pp. 64–72, 2018.

[31] M. Wang, Y. Mei, W. Hu, X. Li, and G.-Q. Lu, "Pressureless sintered-silver as die attachment for bonding si and sic chips on silver, gold, copper, and nickel metallization for power electronics packaging: The practice and science", *IEEE Journal of Emerging and Selected Topics in Power Electronics*, vol. 10, no. 2, pp. 2645–2655, 2022.

[32] Z. Zhang and G.-Q. Lu, “Pressure-assisted low-temperature sintering of silver paste as an alternative die-attach solution to solder reflow”, *IEEE Transactions on electronics packaging manufacturing*, vol. 25, no. 4, pp. 279–283, 2002.

[33] Z. Zhang, C. Chen, A. Suetake, M.-C. Hsieh, A. Iwaki, and K. Suganuma, “Pressureless and low-temperature sinter-joining on bare si, sic and gan by a ag flake paste”, *Scripta Materialia*, vol. 198, p. 113 833, 2021.

[34] W. D. Kingery, H. K. Bowen, and D. R. Uhlmann, *Introduction to ceramics*. John wiley & sons, 1976, vol. 17.

[35] S.-J. L. Kang, *Sintering: densification, grain growth and microstructure*. Elsevier, 2004.

[36] T. Furukawa, M. Shiraishi, Y. Yasuda, *et al.*, “High power density side-gate higt modules with sintered cu having superior high-temperature reliability to sintered ag”, in *2017 29th International Symposium on Power Semiconductor Devices and IC’s (ISPSD)*, IEEE, 2017, pp. 263–266.

[37] K. S. Siow, “Are sintered silver joints ready for use as interconnect material in microelectronic packaging?”, *Journal of electronic materials*, vol. 43, no. 4, pp. 947–961, 2014.

[38] J.-W. Yoon and J.-H. Back, “Effect of sintering conditions on the mechanical strength of cu-sintered joints for high-power applications”, *Materials*, vol. 11, no. 11, p. 2105, 2018.

[39] R. Riva, C. Buttay, B. Allard, and P. Bevilacqua, “Migration issues in sintered-silver die attaches operating at high temperature”, *Microelectronics Reliability*, vol. 53, no. 9-11, pp. 1592–1596, 2013.

[40] C. Chen, A. Iwaki, A. Suetake, K. Sugiura, K. Kanie, and K. Suganuma, “Low temperature cu sinter joining on different metallization substrates and its reliability evaluation with a high current density”, in *2021 33rd International Symposium on Power Semiconductor Devices and ICs (ISPSD)*, IEEE, 2021, pp. 387–390.

[41] H.-J. Huang, X. Wu, M.-B. Zhou, and X.-P. Zhang, “A highly reliable die bonding approach for high power devices by low temperature pressureless sintering using a novel cu nanoparticle paste”, in *2020 IEEE 70th Electronic Components and Technology Conference (ECTC)*, IEEE, 2020, pp. 1697–1702.

[42] Y. Kobayashi, Y. Yasuda, and T. Morita, “Recent advances in the synthesis of copper-based nanoparticles for metal–metal bonding processes”, *Journal of Science: Advanced Materials and Devices*, vol. 1, no. 4, pp. 413–430, 2016.

[43] Y. Mou, H. Cheng, Y. Peng, and M. Chen, “Fabrication of reliable cu-cu joints by low temperature bonding isopropanol stabilized cu nanoparticles in air”, *Materials Letters*, vol. 229, pp. 353–356, 2018.

[44] S. Takata, C. Chen, Y. Gao, and K. Suganuma, “Sintering cu paste on cu plates with different metallization”, in *PCIM Europe 2019; International Exhibition and Conference for Power Electronics, Intelligent Motion, Renewable Energy and Energy Management*, VDE, 2019, pp. 1–6.

[45] Y. Tian, W. Zhou, and P. Wu, “A density functional investigation of the structural, elastic and thermodynamic properties of the au–sn intermetallics”, *Journal of Electronic Materials*, vol. 45, no. 1, pp. 639–647, 2016.

[46] Y. Liu, J. Zhao, C. C.-A. Yuan, G. Q. Zhang, and F. Sun, “Chip-on-flexible packaging for high-power flip-chip light-emitting diode by ausn and sac soldering”, *IEEE Transactions on Components, Packaging and Manufacturing Technology*, vol. 4, no. 11, pp. 1754–1759, 2014.

[47] Y. Zhong, R. An, C. Wang, *et al.*, “Low temperature sintering cu6sn5 nanoparticles for superplastic and super-uniform high temperature circuit interconnections”, *Small*, vol. 11, no. 33, pp. 4097–4103, 2015.

[48] C. C. Lee, P. J. Wang, and J. S. Kim, “Are intermetallics in solder joints really brittle?”, in *2007 Proceedings 57th Electronic Components and Technology Conference*, IEEE, 2007, pp. 648–652.

[49] X. Liu and H. Nishikawa, “Improved joint strength with sintering bonding using microscale cu particles by an oxidation-reduction process”, in *2016 IEEE 66th Electronic Components and Technology Conference (ECTC)*, IEEE, 2016, pp. 455–460.

[50] T. F. Chen and K. S. Siow, “Comparing the mechanical and thermal-electrical properties of sintered copper (cu) and sintered silver (ag) joints”, *Journal of alloys and Compounds*, vol. 866, p. 158 783, 2021.

[51] S. K. Bhogaraju, O. Mokhtari, F. Conti, and G. Elger, “Die-attach bonding for high temperature applications using thermal decomposition of copper (ii) formate with polyethylene glycol”, *Scripta Materialia*, vol. 182, pp. 74–80, 2020.

[52] Y. Gao, H. Zhang, W. Li, *et al.*, “Die bonding performance using bimodal cu particle paste under different sintering atmospheres”, *Journal of Electronic Materials*, vol. 46, no. 7, pp. 4575–4581, 2017.

[53] Y. Kobayashi, Y. Abe, T. Maeda, Y. Yasuda, and T. Morita, “A metal–metal bonding process using metallic copper nanoparticles produced by reduction of copper oxide nanoparticles”, *Journal of Materials Research and Technology*, vol. 3, no. 2, pp. 114–121, 2014.

[54] T. Fujimoto, T. Ogura, T. Sano, M. Takahashi, and A. Hirose, “Joining of pure copper using cu nanoparticles derived from cuo paste”, *Materials Transactions*, p. MI201410, 2015.

[55] Y. Zuo, S. Carter-Searjeant, M. Green, L. Mills, and S. H. Mannan, “High bond strength cu joints fabricated by rapid and pressureless in situ reduction-sintering of cu nanoparticles”, *Materials Letters*, vol. 276, p. 128 260, 2020.

[56] Y. Mou, Y. Peng, Y. Zhang, H. Cheng, and M. Chen, “Cu-cu bonding enhancement at low temperature by using carboxylic acid surface-modified cu nanoparticles”, *Materials Letters*, vol. 227, pp. 179–183, 2018.

[57] Y. Kobayashi, T. Shirochi, Y. Yasuda, and T. Morita, “Preparation of metallic copper nanoparticles in aqueous solution and their bonding properties”, *Solid state sciences*, vol. 13, no. 3, pp. 553–558, 2011.

[58] Y. Kamikoriyama, H. Imamura, A. Muramatsu, and K. Kanie, “Ambient aqueous-phase synthesis of copper nanoparticles and nanopastes with low-temperature sintering and ultra-high bonding abilities”, *Scientific reports*, vol. 9, no. 1, pp. 1–10, 2019.

[59] Y. Jianfeng, Z. Guisheng, H. Anming, and Y. N. Zhou, “Preparation of pvp coated cu nps and the application for low-temperature bonding”, *Journal of Materials Chemistry*, vol. 21, no. 40, pp. 15 981–15 986, 2011.

[60] J. Yan, G. Zou, A. Wu, J. Ren, A. Hu, and Y. N. Zhou, “Polymer-protected cu-ag mixed nps for low-temperature bonding application”, *Journal of electronic materials*, vol. 41, no. 7, pp. 1886–1892, 2012.

[61] J. Xiong, Y. Wang, Q. Xue, and X. Wu, “Synthesis of highly stable dispersions of nanosized copper particles using l-ascorbic acid”, *Green Chemistry*, vol. 13, no. 4, pp. 900–904, 2011.

[62] Y. Zhang, C. Cui, B. Yang, *et al.*, “Size-controllable copper nanomaterials for flexible printed electronics”, *Journal of Materials Science*, vol. 53, no. 18, pp. 12 988–12 995, 2018.

[63] W. L. Choi, Y. S. Kim, K.-S. Lee, and J.-H. Lee, “Characterization of the die-attach process via low-temperature reduction of cu formate in air”, *Journal of Materials Science: Materials in Electronics*, vol. 30, no. 10, pp. 9806–9813, 2019.

[64] Y. Gao, W. Li, C. Chen, *et al.*, “Novel copper particle paste with self-reduction and self-protection characteristics for die attachment of power semiconductor under a nitrogen atmosphere”, *Materials & Design*, vol. 160, pp. 1265–1272, 2018.

[65] J. Zhao, M. Yao, and N.-C. Lee, “Nano-cu sintering paste for high power devices die attach applications”, in *2018 IEEE 68th Electronic Components and Technology Conference (ECTC)*, IEEE, 2018, pp. 557–563.

[66] B. K. Park, S. Jeong, D. Kim, J. Moon, S. Lim, and J. S. Kim, “Synthesis and size control of monodisperse copper nanoparticles by polyol method”, *Journal of colloid and interface science*, vol. 311, no. 2, pp. 417–424, 2007.

[67] H.-J. Huang, X. Wu, M.-B. Zhou, and X.-P. Zhang, “A highly reliable die bonding approach for high power devices by low temperature pressureless sintering using a novel cu nanoparticle paste”, in *2020 IEEE 70th Electronic Components and Technology Conference (ECTC)*, IEEE, 2020, pp. 1697–1702.

[68] Y. Mou, H. Cheng, Y. Peng, and M. Chen, “Fabrication of reliable cu-cu joints by low temperature bonding isopropanol stabilized cu nanoparticles in air”, *Materials Letters*, vol. 229, pp. 353–356, 2018.

[69] Y. Zhang, C. Cui, B. Yang, *et al.*, “Size-controllable copper nanomaterials for flexible printed electronics”, *Journal of Materials Science*, vol. 53, no. 18, pp. 12 988–12 995, 2018.

[70] J. Liu, H. Ji, S. Wang, and M. Li, “The low temperature exothermic sintering of formic acid treated cu nanoparticles for conductive ink”, *Journal of Materials Science: Materials in Electronics*, vol. 27, no. 12, pp. 13 280–13 287, 2016.

[71] K. Siow and Y. Lin, “Identifying the development state of sintered silver (ag) as a bonding material in the microelectronic packaging via a patent landscape study”, *Journal of Electronic Packaging*, vol. 138, no. 2, 2016.

[72] M. C. Crisan, M. Teodora, and M. Lucian, “Copper nanoparticles: Synthesis and characterization, physiology, toxicity and antimicrobial applications”, *Applied Sciences*, vol. 12, no. 1, p. 141, 2021.

[73] X. Liu, Q. Zhou, X. Zhao, S. W. Koh, H. Ye, and G. Zhang, “Study and application of nano copper sintering technology in power electronics packaging”, in *2021 IEEE 71st Electronic Components and Technology Conference (ECTC)*, IEEE, 2021, pp. 1928–1932.

[74] X. Liu, Q. Zhou, Q. Liu, *et al.*, “Study on the effect of mixing proportion of micro- and nano-copper particles on sintering properties”, in *2020 21st International Conference on Electronic Packaging Technology (ICEPT)*, IEEE, 2020, pp. 1–5.

[75] L. Del Carro, J. Zürcher, U. Drechsler, I. E. Clark, G. Ramos, and T. Brunschwiler, “Low-temperature dip-based all-copper interconnects formed by pressure-assisted sintering of copper nanoparticles”, *IEEE Transactions on Components, Packaging and Manufacturing Technology*, vol. 9, no. 8, pp. 1613–1622, 2019.

[76] J. Zürcher, L. Del Carro, G. Schlottig, *et al.*, “All-copper flip chip interconnects by pressureless and low temperature nanoparticle sintering”, in *2016 IEEE 66th Electronic Components and Technology Conference (ECTC)*, IEEE, 2016, pp. 343–349.

[77] M. J. Kammer, A. Muza, J. Snyder, A. Rae, S. J. Kim, and C. A. Handwerker, “Optimization of cu–ag core–shell solderless interconnect paste technology”, *IEEE Transactions on Components, Packaging and Manufacturing Technology*, vol. 5, no. 7, pp. 910–920, 2015.

[78] Y. Yuan, H. Wu, J. Li, P. Zhu, and R. Sun, “Cu-cu joint formation by low-temperature sintering of self-reducible cu nanoparticle paste under ambient condition”, *Applied Surface Science*, vol. 570, p. 151 220, 2021.

[79] B. Zhang, A. Damian, J. Zijl, *et al.*, “In-air sintering of copper nanoparticle paste with pressure-assistance for die attachment in high power electronics”, *Journal of Materials Science: Materials in Electronics*, vol. 32, no. 4, pp. 4544–4555, 2021.

[80] T. G. Lei, J. Calata, S. F. Luo, G. Q. Lu, and X. Chen, “Low-temperature sintering of nanoscale silver paste for large-area joints in power electronics modules”, in *Key Engineering Materials*, Trans Tech Publ, vol. 353, 2007, pp. 2948–2953.

[81] M. Knoerr and A. Schletz, “Power semiconductor joining through sintering of silver nanoparticles: Evaluation of influence of parameters time, temperature and pressure on density, strength and reliability”, in *2010 6th International Conference on Integrated Power Electronics Systems*, IEEE, 2010, pp. 1–6.

[82] J. Liu, H. Chen, H. Ji, and M. Li, “Highly conductive cu–cu joint formation by low-temperature sintering of formic acid-treated cu nanoparticles”, *ACS applied materials & interfaces*, vol. 8, no. 48, pp. 33 289–33 298, 2016.

[83] S. Takata, C. Chen, Y. Gao, and K. Suganuma, “Sintering cu paste on cu plates with different metallization”, in *PCIM Europe 2019; International Exhibition and Conference for Power Electronics, Intelligent Motion, Renewable Energy and Energy Management*, VDE, 2019, pp. 1–6.

[84] J.-L. Jo, K. Anai, S. Yamauchi, T. Hattori, and T. Sakaue, “The bonding properties of various surface finishes with cu paste for pressure sintering”, in *2020 IEEE 70th Electronic Components and Technology Conference (ECTC)*, IEEE, 2020, pp. 749–754.

[85] Y. Mou, H. Cheng, Y. Peng, and M. Chen, “Fabrication of reliable cu-cu joints by low temperature bonding isopropanol stabilized cu nanoparticles in air”, *Materials Letters*, vol. 229, pp. 353–356, 2018.

[86] S. Paul, S. Mitra, D. Roy, *et al.*, “Molecular dynamics simulation study of neck growth in micro-selective laser sintering of copper nanoparticles”, in *Simulations for Design and Manufacturing*, Springer, 2018, pp. 259–292.

[87] B. Cheng and A. H. Ngan, “The sintering and densification behaviour of many copper nanoparticles: A molecular dynamics study”, *Computational materials science*, vol. 74, pp. 1–11, 2013.

[88] J. Guo, C. Xu, A. Hu, *et al.*, “Sintering dynamics and thermal stability of novel configurations of ag clusters”, *Journal of Physics and Chemistry of Solids*, vol. 73, no. 11, pp. 1350–1357, 2012.

[89] D. Hu, Z. Cui, J. Fan, X. Fan, and G. Zhang, “Thermal kinetic and mechanical behaviors of pressure-assisted cu nanoparticles sintering: A molecular dynamics study”, *Results in Physics*, vol. 19, p. 103 486, 2020.

[90] L. Yang, Y. Gan, Y. Zhang, and J. Chen, “Molecular dynamics simulation of neck growth in laser sintering of different-sized gold nanoparticles under different heating rates”, *Applied Physics A*, vol. 106, no. 3, pp. 725–735, 2012.

[91] F. Wakai, O. Guillon, G. Okuma, and N. Nishiyama, “Sintering forces acting among particles during sintering by grain-boundary/surface diffusion”, *Journal of the American Ceramic Society*, vol. 102, no. 2, pp. 538–547, 2019.

[92] C. Li, D. Li, X. Tao, H. Chen, and Y. Ouyang, “Molecular dynamics simulation of diffusion bonding of al–cu interface”, *Modelling and Simulation in Materials Science and Engineering*, vol. 22, no. 6, p. 065 013, 2014.

[93] B. Cheng and A. H. Ngan, “Crystal plasticity of cu nanocrystals during collision”, *Materials Science and Engineering: A*, vol. 585, pp. 326–334, 2013.

2

MOLECULAR DYNAMICS STUDY OF CU NPS SINTERING BETWEEN SUBSTRATES

Nano-copper sintering has great potential for wide-bandgap semiconductor packaging applications. However, it is a challenge to use experimental methods to study the atomic-scale sintering mechanisms. In order to investigate the coalescence kinetics of copper NPs for die-attach application, a molecular dynamic (MD) simulation was carried out in this chapter. A special model containing two substrates and 3×3 particles in between was employed to study the interactions between the NPs and the substrate. The microstructure change, crystalline evolution, dislocation generation and annihilation were monitored by carrying out the Mean-Squared Displacement (MSD) comparison, Common Neighbor Analysis (CNA), Dislocation Extraction Algorithm (DXA) analysis. In addition, the particle rotation phenomena and the pore evolution during sintering have been extensively studied by using the atomic trajectory tracking method. Finally, the effect of particle size on the sintering kinetics was investigated by comparing the simulation results for the 3 nm, 4 nm and 5 nm models.

Parts of this chapter have been published in Journal of Materials Research and Technology **17**, 1132 (2022).

2.1. INTRODUCTION

IN general, sintering is a thermally activated process that enhances material strength via particle necking connection and the formation of microstructural networks. On a microscopic scale, such process occurs through atomic transportation (mass transportation) at the contact area of particles [1], [2]. According to the research on high-temperature sintering [1], the dominant mass transportation mechanisms include 1) evaporation and recondensation, 2) surface diffusion, 3) volume diffusion beneath the surface, 4) grain boundary diffusion, 5) volume diffusion. However, in the field of the low-temperature semiconductor packaging process, usually the devices can only withstand process temperatures below 300°C. As a result, most of the above-mentioned high-temperature mechanisms cannot be activated.

In order to deeply understand the coalescence mechanism of nanoparticles (NPs) at low temperatures, atomic-scale simulation methods such as Molecular Dynamics (MD) can be applied, which can help us to observe the microstructural evolution, dislocation behavior and diffusion process during the sintering [2]–[6]. It has been reported that dominant mechanisms at low temperatures included grain boundary diffusion, matrix diffusion, surface diffusion, plastic deformation mechanisms, etc.[7]–[9]. However, most of the current studies are based on two- or three-particle models, which focus on neck formation, and crystal rearrangement of the free-standing particles. In fact, in a real semiconductor packaging scenario, NPs need to be sintered between a backside metallization layer of the chip and a metallic surface of the substrate. Thus, interactions between the NPs and the components around them can be non-negligible, which may significantly affect processes such as contact of particles, formation of the necks, distribution of stress, and generation of the pores. The interactions between different components at each sintering stage and the corresponding coalescence kinetics have not been discussed yet.

However, the use of MD methods to study the Cu NPs sintering between the chip and the substrate is very challenging. Dong et al. [10] showed that metallic nanoparticles can be deposited on the substrate in 400 ps through necking formation. E. Elkoraychy [11] used a similar model to explore homogeneous sintering and heterogeneous sintering. It is found that the particles were twisted due to the constraints effect of the substrate, and grain boundaries were formed in between. In the meantime, the particles penetrated into the substrate. Lan et al.[12] set particles on different sites and on a substrate with different orientations for sintering, and they found that the grain boundaries formed by the substrate and the particles during sintering could promote the generation of dislocations. The particles would then rotate and move slightly to eliminate grain boundaries. Wang et al.[13] conducted a transient liquid phase sintering simulation of Ni nanoparticles on an alloy substrate and stated that Ni nanoparticles in the matrix had stronger diffusion properties. The all-above-mentioned studies are based on the double-particles model or single-particle-substrate model. The interactions between the different components at each stage and the corresponding coalescence dynamics have not been discussed yet. Dai Ishikawa et al. [14] used a model containing multi-particles with substrates for the first time, and they mainly explored the diffusion behavior between Cu nanoparticles and different metal finishes. Whereas, the sintering mechanism, and pore evolution of such model, have not been studied yet. Overall, there is still a lack of sintering theories of the Cu sintered die-attach model concerning the behavior of necking formation, atomic diffusion, and defects evolution.

In the present work, by using the MD simulation method, we set up a die-attach model system consisting of two substrates and nine 4nm Cu particles in between. The sintering process at 500K of this structure was deeply studied. The microstructure change, crystalline evolution, dislocation generation and annihilation were monitored by carrying out the Mean-Squared Displacement (MSD) comparison, Common Neighbor Analysis (CNA), Dislocation Extraction Algorithm (DXA) analysis. In addition, the particle rotation phenomena and the pore evolution during sintering have been extensively studied by using the atomic trajectory tracking method. Finally, the effect of particle size on the sintering kinetics was investigated by comparing the simulation results for the 3 nm, 4 nm and 5 nm models.

2.2. METHODS

2.2.1. SIMULATION MODEL

IN this study, all MD simulation works were conducted by using Large-scale Atomic / Molecular Massively Parallel Simulator (LAMMPS)[15]. The embedded atom method (EAM)[16] potential developed by Fischer[17] was used to describe the low-temperature atomic interactions among copper atoms in particles and substrates. In this study, a special sandwiched-like model containing two substrate and multiple particles in between was applied as shown in Fig.2.1 . Previous studies have dealt with typical models which applied different amounts of NPs and substrate as shown in Appendix A. It turns out that in order to study the interaction between substrates and NPs, the effect of particle size on sintering kinetics, microstructure and pores evolution during sintering, the model of double substrates with multiple NPs is a reasonable selection.

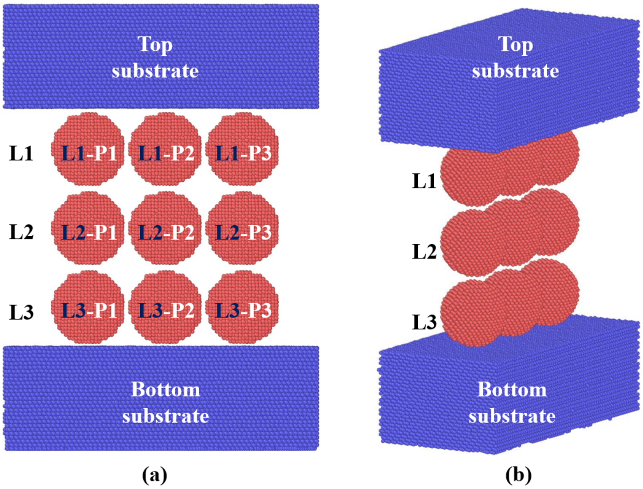

Figure 2.1: Initial configuration of the particle-substrate model for coalescence simulation. (a) Front view and (b) side view.

Previous studies also found that a diameter of NP within 2.8 nm to 6 nm is proper to investigate the sintering kinetics [10], [18]–[20]. Accordingly, as shown in Fig.2.1 the first model consisted of nine Cu NPs with a diameter of 4 nm in 3×3 array was built. Then for the study of particle size effect, 3 nm and 5 nm Cu NPs models were developed as well. For all models, two copper layers were set above and below the particle array to imitate the backside metallization layer of the chip and the metallic surface of the substrate, as the color purple parts shown in Fig.2.1.

For descriptive convenience, the three layers of 3×3 copper NPs array are named as L1, L2 and L3 from top to bottom as shown in Fig.2.1. Within each layer, the particles are further labeled according to the order, for example, L1-P1, L1-P2 and L1-P3. In addition, the initial distance between NPs was usually set within 2-5 Å[5]. Correspondingly, in this study, the space between NPs is set as 3.61 Å, which is equal to the lattice constant of Cu. In addition, the Cu (111) plane was set as the substrate plane towards the NPs due to its lowest surface energy [14]. In order to avoid the particle spontaneous coalescence prior to the particle-substrate sintering, there was an initial 3 Å gap between the substrate and the NPs.

We preset a small initial velocity (1Å/ps, -z direction) to the atoms in the first two layers of the upper substrate. The purpose of this setting is first to imitate the downward movement tendency caused by the gravity of the upper substrate (chip) and also to accelerate the simulation process. In order to avoid the influence of the random fluctuation motion of the substrate, we fixed the coordinates of the downmost two layers of the lower substrate. In all simulations, periodic boundary conditions were applied in three dimensions. A time step of 1 fs was set for for calculation and the positions as well as velocities of each Cu atoms were recorded every 1 ps.

2.2.2. TEMPERATURE PROFILE

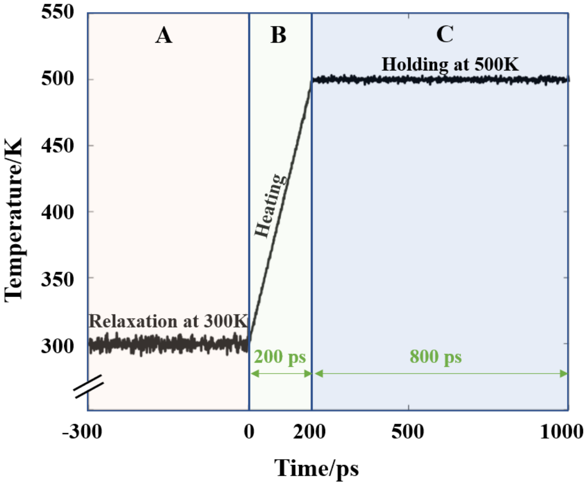

Figure 2.2: Temperature profile of sintering process at 500 K. *Phase A* is the relaxation process. *Phase B* is the heating and sintering process. *Phase C* is the holding process at peak temperature for another 800 ps.

As shown in Fig.2.2, the temperature profile in this study can be divided into three phases. In ***Phase A***, a relaxation process of 500 ps at a low temperature of 300 K in the NVT ensemble must be performed first to obtain the equilibrium initial structure of the constructed model before sintering. Then in ***Phase B***, the system was heated up by 1K/ps for another 200 ps to 500K, in which the study of the coalescence kinetics of the NPs-substrates model was conducted. Here we define the beginning of *Phase B* as time zero to facilitate the discussion in the following sections. Finally in ***Phase C***, when it reached 500K, the 3 nm, 4 nm and 5 nm as-sintered models were then held at 500K for another 800 ps to reach their equilibrium state.

It is found that the microstructure and diffusion behavior of the model essentially remain unchanged throughout ***Phase A*** and ***Phase C***, but change dramatically in ***Phase B***. Therefore, in this chapter, when studying the dominant mechanism in the low-temperature sintering case, we will focus mainly on the phenomena in ***Phase B***. When studying the effect of particle size on the sintering process, we will focus on the whole heating and holding process (***Phase B*** + ***Phase C***).

2.2.3. DATA RECORDING AND ANALYZING METHODS

OVITO software was applied to visualize the atomic configurations and analyze the dislocation conditions. To describe the shrinkage of the sintering model, the Shrinkage Ratio (SR, ζ_x) was applied. The SR for L1, L2, L3 are named as $\zeta_{x,L1}$, $\zeta_{x,L2}$, $\zeta_{x,L3}$. The corresponding definitive equation is as follows:

$$\zeta_x = \Delta L/L_0 = (L_0 - L_t)/L_0 \tag{2.1}$$

where L_0 is the initial distance between particles in each layer and L_t is the corresponding distance at moment t.

As previously mentioned, CNA and DXA analysis tools were used to analyze the crystal structures and dislocations evolution, respectively [21], [22]. Before using the method, the cutoff radius (r_{cut}) needed to be set, which is always calculated as below for face-centered cubic (FCC) structures:

$$r_{cut}^{fcc} = \frac{1}{2}(\sqrt{1/2}+1)a_{fcc} \simeq 0.854a_{fcc} \tag{2.2}$$

where, a_{fcc} is the lattice constant of the corresponding atom in FCC structure. Therefore, in this work, the cutoff radius of Cu is 3.08 nm.

The contribution of the atomic (mass) transportation on the coalescence mechanism was estimated by analyzing the MSD of the system[23], [24]. Both atomic diffusion and plastic deformation can affect this parameter. The definition equation is as follows:

$$\langle d^2 \rangle = \left\langle \left\{ \left[r_{(t_0+\tau)} - r_{com(t_0+\tau)} \right] - \left[r_{(t_0)} - r_{com(t_0)} \right] \right\}^2 \right\rangle \tag{2.3}$$

where t_0 is the initial time, τ is the observation moment, $r_{(t0)}$ is the coordinates of the atom at time t_0, and $r_{com(t0)}$ is the centroid coordinates of the particle. $r_{(t0+\tau)}$ is the atomic coordinates of the atom at time τ, and $r_{com(t0+\tau)}$ is the particle centroid coordinates of the atom at time τ. <> is the ensemble average computing operator.

2.3. Coalescence Kinetics of NPs-Substrates Model

It is known from classical sintering theory that the driving force of sintering is the reduction of the free energy of the system. This is achieved through the reduction of the total specific surface area and total surface free energy of NPs, the reduction of pore volume and total surface area within the sintered body, and the elimination of lattice distortion within the particles. The purpose of this work is to investigate the effect of particle-to-particle and substrate-to-particle interactions on the above mechanism.

In this section, the different sintering stages will be distinguished based on the data curve results in Fig.2.3. Then, the slope of the MSD curves will be analyzed to determine the degree of the sintering process proceeding. Then the microstructure transient snapshot will be used to observe the sintering neck growth. After that, the driving force of the sintering process will be analyzed in conjunction with the trend of crystal type and dislocation density evolution. Finally, the macroscopic behavior of the model is described based on the transverse and longitudinal shrinkage rates. With this particular model, the influence of atomic diffusion and plastic deformation on the sintering process will be discussed, while also focusing on the role of the substrate.

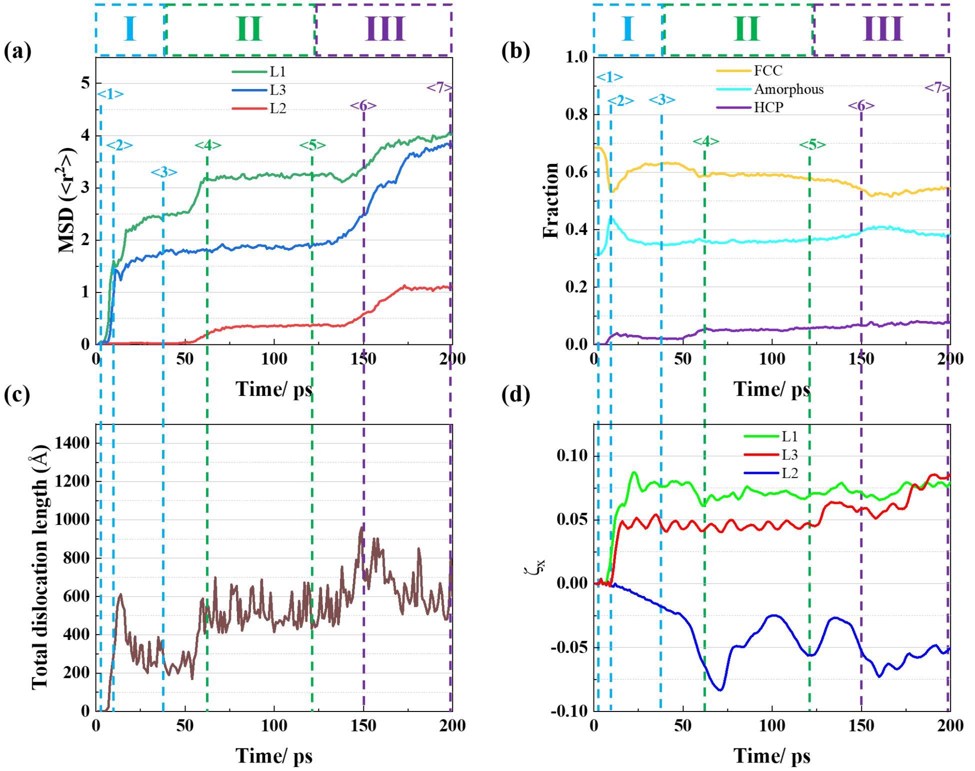

Figure 2.3: (a) The MSD curves for L1, L2 and L3. (b) The FCC, HCP and amorphous fraction evolution. (c) The dislocation density evolution. (d) The shrinkage ratio evolution of L1, L2 and L3.

To begin with, the 4 nm model was adopted to study the coalescence kinetics of the

NPs-substrates model. The whole sintering process can be divided into three stages for the model of 4 nm based on the MSD results, microstructural fraction, dislocation density and shrinkage ratio as shown in Fig.2.3, which are:

Stage I:

- 0~40 ps (blue box), sintering of L1, L3 particles with the substrates.

Stage II:

- 40~120 ps (green box), sintering between L1 and L2 particles.

Stage III:

- 120~200 ps (purple box), sintering between L2 and L3 particles.

As mentioned in the previous section, OVITO was applied to conduct an in-depth microstructural analysis. The analysis tools CNA and DXA are employed to analyze the crystal structure and dislocations evolution, respectively. In Fig.2.4, Fig.2.5 and Fig.2.6, the atomic configurations of L1, L3 particles during *Stage I*, *Stage II* and *Stage III* are shown. We assigned different colors to the Cu atoms of the particle and substrate to facilitate the observation of different behaviors of the particle, substrate, and interface, as illustrated in Fig.2.4.

2.3.1. STAGE I

IN this section, the NPs sintering process and mechanism in *Stage I* was discussed. From 2 ps at position <1>, when the upper substrate started to contact with the L1 particles with its initial velocity of 0.067 Å/ps. In the MSD results in Fig.2.3, the slope of the L1 and L3 curves from position <0> to position <1> are gradually increasing from near horizontal. It indicates that the system was undergoing a migration process from a steady state to mass transportation. Then by observing the atomic configurations at position <0> and <1> in Fig.2.4, it is found that the particles in L1 and L3 just contacted with the corresponding top and bottom substrates, and lots of amorphous atoms appeared at the interface between the particles and the substrate. After this, the atomic vibration amplitude increased under the effect of evaluated temperature, which led to the occurrence of atomic diffusion and allowed more atoms to enter the atomic force range. A repositioning of the atoms on the contact surface occurred, while the atoms of the particle and substrate were converted from mechanical contact to crystalline bonding. Also at this position, the sintering necks formed and grew fast on the substrate-particles interface. The neck size was around 2.1 nm in the L3-substrate interface and 2.6 nm in the L1-substrate interface.

Next, by analyzing the crystal transition curves and atomic configuration graphs, the reasons for the rapid formation and growth of the sintered neck at this period could be obtained. From Fig.2.3b it can be found that there was a small amount of the FCC atoms disappeared during this period. This is accompanied by the production of a small number of amorphous atoms and hexagonal close-packed (HCP) atoms. The amorphous atoms came from the mass transportation from the volume to the necking region during the sintering process. These HCP atoms were supposed to be generated in L1 and L3 as the light green dots shown in Fig.2.4b and f. It is deduced that when NPs contact with substrate, the compress stress will first cause plastic deformation by generating stacking fault (SF) with small partial dislocation near the necking region, as shown in Fig.2.4a and b. Apparently, the neck of L1 consisted of more SF than that of L3 at this period, because the motion of the upper substrate caused higher compressive force to the L1 particles. Thus, a higher driving force was provided through more plastic flow in L1.

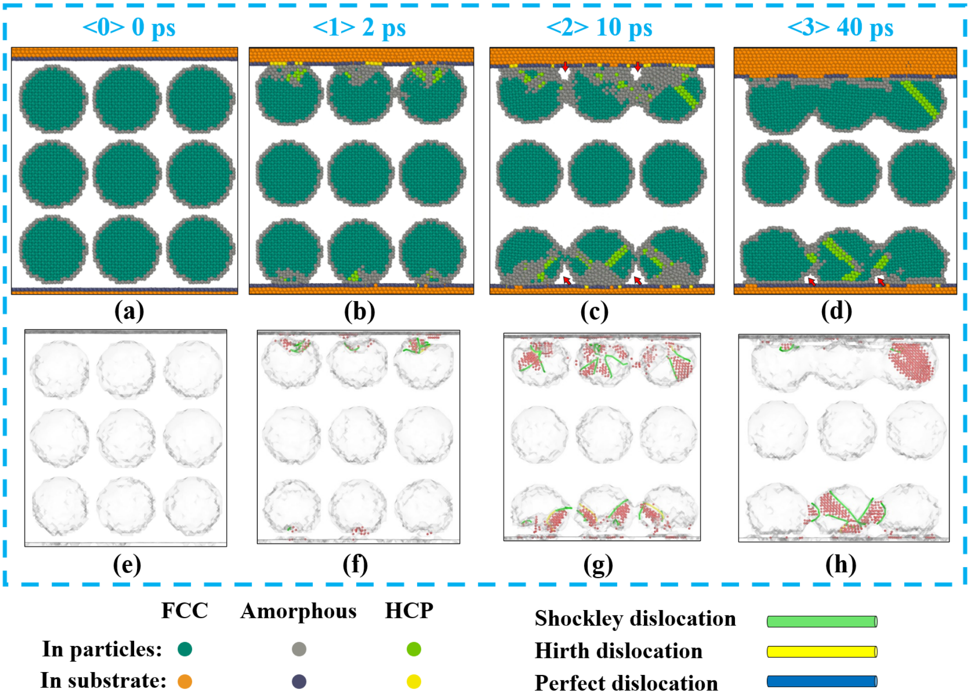

Figure 2.4: Cross-section and dislocation distribution snapshots of 4 nm model in *Stage I*. (a) - (d) Cross-section snapshots at 0 ps, 2 ps, 10 ps and 40 ps. (e)-(h) HCP and dislocation distribution snapshots at 0 ps, 2 ps, 10 ps and 40 ps. *Type-α* pores were marked with red arrows.

Then from position <1> to position <2> was the stage of the rapid growth of the neck, when the neck size was increased to 3.18 nm for the L3-substrate and 3.64 nm for L1-substrate over the time. During this sintering stage, necking growth occurred mainly through surface diffusion, grain boundary diffusion, and plastic flow. MSD curves in Fig.2.3a show extremely large increasing slopes for L1 and L3 during this period, which implies a drastic atomic migration process. According to the study of Chen et al.[3], this anomalously large slope indicates the much faster plastic deformation-induced atomic motion, which is not possible to be provided by surface diffusion alone. Therefore, the plastic flow was supposed to be the dominant coalescence mechanism at this stage. To verify this hypothesis, the atomic configurations and the crystal fraction evolution at position <2> were analyzed. The sharpest valleys and peaks in Fig.2.3b indicate that a tremendous number of FCC atoms began to transform into amorphous and HCP atoms. Combined with the information from Fig.2.3c and Fig.2.4g, we found that the SF grew rapidly and partial dislocations elongated a lot in both L1 and L3 layers. In addition, there were some stair-rod dislocations due to dislocation motion. These findings indicate that severe plastic deformation occurred in these regions. In addition, from Fig.2.4c, it can be observed that interlayer particle contact within the L1 and L3 layers occurred and small necks among Cu NPs also started to form. The neck sizes between particles in L1 and L3 were only 0.76 nm and 1.35 nm at this moment. The positive $\zeta_{x,L1}$ and $\zeta_{x,L3}$ values in Fig.2.3d indicate that, the L1 and L3 particles did not shrink along the horizontal direction, but rather expanded. By observing the Fig.2.4c, it shows that the L1 and L3 particles were fixed by the corresponding substrates and therefore it was difficult to have significant horizontal shrinkage. However, despite this, the growth of sintering necks and the decrease of the pores were still promoted by surface diffusion and grain boundary diffusion of adjacent particles after contact.

Finally, from position <2> to position <3> the sintering of L1 and L3 particles with their adjacent substrate entered the final step. The slope of MSD curves (Fig.2.3a) became smaller, which represented the slowdown of atomic migration. First, it can be assumed that the plastic flow driving force due to the impact of the top substrate on the L1 particles has been consumed by forming the large necks between L1 and the substrate. Therefore, no significant dislocation generation can be observed from the dislocation density graph in Fig.2.3c and DXA graph in Fig.2.4h. Then due to the formation of the stair-rod dislocations in position <2>, the further motion of the dislocations was hindered. Thus, the transition from plastic deformation-induced atomic motion to the surface diffusion of atoms occurred at this stage.

Now it is possible to summarize the influence of the substrate on the sintering of the Cu NPs. In general, the main force between the particles and the substrate at the starting period came from the Van der Waals force, which is also the driving force for the L3 particles and the bottom substrate to approach each other. In the present work, the downward motion of the top substrate not only accelerated the approach between the L1 particles and the top substrate, but also caused downward directional pressure on the L1 particles, which could significantly facilitate the sintering process by inducing the plastic flow mechanism. Furthermore, the pinning effect of the substrate on the NPs led to a slowing down of the shrinkage of the particles in the horizontal direction, and also led to the formation of pores. Fig.2.4c and d demonstrate that small pores (*Type-α* pore) formed around the particle-substrate necking region and then vanished first at the top substrate region. The necking groove contained symmetrical curvature at the beginning. However, most of the atoms moved to the side where the pores used to be. This is due to the fact that the reduction in pore volume and total surface area inside the sintered body is also an effective driving force for sintering. Accordingly, it is believed that the diffusion in the final moments was driven by the removal of free surfaces in these pores. At the end of this stage, the reduction of the free surface due to the necking growth of L1 and L3 particles reached a bottleneck. As a result, the ζ_x of L1 and L3 started to vibrate more or less periodically. It is important to note that although there was initially no misorientation between the particles of L1 or L3, they must undergo rigid rotation as a complementary mechanism for crystal arrangement due to the pinning effects of the substrate. The details about the rotation behavior would be discussed in the next section.

2.3.2. STAGE II

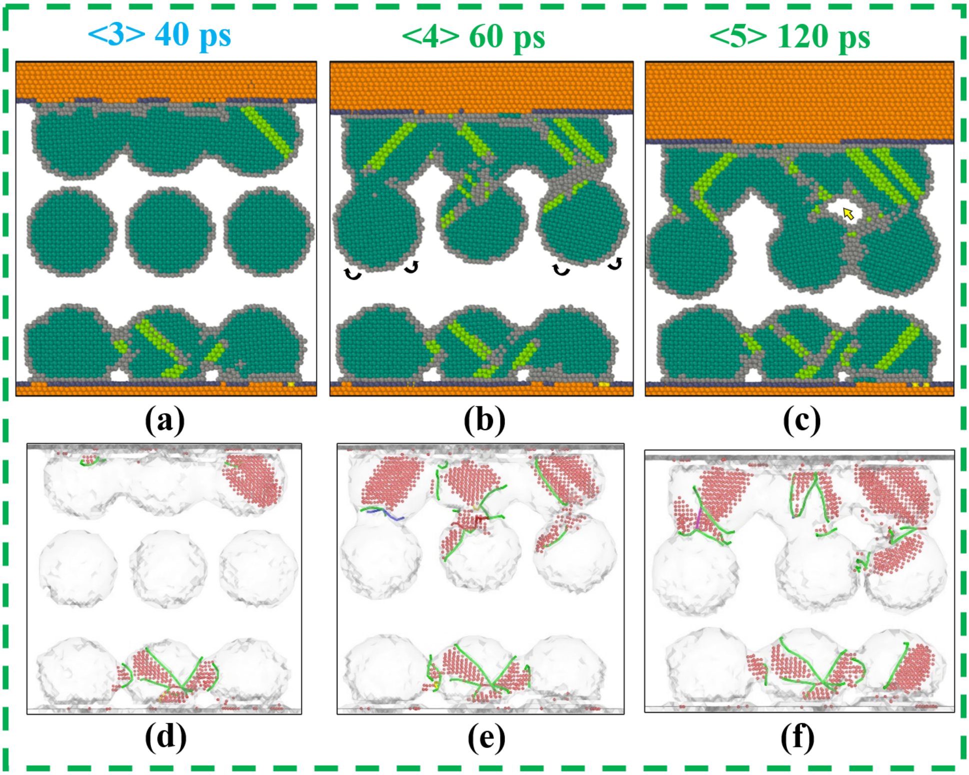

Figure 2.5: Cross-section and dislocation distribution snapshots of 4nm model in *Stage II*. (a) - (b) Cross-section snapshots at 60 ps and 120 ps. (e)-(h) HCP and dislocation distribution snapshots at 60 ps and 120 ps. *Type-β* pores were marked with yellow arrows.

FROM position <3> to position <5> is defined as the *Stage II*, during which the L1 and L2 particles started contacting and sintering with each other. MSD curve in Fig.2.3a reveals that the *Stage II* can be further divided into two phases, one on the left and one on the right of position <4>. From position <3> to <4>, the MSD curve of L3 remains horizontal, indicating a steady state without significant mass transportation. The atomic configuration images in Fig.2.5a to b and d to e also confirm that the L3 particles have basically completed sintering at this temperature, and no further changes in the sintered neck, pores and dislocations can be found. However, both the green and red MSD curves for L1 and L2 contained large rising slopes, which implies a drastic atomic migration process between 40 ps to 60 ps. Fig.2.3b and c show that some FCC atoms transformed into HCP as well as a small number of amorphous atoms, and the dislocation density raised again at the same time. Fig.2.5d and f illustrate that dislocations were generated from the interface and slipped along the dense plane into the particle body. Such phenomena prove that there was also an additional driving force for the sintering process between L1 and L2 in addition to the reduction of total surface free energy, due to the collision effect between L1 and L2 particles. Finally, from position <4> to <5>, the MSD curves for L1 and L2 reduced to a plateau till the end of this stage which indicates the atomic migration was becoming less significant.

As depicted in Fig.2.4d and Fig.2.5, the horizontal shrinkage within L1 and L3 was almost complete at this stage. However, for L2, there was a noticeable shrinkage that occurred between <3> and <4>, but then a little expansion took place between <4> to <5>. As is mentioned in *Stage I*, the L1 particles would have a rigid rotation for crystal alignment with the atoms in the substrate. Consequently, when particles in L2 contacted with particles in L1, the particles in L2 would also rotate themselves by plastic deformation induced force via dislocation gliding and even slip across the grain boundary[3], [9], [25]. Additionally, it is also found that, when sintering neck between L1 and L2 were formed (at the end of *Stage II*), there were elastic oscillations of L2 particles (as shown in Fig.2.5b) towards left and right. The same phenomena have been reported in other studies[26]. Both of these rotational effects are critical, since they can further randomly decide the interlayer coalescence of three particles in L2. In other words, when two particles in L2 are contacted and sintered together, the other one will be isolated. In this work, the L2-P2 and L2-P3 coalesced to form the sintering networking due to the random rotation, whereas the L2-P1 was the isolated one. After the formation of a such four-particle network for L1-P2, L1-P3, L2-P2 and L2-P3, the structure was fixed. Their further alignment rotation was hindered and hence the misorientation within the network will persist for a long time along with the presence of high-energy grain boundaries. In the middle site of the network, a large pore could be observed, which was referred to as *Type-β* pore in this study. The details about different pores will be discussed in the following sections.

2.3.3. STAGE III

At *Stage III* (position <5> to <7>), it is found that the L3 particles were compressed by the corresponding L2 particles, forming the final sintering network with all three layers and two substrates, as displayed in Fig.2.6. At the moment between position <5> and <6>, the L2 particles started to contact with L3 particles. Along with the huge compressive stress to the L3 layer given by the substrate-L1-L2 system, a large number of SF and dislocations were produced in the L3-particles and necking regions by the dissociation of the stair-rod dislocation as shown in Fig.2.6d, e and f. Then, with the extension of SF, the neck size between L2-particles and L3-particles grew rapidly. From Fig.2.6e and f, most of the dislocations glided to the interfaces between the particles in different layers, forming the grain boundaries. As plotted in Fig.2.3a, there were raising MSD slopes around position <6> for all three layers. Also, the increase in dislocation density and decrease of FCC atoms can be found in Fig.2.3b and c. It is deduced that the atomic migration mechanism for the sintering at this stage included the plastic flow, surface diffusion, and grain boundary diffusion. The driving forces for the atomic diffusion were supposed to be the reduction of the free surface area and the vanishment of the pores. Accordingly, the *Type-α* pore on L1-substrate interface and L3-substrate interface completely disappeared. Moreover, the *Type-β* pores between adjacent layers, and the giant *Type-γ* pores became smaller. Finally, the plastic flow was almost complete near the end of *Stage III* with the decreasing of dislocation density and HCP amount till 200 ps. The MSD curve for all layers came to a plateau, indicating the weakening of atomic diffusion.

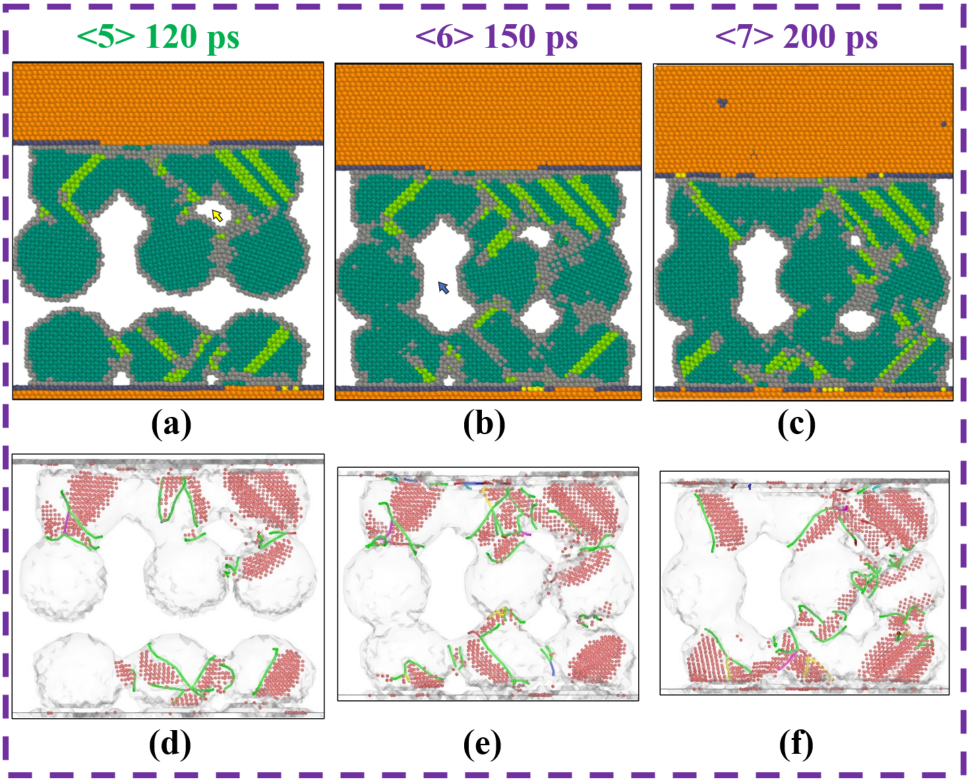

Figure 2.6: Cross-section and dislocation distribution snapshots of 4 nm model in *Stage III*. (a) - (d) Cross-section snapshots at 150 ps and 200 ps. (e)-(h) HCP and dislocation distribution snapshots at 150 ps and 200 ps.

In summary, based on the above-mentioned results, it is found that:

1) In this model, the dominating sintering mechanism when two particles contact with each other was plastic flow caused by the production and motion of dislocations.

2) The compressive effect provided by the upper substrate can significantly accelerate the sintering behavior of upper NPs layers by amplifying the plastic flow.

3) Due to the misorientation alignment tendency, there was rigid rotation of as-sintered NPs. The rigid rotation of one particle might then cause random misorientation and elastic oscillation of lately contacted particles.

4) The pinning effect of the substrate on the corresponding particles might expand such random effect of lately contacted particles (in this case, L2 particles), which would produce huge pores (*Type*-γ).

5) Small pores (*Type*-α and *Type*-β) can vanish via both plastic deformation and surface diffusion. This served as a complement to the driving force for the neck growth when the plastic deformation mechanism was weakened.

2.4. PORES EVOLUTION AND ROTATION BEHAVIOR

2.4.1. PORES EVOLUTION BETWEEN NPS AND SUBSTRATES

GENERALLY, three types of pores were found in this system, as shown in Fig.2.7. According to the different formation approach and the size of the pores, they are designated as *Type-α*, *Type-β*, *Type-γ* pores. The *Type-α* pore is generated between the as-connected NPs and substrate surface. This type of pore also appeared in other studies, and it was found that the driving force for the diffusion of the atoms around it is the decreasing of extra free surface energy caused by the necking region[7]. At low temperatures, however, diffusion is hard to be activated, and thus Type-α pores cannot be quickly filled in this way. This effect is also valid for Type-β pores, which were created in the middle site of four-particles sintering network. In this study, the plastic deformation of L1 particles caused by the pressure from the upper substrate may assist the filling of both Type-α and Type-β pores.

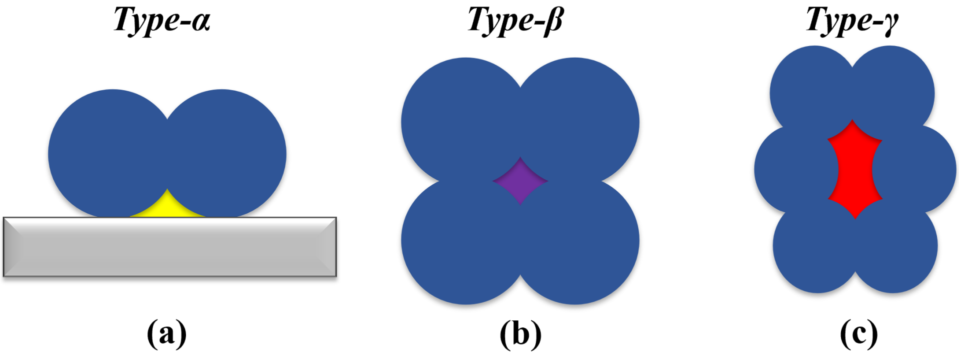

Figure 2.7: The schematic diagram of the three types of the pore. (a) The Type-α pore marked with yellow color is surrounded by a substrate and double particles. (b) The Type-β pore marked with purple color is surrounded by four particles. (c) The Type-γ pore marked by red color is generated by misorientation of between NPs.

The Type-γ pore is the largest one, which was formed due to the misorientation of the particles in L2 with respect to the particles in L1 and L3. For crystal alignment, the L2 particle rotated at a small angle after forming a neck with the L1 particle, which created a large gap to its adjacent L2 particles. Since too many particles were involved in the formation of the Type-γ pore, it was difficult to effectively vanish this pore neither by self-motivated surface diffusion nor the low-pressure plastic flow. Therefore, it will be feasible to use higher temperature or higher assisted pressure in practice to improve the atomic diffusion behavior and plastic deformation in order to decrease the size of *Type-γ* pores.

2.4.2. ROTATION BEHAVIOR OF NPS AFFECTED BY THE SUBSTRATE

IT has been reported[27]–[29] that when solid-phase sintering was performed at low temperature, the nanoparticles would undergo rigid rotation after the formation of sintering necks to adjust the lattice mismatch between the particles, thereby eliminating lattice distortion and further reducing the system energy. Some studies[28], [29] have also found that relative rotation occurred after sintering neck formation when there was initially no lattice mismatch between two smaller-sized particles. This was because small-sized particles could form crystal bonds very quickly after initial contact, but as the sintered neck grew, the vigorous atomic motion in this region would then lead to crystal transition back to the amorphous state. After the growth of the sintered neck was nearly complete, the mismatch between the lattices would be compensated by the rotational motion of the NPs again. It can be found that the rotational dynamics of NPs mainly come from the energy reduction by solving the lattice mismatch that arises after neck growth. A similar rotational mechanism is found in the models studied in this chapter. However, at the same time, the classical rotational behavior has been affected by the substrates. In this section, we investigated the rotational behavior of the particles in this sandwich model by recording the atomic trajectories of the particles in each layer.

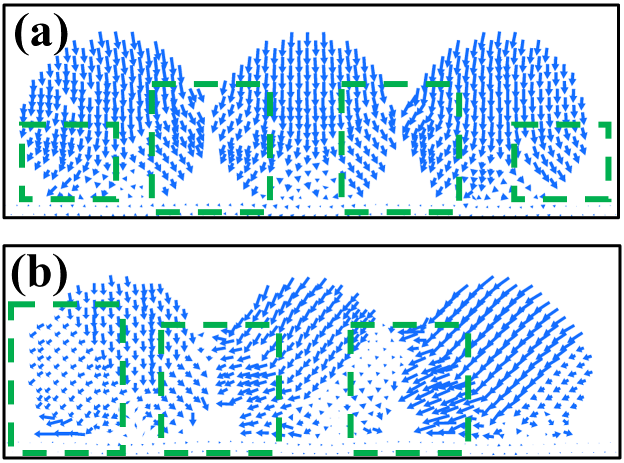

Figure 2.8: Displacement vectors of the atoms in L3 particles at (a) 10 ps and (b) 60 ps.

Fig.2.8 shows the displacement vectors of the atoms in L3 particles at 10 ps and 60 ps. It can be found that at 10 ps most of the atoms in each particle had a tendency to move downward due to the growth of the sintered neck between the particle and substrate. A small number of atoms had a tendency of lateral motion, leading to a small angular rotation of the particles at the macroscopic level. This rotation is in accordance with the previously introduced misorientation-induced rule. At around 60 ps, because of the dynamics of the sintered neck growth between the particles in L3, a more pronounced lateral displacement of atoms between adjacent atoms can be observed. However, further approaching movement between L3 particles was hindered by the pinning effect of the substrate. It eventually led to a partial rotation of each particle, rather than a rotation of the whole body, as highlighted by the green dot box in Fig.2.8. Plastic deformation in each particle occurred through the formation of SF and sliding of partial dislocations. This passive rotational behavior did not effectively resolve the crystal lattice mismatch due to the pinning effect of the substrate, but left some amount of SF at the interface between the particles after sintering as shown in Fig.2.4, Fig.2.5 and Fig.2.6.

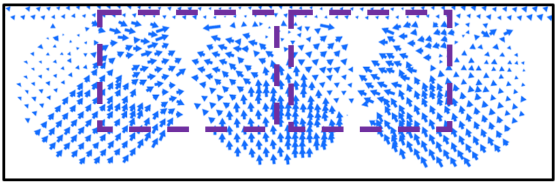

Figure 2.9: Displacement vectors of the atoms in L1 particles at 10 ps.

Fig.2.9 and Fig.2.10 present the rotation behavior of L1 particles at 10 ps and L2 particles at 60 ps. Similarly as L3 particles, the initial rotation of L1 particles also followed the misorientation-induced rule and was impeded by the substrate, as shown in Fig.2.9. The pressure provided by the upper substrate caused plastic deformation of the L1 layer particles by longitudinal shrinkage and lateral expansion, which promoted the contact of the particles within the layer and the formation of the sintered neck between particles. Therefore, the above-mentioned passive rotation did not occur in L1 particles, and no obvious dislocations were found on the sintered neck between the particles.

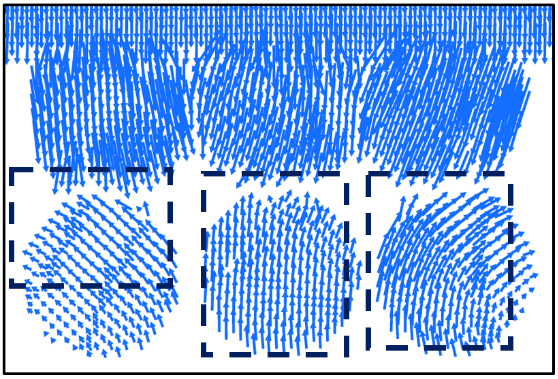

Figure 2.10: Displacement vectors of the atoms in L2 particles at 60 ps.

For the constraint-free L2 particles, they also followed the misorientation-induced rotation rule. At 10 ps, the L2 particles were not touched by other particles, and thus there was no rotation behavior for them yet. Till 60 ps as shown in Fig.2.10, the L2 particles contained obvious rotation motion with respect to the L1 particles. The misorientation between the L2 particles and L1 particles came from the rotation of L1 particles with respect to the substrate. After the formation of the sintering neck between L1 particles and L2 particles, the dislocation would glide across the L2 due to the surface stress around the neck. It is worth noting that, the rotation is not uniformly distributed within each L2 particle. More rotation was observed on the part that was close to the L1 particle. In this way, SF and partial dislocations were generated inside of the L2 particles.

2.5. SIZE EFFECT OF NPS ON THE SINTERING MECHANISM

To investigate the effect of particle size on sintering kinetics in this proposed system, models of 3 nm, 4 nm and 5 nm Cu NPs were applied. All three models were sintered with the same temperature profile introduced in the methodology section. The atomic configuration, dislocation evolution, horizontal and vertical shrinkage ratio, and crystalline fraction change were studied respectively. Fig.2.11 shows the cross-section snapshots and defects distribution of different models (from left to right). The sintering process of the three models was also divided into three stages (from top to bottom) according to the corresponding microstructure variation. It can be found that the model of smaller NPs contained larger necking size and smaller pores at each stage. Atomic activation was extremely easy in the model with the smallest particle size (3 nm) at 500K to start the mass transportation and form a dense structure. In its sintered body, basically, no pores of any type were found. However, in the 5 nm model, all three types of pores were observed, including the one formed with the top substrate. The filling of different types of pores in larger particles was difficult, which required longer aging times or higher sintering temperatures.

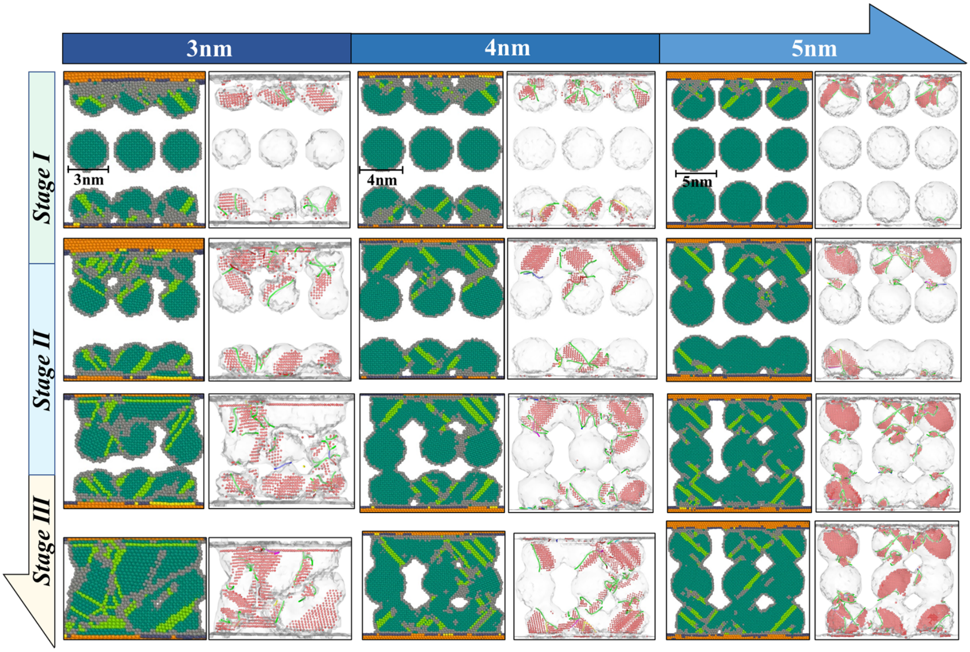

Figure 2.11: Cross-section and dislocation distribution snapshots of different models in different stages. From left to right are models for 3 nm, 4 nm and 5 nm particles. From up to bottom are *Stage I*, *II* and *III*.

Fig.2.12 shows the fraction of different crystal structures and the dislocation density evolution for the models with different particles size. It reveals that small-sized particles contained more amorphous atoms and fewer FCC atoms at the beginning than larger particles, since they had higher specific surface area. In addition, more drastic crystal transitions and dislocation evolution can be found for the smaller model at each stage. In the 3 nm model, more SF (HCP atoms) presented across the particle at *Stage I* as shown in Fig.2.11 and Fig.2.12, indicating more plastic deformation-driven neck growth.

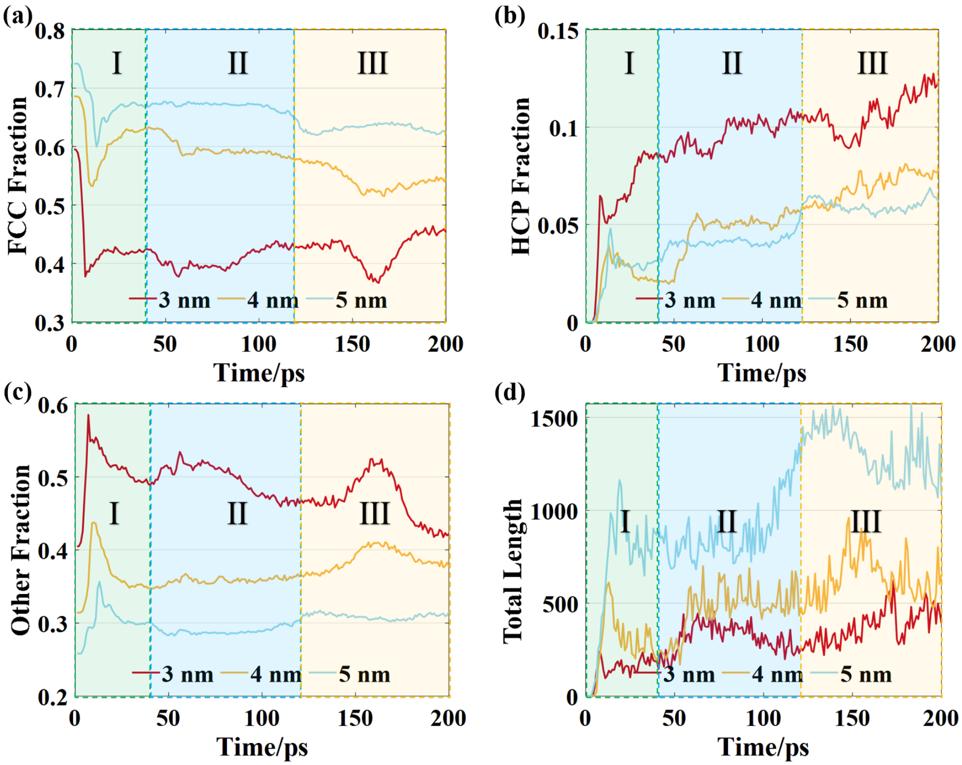

Figure 2.12: Macro- and microstructural evolution during 200ps sintering for 3nm, 4nm and 5nm models.(a) to (c) The diagram of FCC, HCP and amorphous fraction changes over time. (d) The dislocation density.

However, in the larger-size model, more stair-rod dislocations appeared in some particles as shown in Fig.2.11, which hindered the dislocation movement and plastic deformation. At the same time, partial dislocations were generated in each model. In *Stage II* and *III*, the 3 nm model again shown better ability for the plastic flow, and finally, most of dislocations glided into the grain boundaries and annihilated due to the recovery process (as drop shown in dislocation density curve) forming a dense and strong structure. In 4 nm model, the stair-rod dislocation was finally unlocked by the compressive pressure from the L1 and L2. Most of the dislocations also glide towards the grain boundaries. However, for the 5 nm model, the force might be insufficient for the dissociation of the pinned stair-rods dislocations since the upper substrate in each model had the same initial moving velocity and therefore the same compressive force to the particles. Therefore, most of stair-rod dislocations stayed at their original location. It is worth noting that for each model the final increase in dislocation density was attributed to crystal alignment between L2 and L3.

Finally, from E_z, E_{xL1} and E_{xL3} curve (Fig.2.13) it shows that smaller-size models usually contained higher shrinkage ratio which is in line with previous studies [3], [28], [29]. Specifically, in the 3 nm model, the L1 layer had around 18% shrinkage ratio which is much higher than that for 4 nm model (9%) and 5 nm model (-5%). Interestingly, there are negative shrinkage values in the L1 layer of 5 nm and the L2 layer of 4 nm. This could be caused by the rigid rotation and randomly elastic oscillation of L1 which has been discussed in the previous sections.

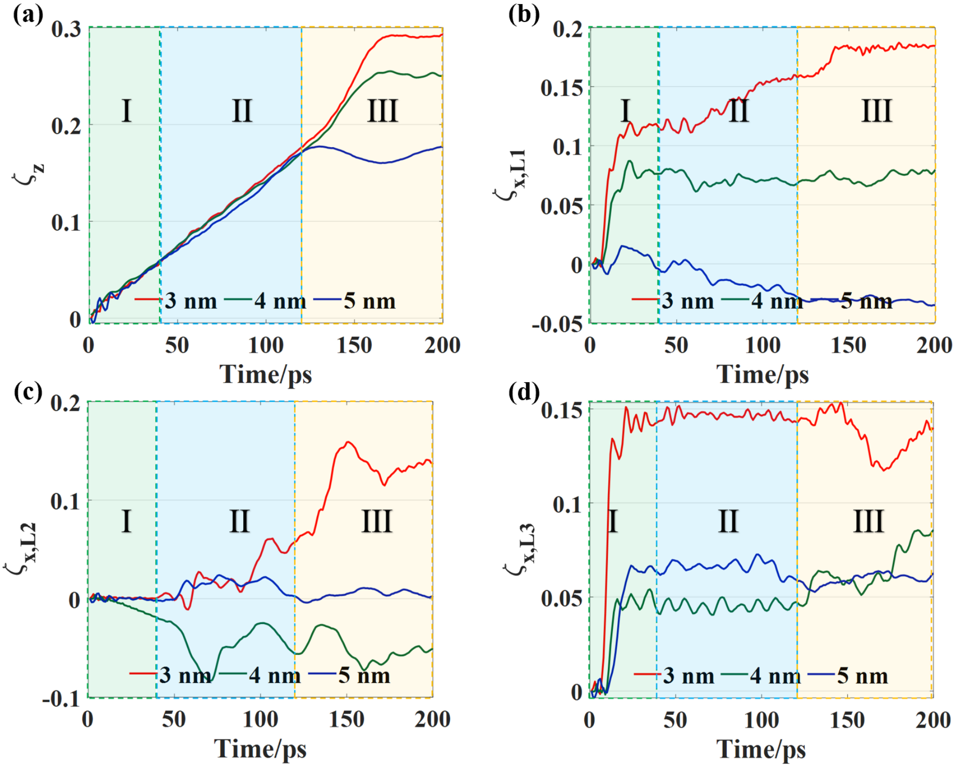

Figure 2.13: Macro- and microstructural evolution during 200ps sintering for 3nm, 4nm and 5nm models. (a) to (d) The vertical and horizontal shrinkage of L1, L2 and L3.

2.6. CONCLUSION

In this chapter, the coalescence kinetics and microstructure evolution of Cu NPs sintering process between two substrates at low temperature were investigated by MD simulation. The crystal structure, atomic diffusion, dislocation behavior and porous defects were studied by using OVITO tools, MSD curves, CNA and DXA analysis. It was found that the dominant sintering mechanism for the particles without applied pressure at low temperatures was mainly surface diffusion. However, when the pressure effect of the upper substrate on the particles was introduced, the dominant sintering mechanism of the particles changed to plastic flow induced by dislocation production and motion in the particles. In addition, the spontaneous rotation of particles occurred during the coalescence to eliminate the inter-particle lattice mismatch, while the passive rotation behavior of the L3 particles also occurred due to the pinning effect of the substrate. Apart from that, the pinning effect also created giant pores between particles and substrates. Some of these pores can be filled via both plastic deformation and surface diffusion of atoms for the smaller particles. Finally, to investigate the size effect on the sintering kinetics, the atomic motion and microstructural evolution of 3 nm, 4 nm and 5 nm models were compared. It was found that the models of smaller size particles typically contained higher shrinkage ratios, larger sintering necks and smaller pores. More severe atomic motion, and more drastic crystal structure transitions at each stage were found in smaller size particles. The research results show that the sintering densification and pores structure could be improved by using the applied pressure in the sintering process. Particle sintering progress was greatly accelerated by enhancing the plastic flow mechanism. However, attention should also be paid to the problems such as rotational residual stresses brought about by the pinning effect of the substrate, which may require further heat treatment to eliminate.

REFERENCES

[1] S.-J. L. Kang, *Sintering: densification, grain growth and microstructure*. Elsevier, 2004.

[2] S. Paul, S. Mitra, D. Roy, *et al.*, “Molecular dynamics simulation study of neck growth in micro-selective laser sintering of copper nanoparticles”, in *Simulations for Design and Manufacturing*, Springer, 2018, pp. 259–292.

[3] B. Cheng and A. H. Ngan, “The sintering and densification behaviour of many copper nanoparticles: A molecular dynamics study”, *Computational materials science*, vol. 74, pp. 1–11, 2013.

[4] J. Guo, C. Xu, A. Hu, *et al.*, “Sintering dynamics and thermal stability of novel configurations of ag clusters”, *Journal of Physics and Chemistry of Solids*, vol. 73, no. 11, pp. 1350–1357, 2012.

[5] D. Hu, Z. Cui, J. Fan, X. Fan, and G. Zhang, “Thermal kinetic and mechanical behaviors of pressure-assisted cu nanoparticles sintering: A molecular dynamics study”, *Results in Physics*, vol. 19, p. 103 486, 2020.

[6] L. Yang, Y. Gan, Y. Zhang, and J. Chen, “Molecular dynamics simulation of neck growth in laser sintering of different-sized gold nanoparticles under different heating rates”, *Applied Physics A*, vol. 106, no. 3, pp. 725–735, 2012.

[7] F. Wakai, O. Guillon, G. Okuma, and N. Nishiyama, “Sintering forces acting among particles during sintering by grain-boundary/surface diffusion”, *Journal of the American Ceramic Society*, vol. 102, no. 2, pp. 538–547, 2019.

[8] C. Li, D. Li, X. Tao, H. Chen, and Y. Ouyang, “Molecular dynamics simulation of diffusion bonding of al–cu interface”, *Modelling and Simulation in Materials Science and Engineering*, vol. 22, no. 6, p. 065 013, 2014.

[9] B. Cheng and A. H. Ngan, “Crystal plasticity of cu nanocrystals during collision”, *Materials Science and Engineering: A*, vol. 585, pp. 326–334, 2013.

[10] H. Dong, K.-S. Moon, and C. Wong, “Molecular dynamics study on the coalescence of cu nanoparticles and their deposition on the cu substrate”, *Journal of electronic materials*, vol. 33, no. 11, pp. 1326–1330, 2004.

[11] M. Meddad, M. Badawi, M. Mazroui, *et al.*, “Sintering and deposition of homo- and heteronanoparticles of aluminum and nickel on aluminum (100) substrate”, *Chemical Physics*, vol. 541, p. 111 037, 2021.

[12] L. Zhan, X. Zhu, X. Qin, M. Wu, and X. Li, “Sintering mechanism of copper nanoparticle sphere-plate of crystal misalignment: A study by molecular dynamics simulations”, *Journal of Materials Research and Technology*, vol. 12, pp. 668–678, 2021.

[13] J. Wang, S. Shin, A. Hu, and J. K. Wilt, “Diffusion kinetics of transient liquid phase bonding of ni-based superalloy with ni nanoparticles: A molecular dynamics perspective”, *Computational Materials Science*, vol. 152, pp. 228–235, 2018.

[14] D. Ishikawa, B. N. An, M. Mail, *et al.*, “Bonding strength of cu sinter die-bonding paste on ni, cu, ag, and au surfaces under pressureless bonding process”, *Transactions of The Japan Institute of Electronics Packaging*, vol. 13, E19–017, 2020.

[15] S. Plimpton, “Fast parallel algorithms for short-range molecular dynamics”, *Journal of computational physics*, vol. 117, no. 1, pp. 1–19, 1995.

[16] M. S. Daw and M. I. Baskes, “Embedded-atom method: Derivation and application to impurities, surfaces, and other defects in metals”, *Physical Review B*, vol. 29, no. 12, p. 6443, 1984.

[17] F. Fischer, G. Schmitz, and S. Eich, “A systematic study of grain boundary segregation and grain boundary formation energy using a new copper–nickel embedded-atom potential”, *Acta Materialia*, vol. 176, pp. 220–231, 2019.

[18] S. Yang, W. Kim, and M. Cho, “Molecular dynamics study on the coalescence kinetics and mechanical behavior of nanoporous structure formed by thermal sintering of cu nanoparticles”, *International Journal of Engineering Science*, vol. 123, pp. 1–19, 2018.

[19] F. Wang, Z. Tang, and H. He, “Stress-dislocation interaction mechanism in low-temperature thermo-compression sintering of ag nps”, *AIP Advances*, vol. 8, no. 4, p. 045 012, 2018.

[20] M. Samantaray, S. Sahoo, and D. Thatoi, “Computational modeling of heat transfer and sintering behavior during direct metal laser sintering of alsi10mg alloy powder”, *Comptes Rendus Mécanique*, vol. 346, no. 11, pp. 1043–1054, 2018.

[21] A. Stukowski, “Structure identification methods for atomistic simulations of crystalline materials”, *Modelling and Simulation in Materials Science and Engineering*, vol. 20, no. 4, p. 045 021, 2012.

[22] A. Stukowski, V. V. Bulatov, and A. Arsenlis, “Automated identification and indexing of dislocations in crystal interfaces”, *Modelling and Simulation in Materials Science and Engineering*, vol. 20, no. 8, p. 085 007, 2012.

[23] Y.-R. Huang, P.-H. Chuang, and C.-L. Chen, “Molecular-dynamics calculation of the thermal conduction in phase change materials of graphene paraffin nanocomposites”, *International Journal of Heat and Mass Transfer*, vol. 91, pp. 45–51, 2015.

[24] H. Mehrer, *Diffusion in solids: fundamentals, methods, materials, diffusion-controlled processes*. Springer Science & Business Media, 2007, vol. 155.

[25] B. Cheng and A. H. Ngan, “The crystal structures of sintered copper nanoparticles: A molecular dynamics study”, *International Journal of Plasticity*, vol. 47, pp. 65–79, 2013.

[26] A. Lange, A. Samanta, H. Majidi, *et al.*, “Dislocation mediated alignment during metal nanoparticle coalescence”, *Acta Materialia*, vol. 120, pp. 364–378, 2016.

[27] D. Nelli, G. Rossi, Z. Wang, R. E. Palmer, and R. Ferrando, “Structure and orientation effects in the coalescence of au clusters”, *Nanoscale*, vol. 12, no. 14, pp. 7688–7699, 2020.

[28] J. Wang, S. Shin, and A. Hu, “Geometrical effects on sintering dynamics of cu–ag core–shell nanoparticles”, *The Journal of Physical Chemistry C*, vol. 120, no. 31, pp. 17 791–17 800, 2016.

[29] P. Song and D. Wen, “Molecular dynamics simulation of the sintering of metallic nanoparticles”, *Journal of Nanoparticle Research*, vol. 12, no. 3, pp. 823–829, 2010.

3

DIE-ATTACH PERFORMANCE EVALUATION AND MECHANISMS STUDY OF CU SINTERING TECHNOLOGY

Robust bonding for Ag-coated copper plate and DBC substrate was achieved by using Cu quasi-nanoparticle (QNPs) sintering. The effects of temperature, pressure and time on the bonding strength and microstructural evolution of the sintering joints were intensively studied. It was found that pressure and temperature had the greatest impact on shear strength. When 5 MPa (at 250° C for 3 min) of assisted pressure, or 210° C (with 20 MPa for 3 min) of sintering temperature were applied, it only achieved around 35 MPa of shear strength. By increasing the pressure to 30 MPa or enhancing the temperature to 270° C, the strength was extremely improved to over 110 MPa. By examing the fracture surface and cross-section morphology of the sheared-off samples, it was found that the low bonding performance was due to both the inhibition effect of the organics and the incomplete sintering of Cu QNPs. In addition, strong bonding was due to the positive effect of pressure and temperature on the necking growth, sintering networking formation, pores isolation and brittle-ductile fracture transformation. Finally, the laser flash measurements and four-probe tests were carried out for evaluating the thermal and electrical properties of Cu sintered layer. It was found that although the pressure and temperature affected both values a lot, the sintering time could also improve the conductivity properties from 5.82 W/m·K to 231.15 W/m·K and 0.003 $(\mu\Omega\cdot cm)^{-1}$ *to 0.255* $(\mu\Omega\cdot cm)^{-1}$*. Accordingly, the recommended sintering profile is 250° C, 3 min, 20 MPa.*

Parts of this chapter have been published in Journal of Materials Research and Technology **19**, 1407 (2022).

3.1. INTRODUCTION

RECENTLY, copper sintering technique is receiving great attentions for the WBG semiconductor packaging applications, due to its much lower material cost (about 1~10% of the Ag price), lower ion migration tendency, as well as the high thermal conductivity (398 W/mK for bulk material)[1]–[5]. In past few years, thanks to the development of pressure-assisted sintering machine (or so-called sintering press), it is possible to both provide precise control for the temperature, time and pressure of the sintering process, and achieve the fast sintering process (less than 5 min per batch). This greatly increases the feasibility of sintering technology to be applied in the electronics packaging industry.

The most important functions of the sintered die-attach layer are mechanical bonding, heat dissipation and signal transmission. To evaluate these performances of the sintered joints and the reliability of the packaging devices, a large number of performance tests and microstructural characterization methods have been utilized. First, the die shear test combined with fracture surface analysis and cross-section morphology observation is the most popular evaluation method applied both in the industry and academia [6]–[14]. Then, the thermal conductivity and electrical resistivity[15]–[19] can be measured by using the laser flash measurements and four-probe methods. It is believed that in order to improve such sintering performances, it is first crucial to study the effect of process parameters on the microstructural evolution and bonding mechanism. In the field of Ag sintering, there is plenty of research studied on the impact of sintering process parameters[11]–[14]. However, the related study for the copper sintering technique is rare.

In this chapter, a self-developed Cu paste was fabricated with predefined workability and sintering property. Next, the Cu die-attachment samples were prepared with different sintering process parameters. Laser flash measurements, four-probe methods, and die shear tests were performed on the sintered samples to obtain the thermal, electrical, and bonding properties of the Cu sintered technique. The effects of temperature, pressure, and time on the integrated properties and the microstructural evolution of the sintered joints were then investigated. Next, the neck formation, pore development, and fracture surface forming process of the associated sintered joints were discussed. Finally, the sintering mechanism was obtained together with the optimized sintering process parameters, which can be used in the practical application of WBG semiconductor packaging.

3.2. MATERIALS AND METHODOLOGIES

3.2.1. CU PARTICLES AND OTHER MATERIALS

IN this study, the Cu quasi-nanoparticles (QNPs) were synthesized by the physical vapor deposition (PVD) methods. In order to reduce the oxidation of the raw Cu particles, a chemical reduction treatment was performed before the paste preparation. For this purpose, carboxylic acids A (99.0%) and ethanol (99.7%) were used. To prepare the Cu paste, the vehicle, the additive, and the treated Cu particles were mixed and milled together in a blender and a three-roll miller. The vehicle was composed of terpinol (95%), ethylene glycol (99.5%), and ethanol (99.7%), which were purchased from Aladdin reagent Co., Ltd. The sintering die-attached samples were then prepared by using the paste, the Cu dummy die, and the ceramic substrate for the bonding performance test. The direct bonded copper (DBC) substrates and active metal brazing (AMB) substrates with 38 mm × 27 mm size were purchased from Ferrotec. The thickness of alumina layer was 0.38 mm and the thickness of the copper plate at front- and backside of the substrate were both 0.3 mm. A 3 mm × 3 mm × 1 mm oxide free copper (OFC) small plate with 2μm Ag metallization surface coating was used as the dummy die.

3.2.2. CU QNPS TREATMENT AND PASTE FORMULATION

FOR the Cu raw particle reduction treatment, a fraction of the reductive agent carboxylic acid A was dissolved in 500 mL of absolute ethyl alcohol by magnetic stirring to prepare the treatment solution B. Then 50 g of copper QNPs were added to solution B under continuous agitation. The treatment reaction was conducted at room temperature for 40 min till the color of solution changed to dark red (solution C). Then the solution C was centrifuged at 4000 rpm for 5 min to separate the treated copper powder as well as the solution. The powders were washed three times by using the absolute ethyl alcohol to remove unreacted reactants. The final as-treated copper powders after milling are shown in Fig.3.1a. Then the as-treated QNPs (77 wt.%) were mixed with ethylene glycol (EG), terpilenol, resin and other additives with the specific ratio at 2000 rpm for 10 min through a mechanical blender to form a paste. Finally, the as-milled paste was further homogenized by the planet agitator at 1500 rpm for 2 min to form the final status of the paste, see Fig.3.1b.

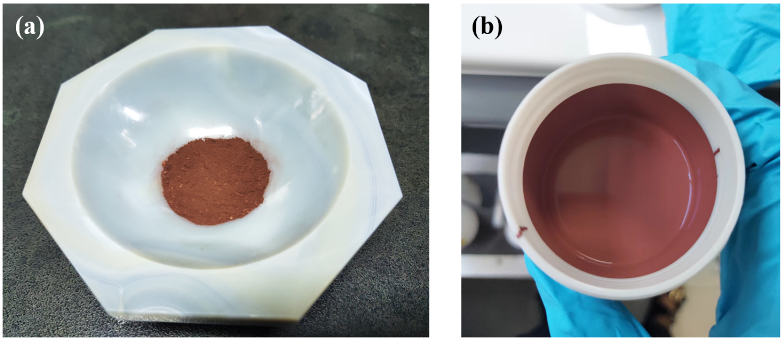

Figure 3.1: (a) The as-treated copper particles and (b) the as-prepared copper paste in a jar.

3.2.3. THE DIE-ATTACH SAMPLES AND SHEAR STRENGTH MEASUREMENT

IN this research, there was a sandwich-like die-attachment sample (dummy die/ Cu sintering layer/ substrate) being applied for shear strength test. As depicted in Fig.3.2, first the copper paste was printed onto a DBC substrate to form six 5 mm × 5 mm × 100 μm sized patterns. Next, the substrates were delivered into a vacuum oven for drying process at around 150°C for 5 min to remove the organic solvent. Then six to eight copper dummy die were placed onto the as-dried copper pad by using pick & place machine (Tresky T3002 PRO) with 0.5 MPa pressure. Finally, the pressure-assisted sintering was conducted in nitrogen atmosphere using the industrial standard sintering machine

(Boschman Sinterstar Mini). The built-in dynamic pressing tool could precisely control the sintering temperature (230~270°C), sintering time (1~4 min) and sintering pressure (5~30 MPa).

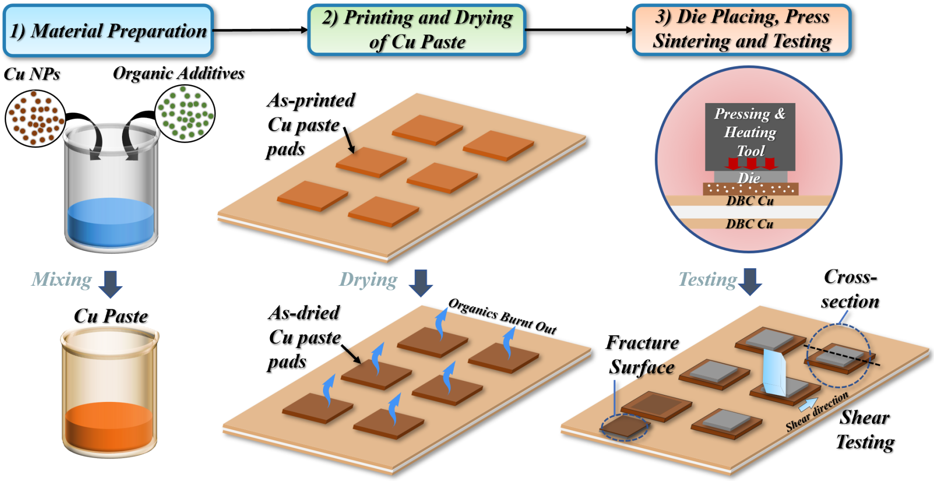
1) Material Preparation
2) Printing and Drying of Cu Paste
3) Die Placing, Press Sintering and Testing
Cu NPs
Organic Additives
As-printed Cu paste pads
Pressing & Heating Tool
Die
DBC Cu
DBC Cu
Mixing
Drying
Testing
Cu Paste
As-dried Cu paste pads
Organics Burnt Out
Cross-section
Fracture Surface
Shear direction
Shear Testing

Figure 3.2: Schematic diagrams of Cu paste preparation, pressure-assisted sintering bonding process and sample testing.

The corresponding die-attachment samples are shown in Fig.3.3. Then, to check the shear strength of the sintering joint, five bonded dummy die were sheared off by using the die shear tester (Dage 4000, Nordson) with 100μm/s shear rate. Next, the fracture surface and the cross-section morphologies were observed by using the SEM (Zeiss GeminiSEM 300). The samples for the cross-section inspection and porosity analysis were prepared by the ion-milling method (Hitachi, IM4000Plus) to guarantee the flatness of the surface. After taking the SEM image of the cross-section, the image processing software (Image J) was adopted to screen out unwanted noises and "binarize" the SEM pictures to the threshold value in the gray scale to gain the porosity values.

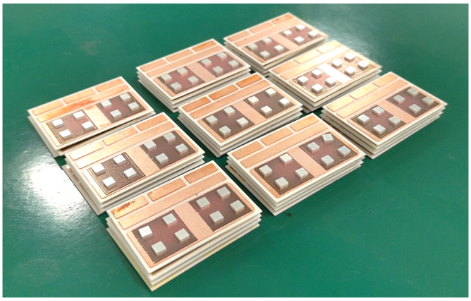

Figure 3.3: The as-sintered Cu die-attachment samples.

3.2.4. Samples for Thermal and Electrical Properties Measurement

The thermal conductivity and electrical resistivity of the die-attachment structure are too difficult to be directly measured since the sintered Cu layer is always obscured by the chip and the substrate. Therefore, according to the testing standard for the nano- and micro-metallic sintering material[20], [21], a ϕ12.8 mm disc-like Cu sintering sample was prepared by using a specially designed mold, as shown in Fig.3.4. The sample mold was divided into three separated parts: a base plate, a paste holder, and an indenter. The mold gouge and base were mounted and fixed as a mold body, and the sintered material was injected into the mold body in a certain quantity. Then the indenter was put into the hole of the gouge to compact the sintered material during the sintering process. Using the disc-like sample, the thermal conductivity of the testing specimen was measured via laser flash method, in which the thermal diffusion coefficient, the specific heat capacity and the density of the sintered parts were involved. For electrical resistivity, the Four-Point Collinear Probe Method (Kelvin Method) was utilized.

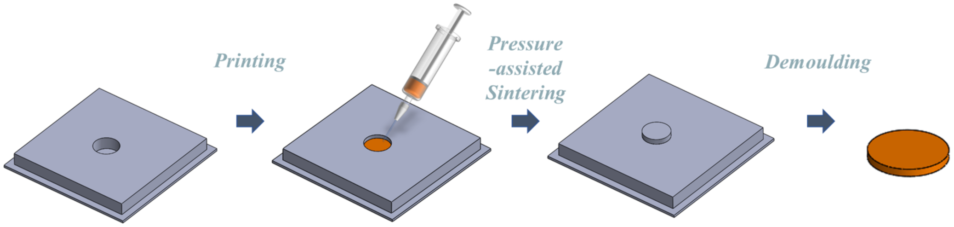

Figure 3.4: Schematic diagram of the disc-like Cu sintered sample preparation flow.

3.2.5. Thermal Conductivity Measurement Method

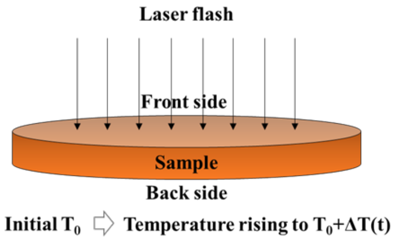

Figure 3.5: Schametic diagram of laser flash testing method.

The thermal conductivity of the sintered specimen was first measured via laser flash method. Firstly, for the thermal diffusion coefficient measurement, the standard testing equipment (NETZSCH LFA467 HyperFlash) was adopted. The sample was subjected to the high-power energy pulse (Q) in the machine, where the frontside of the specimen absorbed the pulse energy and the sample body was heated in short time. As a consequence, the temperature of backside also increased. The temperature difference of the backside between the initial and final state was recorded, as shown in Fig.3.5.

The thermal diffusion coefficient of the specimen was then calculated by using the following equation:

$$\alpha = \left(k_{1/2} \times H^2\right) / t_{1/2} \tag{3.1}$$

where H is the specimen thickness, $t_{1/2}$ is the time required for the backside temperature to reach half of the maximum value, and $k_{1/2}$ is an empirical constant corresponding to the $t_{1/2}$, which is around 0.13879.

Then the specific heat capacity of the sample was measured using a differential scanning calorimeter (DSC). The sample and a standard reference substance (a sample with a known specific heat capacity, usually α-Al_2O_3) were tested under same condition. Then, an empty pan was put into the measurement as well with the same condition. The curves for the samples under the test were subtracted from the baseline curves and then compared to the reference samples. The specific heat capacity can then be calculated via the following equations:

$$c_{p,sample} = \frac{DSC_{sample} - DSC_{base}}{DSC_{standard} - DSC_{base}} \times \frac{m_{standard}}{m_{sample}} \times c_{p,standard} \tag{3.2}$$

where DSC_{sample}, $DSC_{standard}$, DSC_{base}, are the characteristic values of DSC curves of the sample under test, the reference and the empty pan respectively. m_{sample} and $m_{standard}$ are the mass for each sample. $c_{p,standard}$ is the specific heat capacity of the standard reference.

Finally, the bulk density of the sample was measured by the Archimedes' drainage method. According to Archimedes' law, the buoyant force on a sample immersed in a liquid is equal to the weight of the liquid drained by the sample. The sample is submerged in a liquid of known density (usually water or ethanol) and measure its mass in the liquid (B). Combined with its mass in the air (A), the density can be calculated by using the specific equation as follows:

$$\rho = \frac{A}{A-B}(\rho_0 - \rho_{air}) + \rho_{air} \tag{3.3}$$

where ρ is the density to be tested. A and B are the mass of sample in the liquid and in the air. ρ_0 and ρ_{air} are the density of the liquid and the air (0.0012 g/cm^3). Therefore, the thermal conductivity of the sample is finally calculated by using the following equation:

$$\lambda = \alpha \times c_p \times \rho \tag{3.4}$$

3.2.6. ELECTRICAL RESISTIVITY MEASUREMENT METHOD

THE resistivity values of metallic materials are usually very small. Therefore, the lead resistance and the contact resistance (about 10^{-2} to 10^{-4} Ω) are non-negligible, when using a single bridge for the resistivity testing, as shown in Fig.3.6a. This may lead to very large errors in the measurement results. To eliminate this error, the Four-Point Collinear Probe Method (Kelvin Method) can be utilized. This method involves the setting of four equally spaced probes in contact with a material of unknown resistance, as shown in Fig.3.6b.

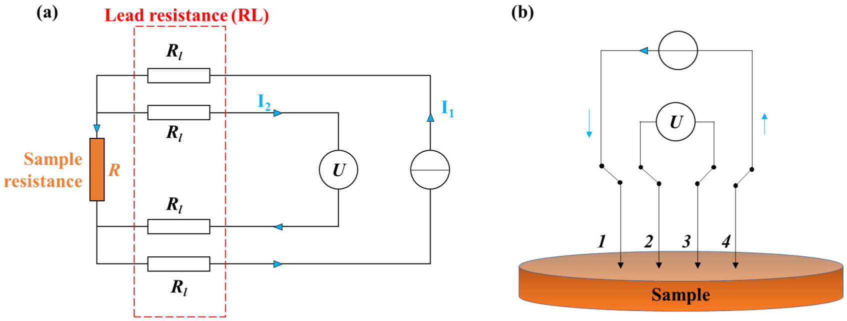

Figure 3.6: Schametic diagram of (a) the lead resistance caused by normal connection method and (b) the circuit for 4-point-probe testing method.

During the measurement, a DC current is forced between the outer two probes (1, 4), and a voltmeter measures the voltage difference between the inner two probes (2, 3). Then, the electrical resistivity can be calculated from geometric factors, the source current, and the voltage measurement in the circuit. The reason that Kelvin method works, is that the measurement loop is a voltmeter with high impedance, and thus the loop current I_{23} is almost 0. There is essentially no shunt in the excitation source current loop. As long as the current source and voltmeter are accurate enough, the calculated resistance values can be trusted:

$$R = \frac{V_{23}}{I_{14}} \times F_{(D/S)} \times F_{(W/S)} \times W \times F_{sp} \tag{3.5}$$

where D, S and W are the sample diameter, probe spacing and sample thickness. $F_{(D/S)}$ and $F_{(W/S)}$ are the sample diameter correction factor and sample thickness correction factor. When D is considered to be infinite compared to the probe spacing, and $W/S < 0.4$, $F_{(D/S)} = 4.532$, $F_{(W/S)} = 1$. Therefore, the equation can be simplified as following:

$$R = 4.532 \times \frac{V}{I} \times W \times F_{sp} \tag{3.6}$$

3.3. CHARACTERIZATION OF CU QNPS AND CU PASTE

3.3.1. SEM, TEM AND XRD CHARACTERIZATION OF THE CU QNPS

THE morphology of Cu QNPs was observed by a field-emission scanning electron microscope (SEM, Zeiss GeminiSEM 300) and transmission electron microscopy (TEM, FEI Tecnai G2 F30). Then, the size distribution of Cu QNPs was measured and calculated by further analyzing the SEM photos. The X-ray diffraction (XRD) patterns were obtained by using an X-ray diffractometer (Rigaku Smartlab) with monochromated Cu $K\alpha$ radiation (Λ = 1.54 Å). Thermogravimetric analysis (TGA) was conducted by using simultaneous thermogravimetry – differential scanning calorimetry (STA 449 F1 Jupiter) from room temperature (25°C) to 600°C with a ramping rate of 10°C/min, under N_2 atmospheres. Fourier transform infrared spectroscopy (FT-IR, Thermofisher, Nicolet IS10) was used to investigate the interactions between different function groups and Cu QNPs.

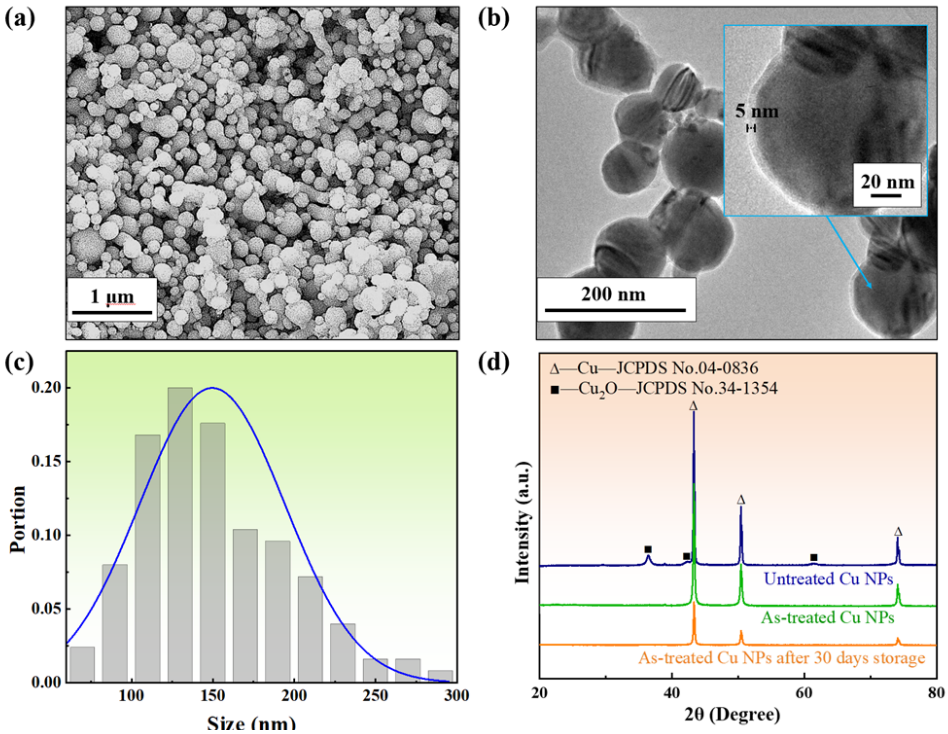

Figure 3.7: (a) SEM photo of Cu QNPs in this study. (b) TEM results of as treated Cu QNPs and the inset is the magnified TEM photo for a Cu QNP marked by a blue arrow. (c) Size distribution of treated Cu QNPs. (d) XRD patterns for original Cu QNPs and as-treated Cu QNPs.

Fig.3.7a and b show the SEM morphology and TEM photos of the treated copper particles. From Fig.3.7a, it can be observed that Cu QNPs were quasi-spherical and were uniformly mixed. Fig.3.7b shows that after treatment, there was a coating layer formed with nanometers thickness. Fig.3.7c reveals that the size of the majority of the as-treated Cu was around 130~150 nm. Some of the particles had an agglomerative effect with neighboring particles, which is due to the high activity of Cu QNPs. Fig.3.7d shows the XRD patterns for the original Cu QNPs, the Cu QNPs after oxidation removal treatment and the Cu QNPs stored for 30 days after the treatment respectively. The as-treated Cu was stored in an open beaker in the lab. The temperature of the lab was around 25°C. It can be observed that there are the main characteristic peaks at 43.29°, 50.43° and 74.13° exist for all three curves, which represent the lattice plane (111), (200) and (220) of pure Cu. Original Cu QNPs also possess diffraction peaks at 36.59°, 42.51° and 61.68°, which are corresponding to the lattice plane of (111), (200) and (220) of Cu_2O. However, for both the as-treated Cu QNPs and stored as-treated Cu QNPs, there is no longer a diffraction peak for Cu_2O, indicating that the proposed treatment method is feasible for Cu oxidation removal and storage protection.

3.3.2. FT-IR SPECTROSCOPY OF THE CU QNPS

FT-IR spectroscopy was used to investigate the interactions between different function groups and Cu particles. Fig.3.8 shows the FT-IR spectrum for the pure carboxylic acid and the as-treated Cu particles. Firstly, from the red curve, the stretching vibration of the carbon-carbon double band and the peak of enol hydroxyl can be observed at around 1630 cm^{-1} and 1322 cm^{-1}. After the treatment of Cu particle, the signals of peaks below 1630 cm^{-1} become too weak to be observed, whereas the peaks at 3450 cm^{-1} and 1630 cm^{-1} still visible. These peaks correspond to the hydroxyl and conjugated carbonyl groups, respectively. These results indicate that upon the treatment, the polyhydroxyl structures were formed on the surface of Cu particles, which may be responsible for oxidation protection for the long term.

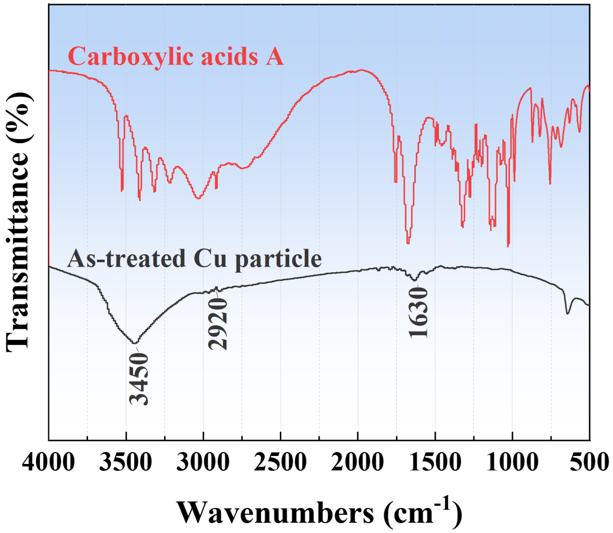

Figure 3.8: FTIR curves for pure carboxylic acid A and as treated Cu particles.

3.3.3. TG/DSC CHARACTERIZATION OF THE CU NPS

THEN, to verify the heating behavior of the treated Cu QNPs, the DSC/TG test was performed. Fig.3.9 shows the DSC/TG curves of the Cu powder before and after treatment. The heating temperature was from room temperature to 500°C, and the heating rate was 10°C/min. The whole process was performed in a nitrogen atmosphere. First of all, for the Cu raw powder (see Fig.3.9a), there is weight loss by 0.275% during at 200°C to 350°C. Since there is no DSC peak in the corresponding region, it is mainly attributed to the evaporation of water or solvent in the Cu powder. Then for the Cu QNPs after the treatment (see Fig.3.9b), there is a sharp weight loss after 200°C. Considering the sharp exothermal valley of the corresponding DSC curve, the weight loss was mainly due to the decomposition of carboxylic acid on the surface of copper particles. This heating behavior of the coating layer is beneficial for the Cu sintering process, since it can not only protect the particles from oxidation at temperatures below 200°C, but will also not affect the sintering process between particles when it is burnt out at higher temperature.

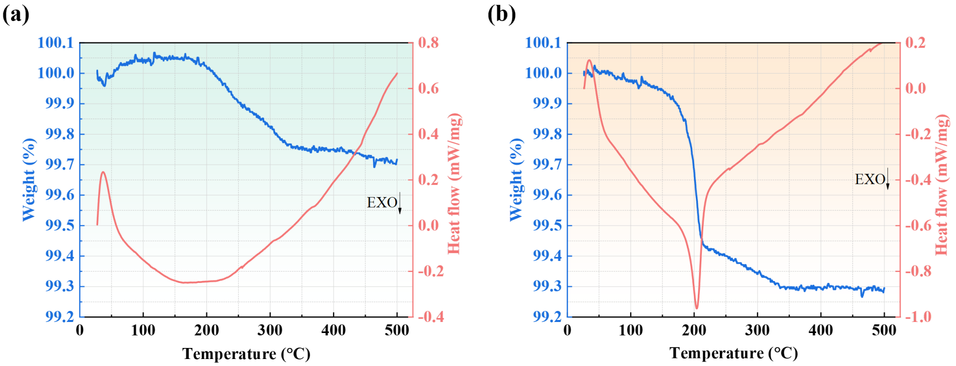

Figure 3.9: (TG/DSC curve for the Cu particles (a) before and (b) after treatment in-N_2 atmosphere.

3.3.4. TG/DSC Characterization of the Cu Paste

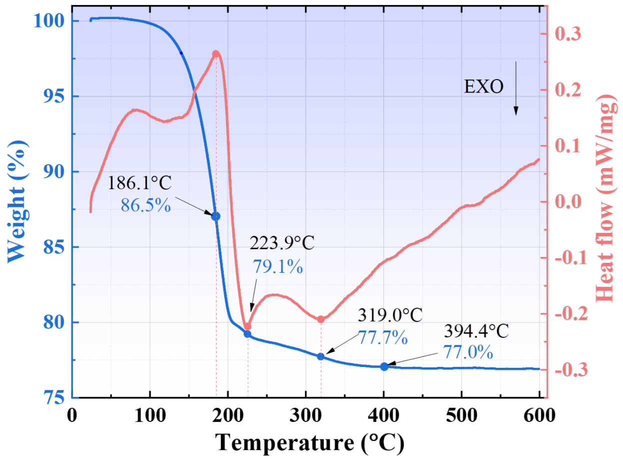

Figure 3.10: (TG/DSC curve for the Cu paste in-N_2 atmosphere.

Next, a TG/DSC test was performed to the Cu paste to determine the appropriate drying and sintering process parameters. Fig.3.10 exhibits the TG/DSC results of the copper paste used in this work. It can be noted that, the total weight difference is around 23 wt.% after the heating process, which is corresponding to the mass load of Cu metal (77 wt.%) in the paste. Moreover, the first rapid mass drop started at around 150°C and reached an endothermal peak at 186°C as a result of solvent evaporation. For this reason, the drying temperature was set as 150°C. To secure the complete removing of solvent and avoid the oxidation of copper at too high temperature, the drying time was set as 5~10 min. Then the second weight loss occurred at 200°C and reached an exothermal peak at 223.9°C due to the burnout of organic additives. Therefore, it is deduced that the sintering at temperature below 230°C might be hindered by the residual organics. The last two slow mass drop happened at around 319°C and 394°C which was attributed to the complete burnout of residual organics.

3.4. STUDY ON THE EFFECTS OF PROCESS PARAMETERS ON THE KEY PROPERTIES

THE design of experiment (DOE) in this study is shown in Table3.1. The effect of the sintering temperature (230~270°C), sintering time (1~4 min) and sintering pressure (5~30 MPa) on the thermal, electrical and mechanical properties, as well as the microstructural evolution were studied. From the perspectives of industrial manufacturing, the unit per hour (UPH) of yielding is critical. Typically, less than 5 min is required for each batch of the sintering process for electronics packaging, and therefore a dwell time range of less than 4 min was chosen in this work. The optimized process parameters will be proposed and the bonding mechanism at various conditions will also be discussed.

Table 3.1: The design of experiment for sintering process parameters study

No.	Pressure/MPa	Temperature/°C	Time/min
1	5	250	3
2	10	250	3
3	20	250	3
4	30	250	3
5	20	210	3
6	20	230	3
7	20	270	3
8	20	250	1
9	20	250	2
10	20	250	4

3.4.1. THERMAL AND ELECTRICAL PROPERTIES

THE results of thermal conductivity (red column) and the inverse of resistivity (blue column) of the samples prepared by different sintering processes are shown in Fig.3.11. First of all, it can be found that the variation trends of the thermal and electrical conductivity with respect to the sintering process parameters are similar. By increasing the sintering pressure, sintering time and sintering temperature, both thermal and electrical conductivity can be effectively enhanced. The most influential process parameters are time and temperature. With only 1 min of the sintering process, the thermal (5.82 W/m·K) and electrical (0.003/($\mu\Omega$·cm)) conductivity values of the sample are extremely small and cannot satisfy the requirements of semiconductor packaging. This is because the sintering necking formation of the copper QNPs was still incomplete at this time, and the organic coating substance was not completely removed yet. The microstructural observations on the die-attach sample prepared by same conditions will be discussed in the following sections. Increasing the sintering time to 4 minutes can effectively improve the conductivity characteristics to 231.15 W/m·K and 0.255/($\mu\Omega$·cm). There is a similar trend for the effect of temperature. By increasing the sintering temperature from 210°C to 270°C, both properties were improved from 126.53 W/m·K to 272.87 W/m·K, and from 0.124/($\mu\Omega$·cm) to 0.282/($\mu\Omega$·cm).

Among them, however, the effect of pressure is minimal. In 10 MPa condition (at 250°C for 3 min), the sample already has very high thermal (214.99W/m·K) and electrical conductivity (0.246/($\mu\Omega$·cm)), and continuing to increase the pressure has a limited effect on improving the performance of both. These results indicate that the 10 MPa of pressure, 250°C of temperature and 3 min of sintering time are already enough for promoting sintering to the second stage, at which the long-range mass transportation occurs and the key properties of the sintering body will be effectively enhanced.

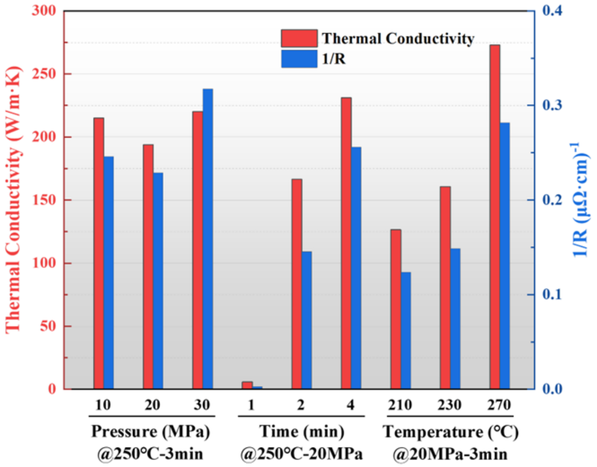

Figure 3.11: The thermal conductivity and eletrical resistivity (reverse values) for the Cu sintered samples.

3.4.2. SHEAR STRENGTH

EFFECT OF PRESSURE

FIG.3.12a, b and c show the results curve of shear strength versus different process parameters (different background colors: blue for pressure, red for temperature, green for time). From the figures, it is clear that the pressure and temperature could effectively improve shear strength, whereas the effect of time is marginal. To study the pressure effect on bonding strength first, four groups of the die-attachment samples were sintered at 250°C for 3 minutes with 5, 10, 20 and 30 MPa sintering pressure respectively. For each sample, five bonded dummy die were sheared off to calculate the average value and standard deviation. First, as sintering pressure increases from 5 MPa to 10 MPa, the mean shear strength is enhanced from 36.5 MPa to 61.2 MPa. The increasing rate for shear strength is 68%. Then by providing further higher sintering pressure (20 MPa), the shear strength reaches 100.1 MPa. The increasing rate is still high (63%). Finally, when the sintering pressure increases to 30 MPa, the shear strength increases slightly to 116.7 MPa, with only 17% increasing rate. Therefore, it indicates that raising from 5 MPa to 20 MPa has a huge effect on strength improvement, while from 20 MPa to 30 MPa, the input-output ratio is no longer sufficient. The microstructural reason for the positive effect of applied pressure on shear strength improvement will be discussed in the following sections.

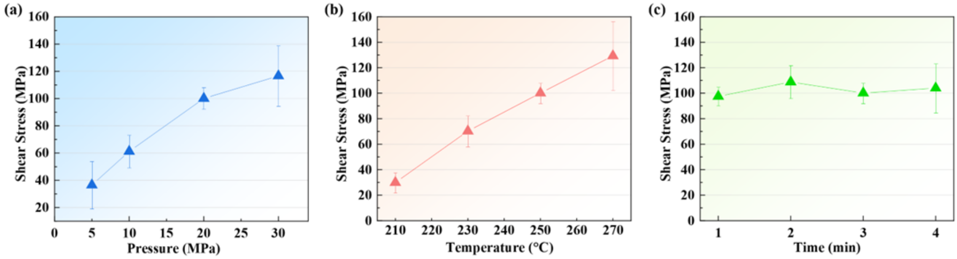

Figure 3.12: Shear stress results versus different (a) sintering pressure (5, 10, 20 and 30 MPa), (b) sintering temperature (210, 230, 250 and 270°C), (c) sintering time (1, 2, 3 and 4 min) for copper sintered joint samples.

EFFECT OF TEMPERATURE

Fig.3.12b reveals the temperature effect on the shear strength of the Cu-sintered joint. It exhibits a similar trend as the effect of the pressure. The applied pressure was set as 20 MPa and the sintering time was kept at 3 min. When the sample was sintered at 210°C, it shows less than 30 MPa average shear strength, which is insufficient for electronics packaging[22]. Surprisingly, when only added up 20°C sintering temperature, it provided over 70 MPa shear strength with 135% increasing rate. In addition, shear strength over 100 MPa was obtained at above 250°C sintering temperature. Combining the DSC and shear test results, it denotes that only temperature over 230°C can ensure the decomposition of the organic compounds and completion of the sintering process, which was also proved in some previous studies[23]. It is worth noting that for higher temperatures such as 270°C, the standard deviation of shear strength is also huge. One reason could be that the high temperature caused a warping of the substrate, which then affected the effective contact area and applied pressure on the different dummy dies. The other reason is that the higher temperature may increase the risk of copper oxidation during sintering, since a high oxygen element content is found in the EDS results in the next section. From the results discussed above, it is found that the shear strength exhibits a significant increase with increasing sintering temperature.

Effect of Time

Fig.3.12c displays the results of sintering time as a function of shear strength. The sintering temperature was set as 250°C and the applied pressure was 20 MPa. It can be found from the figure that the sintered joint can still achieve shear strength in excess of 100 MPa, when the proper temperature and pressure are set, even in short sintering time. There is no statistical difference among samples sintered for 1 min to 4 min. Even though a longer sintering time can secure a more complete sintering structure, the bonding strength of 100 MPa is already high enough for packaging applications, and thus, a longer time case will not be discussed in this work. This result implies that the material in this work is suitable for the fast sintering process for industrial applications. Combined with the effect of process parameters on the thermal and electrical properties discussed in the last two subsections, the conditions of 250°C, 3 min, and 20 MPa can be concluded as the optimal combination here. Table3.2 shows the typically reported die shear strength of both Ag sintered joints [24] and Cu sintered joints[6], [25], [26]. It is found that the bonding performance obtained in the present study is higher than the state-of-art materials. In addition, Cu QNPs also have advantages such as higher production efficiency and lower cost compared to silver and copper nanoparticles.

Table 3.2: Typical die shear stress in the related studies.

Material	Sintering temperature	Sintering pressure	Sintering time	Shear strength	Reference
Commercial sinter Ag	250°C	30 MPa	3 min	73.4 MPa	H. Zhang et al.[24]
Cu	275°C	2 MPa	10 min	35.1 MPa	Y. Mou et al.[25]
Cu	225°C	20 MPa	5 min	63 MPa	W. Choi et al.[6]
Cu	280°C	9 MPa	5 min	80 MPa	J. Jo et al.[26]
Cu	250°C	20 MPa	3 min	100.1 MPa	This work

3.5. Effects of Process Parameters on the Evolution of Microstructure

3.5.1. Fracture Mode

Effect of Pressure

In order to determine the effect of sintering process parameters on the fracture mode, the fracture surface morphology was observed and analyzed by SEM for the sheared samples. First, the global view of the sheared samples is shown in Fig.3.13a to d, for the samples sintered with different sintering pressures. It is identified that each sample contains both a smooth, low-contrast region and a rougher, high-contrast region. EDS results for position A and B in Fig.3.13b verified that high-contrast region is mainly the residual Cu (94.81 wt%) sintered layer, and the low-contrast region is mainly the exposed Ag (99.31 wt.%) metallization layer on the dummy die individually.

Fig.3.13e to h are the 2000× magnified photos of the sintered Cu residual regions as marked by blue frame in Fig.3.13a to d. It reveals a clear relationship among the microstructural evolution, the fracture surface morphology and the sintering pressure. In Fig.3.13e, it contains relatively flat broken facets on certain QNPs along the fracture direction, as marked by red arrows. Such a fracture morphology represents a brittle fracture process, which corresponds to the low strength discussed in the previous section.

Neck growth between adjacent Cu QNPs can be clearly observed as marked by green arrows. Apparently, the sintering is incomplete since the necking width is short and all QNPs still remain in spheroidal shape. Besides the neck structure, large-sized connected pores also exist in between. In this case, the primary adhesion forces in the joint were van der Waals forces from particle adsorption[27]. These structures can be the reason for the relatively low shear strength of this sample. By contrast, in the 10 MPa sample (see Fig.3.13f) there is an enlarged length of the necking size and an increased number of necking regions for each QNP compared with that of the 5 MPa sample. Apart from that, some plastic deformation positions exist in the fracture facets as marked by red arrows in Fig.3.13f of the 10 MPa sample. Based on the above-mentioned observations, it is deduced that the 5 MPa and 10 MPa sintered samples have the mixed (more adhesive) fracture mode as shown in Fig.3.14. These results suggest that the process pressure can significantly change the microstructure of the sintered layer and thus improving the bonding strength.

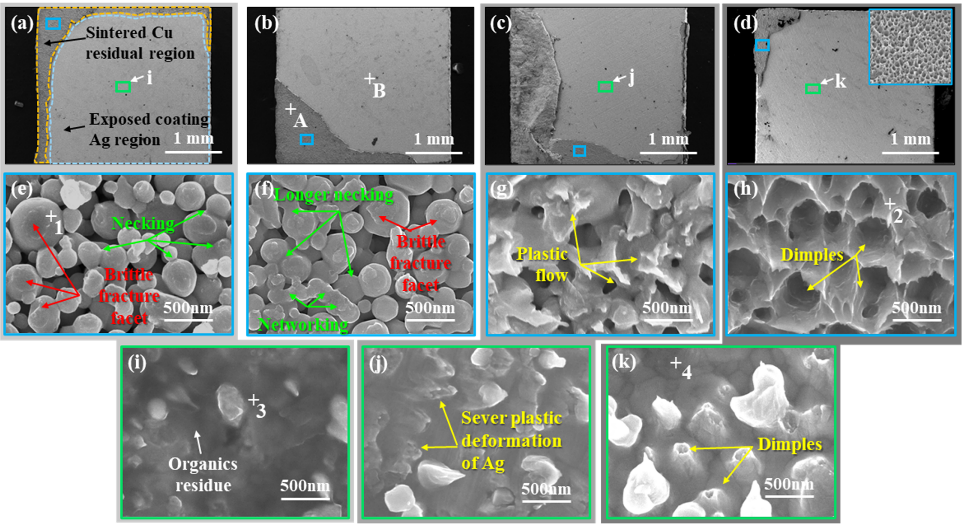
(a)
Sintered Cu residual region
i
Exposed coating Ag region
1 mm
(b)
B
A
1 mm
(c)
j
1 mm
(d)
k
1 mm
(e)
1
Necking
Brittle fracture facet
500nm
(f)
Longer necking
Brittle fracture facet
Networking
500nm
(g)
Plastic flow
500nm
(h)
2
Dimples
500nm
(i)
3
Organics residue
500nm
(j)
Sever plastic deformation of Ag
500nm
(k)
4
Dimples
500nm

Figure 3.13: SEM fracture morphology of sheared-off dice and partial magnified images for blue and green frame regions. This group of samples were sintered at 250°C for 3 min with different pressure: (a) (e) and (i) 5 MPa; (b) and (f) 10 MPa; (c), (g) and (j) 20 MPa, (d), (h) and (k) 30 MPa.

In addition, Fig.3.13g and h present the fracture surface morphologies of the 20 MPa and 30 MPa samples. Cu QNPs have already formed a large area of network with wide necking size. Also, the pores in between became smaller and were isolated by the Cu network, which indicates that the sintering process for 20 MPa and 30 MPa samples is at a near-complete stage. Moreover, it also shows that the 20 MPa and 30 MPa samples have severe plastic deformation in the fracture regions. The residual sintered Cu layer of the 30 MPa sample left on the dummy dice exhibited the severest plastic deformation and contained a uniform distribution of dimple structure as yellow arrows marked. These results corresponded to the excellent mechanical strength for them, and meanwhile representing the mixed (more cohesive) fracture mode as shown in Fig.3.14b. Among these samples, the crack first initiated from one side (bottom surface of dummy dice or top surface of DBC), and then propagate into the copper joint layer. At a certain point, the crack finally transferred to the opposite side.

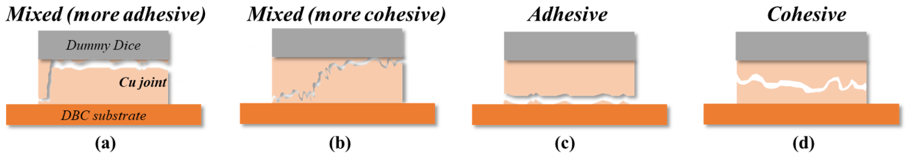

Figure 3.14: Schematic diagrams of shear test fracture mode. (a) mixed mode with more adhesive portion, (b) mixed mode with more cohesive portion, (c) pure adhesive mode, (d) pure cohesive mode.

Moreover, Fig.3.13i, j and k are the 2000× magnified photo of the exposed coating Ag region marked by green frame in Fig.3.13a, c and d. Fig.3.13i presents that there were small isolated particles embedded in the translucent background substance. EDS result (as shown in Fig.3.15a) at positions #1 and #3 shows that the particles were mainly Cu QNPs, and the translucent substance was mainly carbon residues tiled on the coating Ag layer. Based on the DSC/TG result in Fig.3.10, besides solvent, the organic additives and coating agent material on Cu QNPs would start to be burnt out at a temperature above 223.9°C. Therefore, during the sintering process of this group (at 250°C, for 3 min with different pressure), the evaporation of the organics was already initiated. Normally, with the help of pressure, the gas would be expelled quickly[28]. However, for low pressure (5 MPa, Fig.3.13e and i) scenario, the outgassing process is slow and incomplete within 3 min. Therefore, large amounts of evaporated organics did not have time to expel and were gathered and locked inside the sintered layer. In contrast, for the higher pressure scenario in Fig.3.15a (points #2 and #4), the carbon content was dramatically reduced, and with the increase of sintering pressure, there were more and more Ag and Cu elements left on copper sintered layer region and on exposed metallization layer region respectively. The above-mentioned results indicate that higher pressure may promote atomic diffusion during the sintering process, and at the same time, effectively enhance bonding strength by promoting necking growth, networking formation, pores isolation and brittle-ductile fracture transformation.

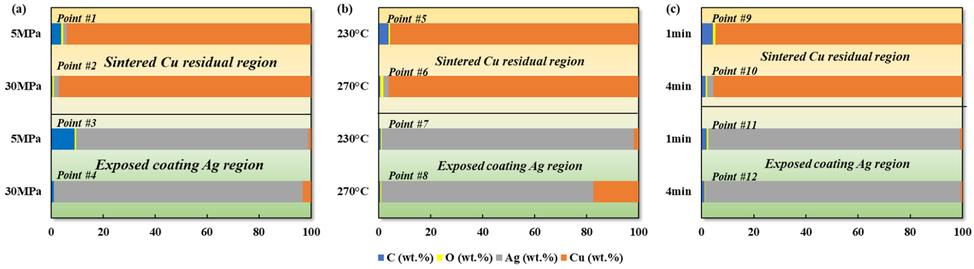

Figure 3.15: EDS results for the marked positions in the SEM fracture morphology figures. (a) points in Fig.14; (b) points in Fig.17; (c) points in Fig.18.

EFFECT OF TEMPERATURE

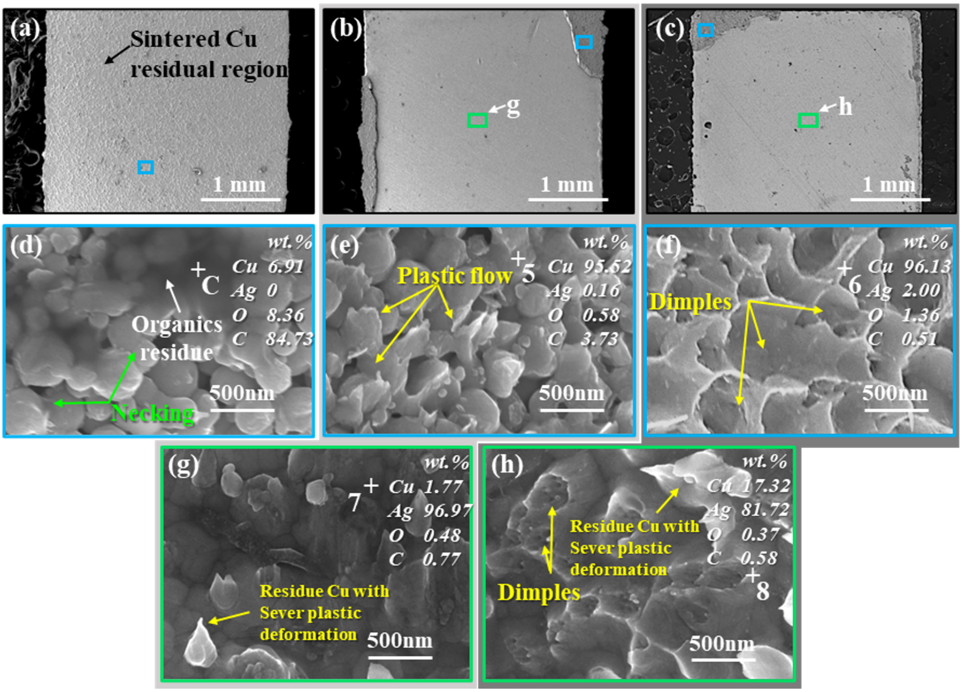
(a)
Sintered Cu
residual region
1 mm
(b)
g
1 mm
(c)
h
1 mm
(d)
wt.%
Cu 6.91
Ag 0
O 8.36
C 84.73
C
Organics
residue
Necking
500nm
(e)
wt.%
Plastic flow
5
Cu 95.52
Ag 0.16
O 0.58
C 3.73
500nm
(f)
wt.%
Dimples
6
Cu 96.13
Ag 2.00
O 1.36
C 0.51
500nm
(g)
wt.%
7
Cu 1.77
Ag 96.97
O 0.48
C 0.77
Residue Cu with
Sever plastic
deformation
500nm
(h)
wt.%
Cu 17.32
Ag 81.72
O 0.37
C 0.58
Residue Cu with
Sever plastic
deformation
Dimples
8
500nm

Figure 3.16: SEM fracture morphology of sheared-off dice and partial magnified images for blue and green frame regions. This group of samples were sintered with 20 MPa for 3 min at different temperatures: (a) and (d) 210°C; (b) (e) and (g) 230°C; (c), (f) and (h) 270°C.

THE fracture morphology SEM photos of the samples sintered at 210°C to 270°C are shown in Fig.3.16. Combined with the discussion in the previous part it is proved that the exposed layer in Fig.3.16a of the 210°C sample is sintered Cu. Unlike other samples, the fracture area for 210°C sintered sample is mainly on the interface between the substrate and sintered layer. Thus, it is clear that the sample sintered at 210°C contains adhesive fracture mode as shown in Fig.3.15c. It suggests that the Cu sintered layer did not form strong bonding with DBC substrate yet. Fig.3.16d shows the magnified image of the blue frame area in Fig.3.16a. Although some particles were found to be slightly deformed, most of Cu QNPs kept their sphere-like shape and yielded short necking structure (marked with green arrows) with its adjacent particles. This again represents that such sintering was at an incomplete stage at such low temperatures. Additionally, huge pores distributed randomly around particles and therefore created a relatively loose structure. A large amount of dark translucent substance was also found in this region. The EDS result at position C proves that it is organics residues laying around sintered Cu, containing a large amount of carbon and oxygen. This can be attributed to that sintering temperature was lower than the organics evaporating temperature. In addition, it can be found that the surface of organic residue is smooth, and thus, there was neither physical nor chemical bonding between the organic gathering residue and the substrate surface. Since on the interface some regions were occupied by such substance, it reduced the region for bonding between Cu sintered layer and substrate surface. Consequently, it further reduced the bonding strength of this sample.

Fig.3.16b, c, e and f present that some of the sintered layer were left on the substrate, while small amount remained on the dummy die for the samples sintered at 230°C as well as 270°C. The magnified view of the fracture surface of 230°C sample in Fig.3.16e shows relatively denser microstructure with the obvious mono-directional plastic flow as marked by yellow arrows. Hence, before the fracture, moderate plastic deformation occurred in these areas. Similarly, the magnified view of 270°C sheared sample shows sintered Cu structure with large deformation and uniformly distributed dimple structures on both the residual copper sintered layer in Fig.3.16f, and the exposed Ag metallization layer in Fig.3.16h. Such deep dimples indicate even more severe plastic deformation during the shear test[13]. It suggests that the fracture occurred on the interface but propagated into the sintered layer, and thus belongs to the mixed mode (with a more cohesive portion). Furthermore, the EDS results in Fig.3.15c for position #5 to #8 reveal that higher temperature effectively increased the Cu and Ag interdiffusion, and at the same time helped to remove organic residues more completely.

Effect of Time

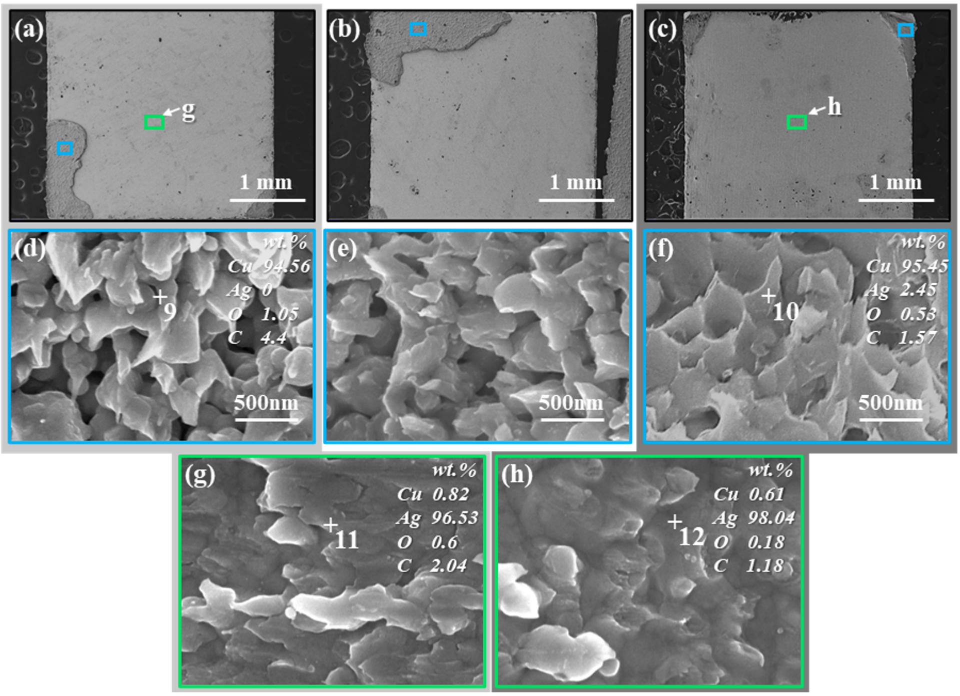

Figure 3.17: SEM fracture morphology of sheared-off dice and partial magnified images for blue and green frame regions. This group of samples were sintered at 250°C with 20 MPa for different dwell time: (a) (d) and (g) 1 min; (b) and (e) 2 min; (c), (f) and (h) 4 min.

In Fig.3.17, it shows the fracture morphology SEM photos of the sample sintered for 1, 2 and 4 min. We found that the fracture modes for this sample group all belong to mixed mode (more cohesive portion). In such fracture mode, a crack initiated from one interface and propagated into the sintering layer and then fast transferred onto the other interface on the opposite side. Similarly, EDS results in Fig.3.15c of position #9 to #12 prove that few of the sintering material was taken away by the dummy die but most of the Cu sintered material remained on the substrate. Fig.3.17d to f are the magnified view of the position marked by blue frame in Fig.3.17a to c. From these figures, all the sintering material has huge necking formed and no spheroidal-shape QNPs existed anymore. Distinct plastic flow can be found in all samples and obvious dimple microstructure existed in the 4 min sintering one, which is corresponding to the high shear strength for all samples. By further comparing the EDS results for samples sintered for different dwell time, it is found that the Cu content and Ag content are almost unchanged on the copper sintered residue layer and the exposed silver metallization layer on the dummy die. Therefore, it is deduced that within 1 min to 4 min, there is little difference in the atomic diffusion process in the Cu-sintered body and bonding interface.

3.5.2. INTERFACE EVOLUTION

EFFECT OF PRESSURE

NEXT, the inspection of the cross-section microstructure was conducted for each sintered joint in order to study the densification effect and interface diffusion of the sintered layer. Fig.3.18a to d and Fig.3.18e to h display morphologies near the bonding interface between the sintered layer and the Ag metallization layer of the dummy die as well as the morphologies near the bonding interface between the sintered layer and the substrate, respectively.

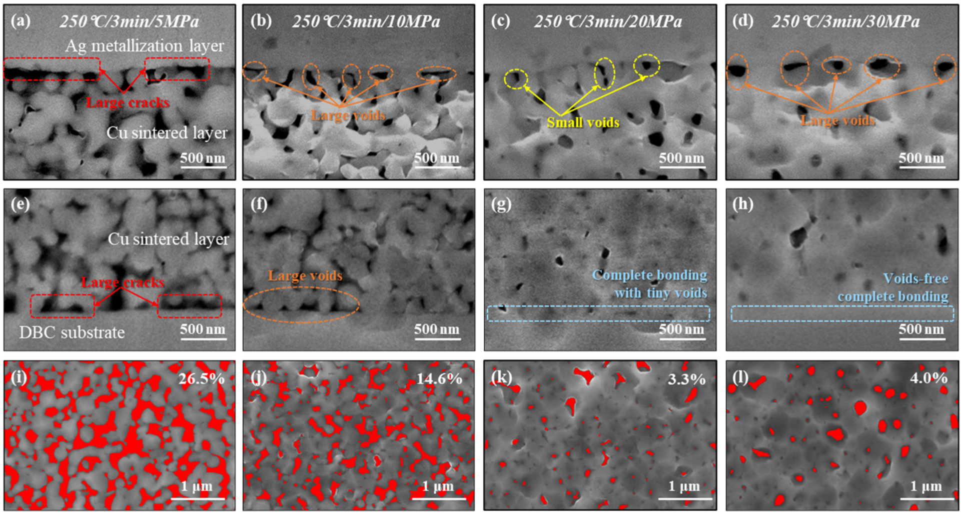
(a) 250 ℃/3min/5MPa
Ag metallization layer
Large cracks
Cu sintered layer
500 nm
(b) 250 ℃/3min/10MPa
Large voids
500 nm
(c) 250 ℃/3min/20MPa
Small voids
500 nm
(d) 250 ℃/3min/30MPa
Large voids
500 nm
(e)
Cu sintered layer
Large cracks
DBC substrate
500 nm
(f)
Large voids
500 nm
(g)
Complete bonding
with tiny voids
500 nm
(h)
Voids-free
complete bonding
500 nm
(i) 26.5%
1 μm
(j) 14.6%
1 μm
(k) 3.3%
1 μm
(l) 4.0%
1 μm

Figure 3.18: SEM images of cross-section morphology with different sintering pressure: (a) – (d) near the Cu-Ag bonding interface; (e) – (h) near the Cu-Cu bonding interface; (i) – (l) sintered body.

It can be seen that the sintering pressure has a remarkable impact on the morphology of both the Cu sintered layer and the bonding interface. As discussed in the previous section, for the 5 MPa sample, the sintering was not done thoroughly, causing short neck growth between Cu QNPs. In addition, the removal of organics was incomplete. Lots of transparent substance which was proved to be the organic residue was found on each interface as shown in Fig.3.18a and e, hindering the contact between Cu sintered layer and the surface to be attached. Plenty of large-size voids connected with each other and formed large-size cracks as marked by red dotted boxes. Then With the increase of sintering pressure (10 MPa, 20 MPa and 30 MPa), the size of the neck and network of the sintered body increased. Also, the organics residue is hard to be found on the interface anymore. More Cu QNPs were able to be connected with the upper and lower surface.

On the Cu-Cu lower interfaces, as shown in Fig.3.18e to h, the number and size of the interfacial voids always decreased with the increase of sintered pressure. For 20 MPa and 30 MPa sample, the voids on the Cu-Cu interface were even diminished forming a voids-free complete bonding region. This is believed as one of the most important reasons for bonding strength improvement and fracture mode transition found in the previous section. However, even though the number and size of interface voids on the Ag-Cu interface decreased dramatically first with the pressure increased from 5 MPa to 20 MPa, they increased when the sintering pressure was 30 MPa. This is mainly attributed to the unequal Ag to Cu and Cu to Ag interdiffusion speed at this region. More Ag atoms were transported into Cu and left the so-called Kirkendall voids[13], [29], which may result in a reduction of the effective connection area. This is also the reason why large area of the Cu sintered layer was always left on the substrate surface in most cases in this study.

Fig.3.18i to l are the magnified photos of the sintered body. Necking and networking morphologies can be clearly observed. Previous research[30]–[32] found that intrinsic pores existed in the sintering joints and affected the bulk mechanical properties such as elastic modulus, yield strength, ultimate tensile strength, and thus, it is important to analyze the porosity characteristics of the sintered structure. By applying the Image-J analysis introduced in the previous section, the porosity value for each sample can be extracted. With low sintering pressure (5 MPa) it shows large-sized pores with the highest porosity (26.5%). Via increasing sintering pressure to 10 MPa and 20 MPa, the porosity decreased dramatically to 14.6%and 3.3%. Higher pressure can provide more energy for NPs coalescence, which can promote the sintering process. However, by further increasing bonding pressure to 30 MPa, the porosity reversely increased to 4.0%. The reason for the porosity reincrease is the shrinkage of the sintered body at the final sintering stage[33].

EFFECT OF TEMPERATURE

To further study the cooperative effect of pressure and temperature on the microstructure, the SEM cross-section figures for samples sintered at 210°C with 10 MPa and 20 MPa, and at 270°C with 10 MPa and 20 MPa were analyzed and compared. For the low temperature with low pressure scenario (at 210°C with 10 MPa) as shown in Fig.3.19a, e and i, Cu QNPs were only pushed to contact with each other and slightly sintered to form short necks. Due to the incomplete burnt-out of organic additives at such low temperatures, lots of residues were left inside the sintering body and on the bonding interface. Similar to the low-pressure case in the previous discussion, large cracks were formed on the interface and therefore causing the delamination after sintering. By increasing pressure to 20 MPa (still at 210°C), the QNPs were pushed together closer, and the neck length grew effectively as depicted in Fig.3.19b, f and j. The porosity reduced from 32.7%to 8.54%, and the most of pores were already isolated. The rest pores only have less than 0.5 μm diameter distributed in the sintered network. On both the upper and lower interface (see Fig.3.19b and f), the sintering necks between the surface of the substrate and the QNPs were formed. Since the neck size was still small and the sintering networking was weak, the bonding strength for this sample was only around 30 MPa.

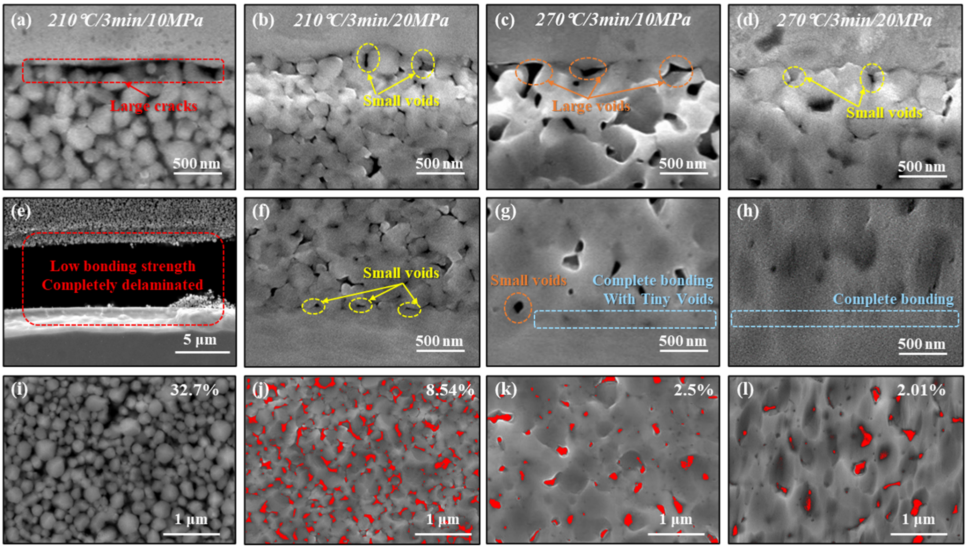
(a) 210℃/3min/10MPa
Large cracks
500 nm
(b) 210℃/3min/20MPa
Small voids
500 nm
(c) 270℃/3min/10MPa
Large voids
500 nm
(d) 270℃/3min/20MPa
Small voids
500 nm
(e)
Low bonding strength
Completely delaminated
5 μm
(f)
Small voids
500 nm
(g)
Small voids
Complete bonding
With Tiny Voids
500 nm
(h)
Complete bonding
500 nm
(i)
32.7%
1 μm
(j)
8.54%
1 μm
(k)
2.5%
1 μm
(l)
2.01%
1 μm

Figure 3.19: SEM images of cross-section morphology with different sintering pressure and at different sintering temperature: (a) – (d) near the Cu-Ag bonding interface; (e) – (h) near the Cu-Cu bonding interface; (i) – (l) sintered body.

At high temperatures as shown in Fig.3.19c, d and g, h, the sintering process of the Cu particles has almost progressed to the final stage, in which strong networking was formed. In Fig.3.19k and l, both the sintering body of 10 MPa and 20 MPa cases show high density compared with the low-temperature scenario. The porosity also shows a slight decrease from 8.54%to 7.83%for 210°C and 230°C and then from 3.30%to 2.01%for 250°C and 270°C. With increasing of pressure, the voids became smaller, and most voids were diminished leaving a complete bonding region on the Cu-Cu interface.

EFFECT OF TIME

NEXT, the comprehensive effect of pressure and dwell time on the microstructure was investigated. From the cross-section photo in Fig.3.20, the effect of pressure on the microstructure of different dwell time cases is clear. No matter for short-time or long-time cases, the sintering density increased effectively and the interface voids on both the Ag-Cu and Cu-Cu interface decreased dramatically with the increase of sintering pressure.

Then, with the same low pressure (10 MPa), longer sintering time (4 min, as in Fig.3.20c, g and k) could promote the interfacial diffusion process between the Cu QNPs and the substrate interface, which resulted in the formation of the isolated interfacial voids compared with the large continuous cracks in the short-time sample (1 min, as in Fig.3.20a, e and i). It has also slightly decreased the porosity from 21.4% to 18.1%. However, with the high pressure (20 MPa), although longer sintering time (4 min, as in Fig.3.20d, h and l) diminished the small voids on the Cu-Cu interface (Fig.3.20f) via facilitating the atomic diffusion of Cu atoms, it again caused the Kirkendall voids on the Ag-Cu interface.

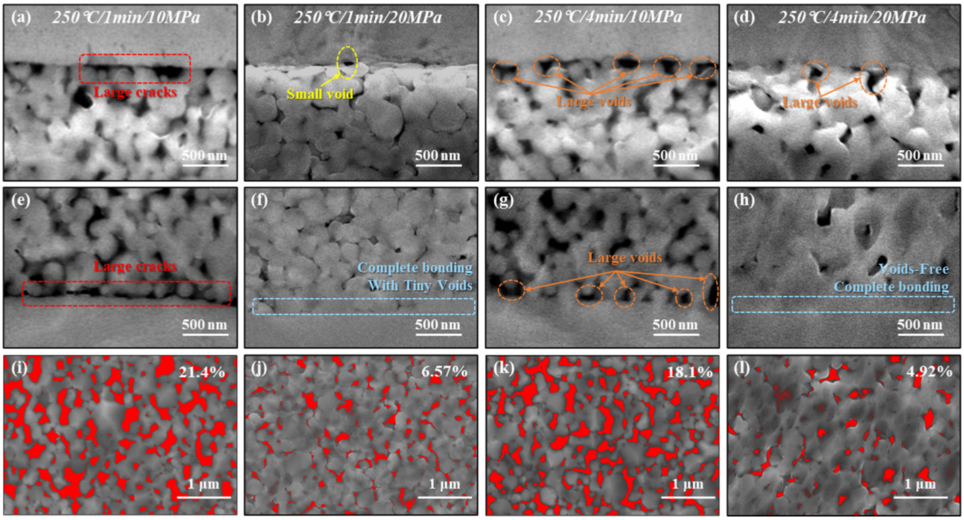
(a) 250 ℃/1min/10MPa
Large cracks
500 nm
(b) 250 ℃/1min/20MPa
Small void
500 nm
(c) 250 ℃/4min/10MPa
Large voids
500 nm
(d) 250 ℃/4min/20MPa
Large voids
500 nm
(e)
Large cracks
500 nm
(f)
Complete bonding
With Tiny Voids
500 nm
(g)
Large voids
500 nm
(h)
Voids-Free
Complete bonding
500 nm
(i)
21.4%
1 μm
(j)
6.57%
1 μm
(k)
18.1%
1 μm
(l)
4.92%
1 μm

Figure 3.20: SEM images of cross-section morphology with different sintering pressure and for different time: (a) – (d) near the Cu-Ag bonding interface; (e) – (h) near the Cu-Cu bonding interface; (i) – (l) sintered body.

Combined with thermal and electrical conductivity results in Fig.3.11, shear stress results in Fig.3.12, and the microstructural results in this section, it shows that, though the sample can already be well sintered at 250°C with 20 MPa within 1 min, longer sintering time is still necessary to ensure the formation of rigid sintering body networking and to provide sufficient thermal and electrical properties. Moreover, sintering for too long time may also cause unexpected interfacial defects, which need to be avoided by experiments in practice.

3.5.3. BONDING MECHANISM

DURING the pressure-assisted sintering, with the help of temperature, dwell time and pressure, the residue polymer content will be burnt out and degassed from the sintered body. At the same time, the copper QNPs come to contact with their adjacent particles, substrate surface, and the coating layer of the die, forming mechanical-chemical bonding that provides high bonding strength to the die and substrate.

In the low-temperature case (as the up-left case shown in Fig.3.21), the shear strength was relatively low, and the fracture surface was in adhesive mode. The EDS and DSC/TG results prove that the organics in the paste were not completely removed, but were distributed in the sintering body and tiled on the Ag-Cu interface. In addition, the necks between Cu particles were short in this case. Thus, the weak bonding at low temperatures is mainly due to the hindering effect caused by the incomplete burn-out of organic matter and the incomplete growth of the sintering neck due to the lower sintering energy supply.

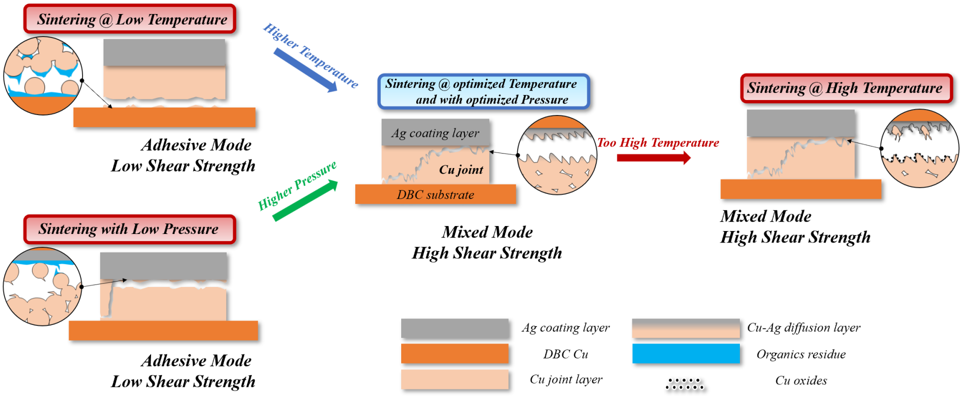
Sintering @ Low Temperature
Adhesive Mode
Low Shear Strength
Higher Temperature
Sintering @ optimized Temperature and with optimized Pressure
Ag coating layer
Cu joint
DBC substrate
Too High Temperature
Sintering @ High Temperature
Mixed Mode
High Shear Strength
Higher Pressure
Sintering with Low Pressure
Adhesive Mode
Low Shear Strength
Mixed Mode
High Shear Strength
Ag coating layer
DBC Cu
Cu joint layer
Cu-Ag diffusion layer
Organics residue
Cu oxides

Figure 3.21: Schematic diagram of sintering mechanism for different process conditions.

By increasing temperature (as the blue arrow indicates), the bonding strength and microstructure were improved. Since the higher temperature can effectively improve the atomic diffusion in the bonding process, it is found that the Cu content in both the Cu sintered joint and the Ag coating layer on the dummy die was increased, and as a result, forming the Cu-Ag metallization bonding. Meanwhile, the content of carbon decreased with the increase of sintering temperature because most of the organics were burnt out during the sintering.

When sintering at low pressure (as the second path shown in Fig.3.21), it shows both the low shear strength and the mixed fracture mode but with a more adhesive portion. Fig.3.21 also indicates that fragile bonding is due to incomplete neck growth and large amounts of pores in between. Meanwhile, although organics could be evaporated at 250°C, without high pressure it could not be expelled quickly. Thus, most of the organics again condensed on the upper surface, leaving a large area of unconnected delamination on the Ag-Cu interface as observed by SEM and EDS.

By increasing the pressure (as the green arrow indicates), although the sintering stage was still incomplete, the contact area of each particle and the density of the sintered body were enhanced. Additionally, the organics were squeezed out and thus providing more space for particle sintering. Therefore the bonding performance can be enhanced.

However, when the temperature was too high (as the red arrow indicates), there was first the oxidation issue. In the SEM fracture morphology photos we found that there were small hillocks and corresponding small pits on the dimples with a couple of nanometers in the high-temperature case. Combined with EDS results, it is found that the oxygen content was higher than in other samples. Such hillocks were also observed in some studies [34] which were believed to be copper oxides generated during material treatment or high-temperature sintering. Other studies also reported [35] that the copper oxide formed during the reliability test may enhance the bonding strength. It is deduced that although the small hillocks could improve the bonding strength by mechanical interlocking effect in this study, the microstructural evolution and negative effect during the reliability test of such structure is still unclear. Moreover, the interface between the Cu sintering layer and Ag coating layer on the chip was observed to contain more voids than that of the interface between the Cu sintering layer and DBC substrate. This is mainly due to the unequal diffusion rate of Ag to Cu and Cu to Cu. Consequently, most of the fracture surface appeared at the Ag-Cu interface side.

3.6. CONCLUSION

IN this chapter, a self-developed Cu paste was fabricated with predefined printing, drying and sintering workability. A reductive pretreatment was conducted in advance to the raw Cu particles to remove the original oxidation. Laser flash measurements, four-probe methods, and die shear tests were performed to obtain the thermal, electrical, and bonding properties of Cu-sintered die attachment techniques. The effects of temperature, pressure, and time on the integrated properties and the microstructural evolution of the sinter joints are then investigated. With only 1 min of the sintering process, the thermal (5.82 W/m·K) and electrical conductivity (0.003/($\mu\Omega$·cm)) of the sample is extremely small and cannot satisfy the semiconductor packaging requirements. Increasing the sintering time to 4 minutes can effectively improve the conductivity characteristics to 231.15 W/m·K and 0.255/($\mu\Omega$·cm). There is a similar trend for the effect of temperature. By increasing the sintering temperature from 210°C to 270°C, both properties were improved from 126.53 W/m·K to 272.87 W/m·K, and from 0.124/($\mu\Omega$·cm) to 0.282/($\mu\Omega$·cm).

Then, in order to evaluate the impact of the Cu sintering process parameters on the joining performance and microstructure evolution of the die-attach samples, the shear test was conducted with various sintering temperatures, pressure and time. It was found that sintering temperature between 210°C and 230°C, or assisted pressure less than 10 MPa could provide bonding strength of around 30 MPa. Such low strength is due to both the partially burnt-out of organics and incomplete Cu particles sintering. By increasing pressure to 20 MPa and 30 MPa, it shows the enhanced die shear strength of 100.1 MPa and 116 MPa, accomplished with a sintering temperature of 250°C for 3 min. When increasing temperature to 270°C, the shear strength was extremely enhanced to over 120 MPa. Moreover, sintering time can insignificantly affect the microstructure and bonding strength but slightly influence the formation of the interfacial defects in less than 4 min. Material microstructural characterization demonstrates that high bonding is coming from the positive effect of pressure and temperature on promoting the necking growth, sintering networking formation, pores isolation and brittle-ductile fracture transition. Considering the small improvement effect by a further increase of temperature and pressure, 250°C/3 min/20 MPa process recipe is well recommended for the application.

REFERENCES

[1] Y. Gao, C. Chen, S. Nagao, K. Suganuma, A. S. Bahman, and F. Iannuzzo, “Highly reliable package using cu particles sinter paste for next generation power devices”, in *PCIM Europe 2019; International Exhibition and Conference for Power Electronics, Intelligent Motion, Renewable Energy and Energy Management*, VDE, 2019, pp. 1–4.

[2] Y. Yuan, H. Wu, J. Li, P. Zhu, and R. Sun, “Cu-cu joint formation by low-temperature sintering of self-reducible cu nanoparticle paste under ambient condition”, *Applied Surface Science*, vol. 570, p. 151 220, 2021.

[3] B. Zhang, A. Damian, J. Zijl, *et al.*, “In-air sintering of copper nanoparticle paste with pressure-assistance for die attachment in high power electronics”, *Journal of Materials Science: Materials in Electronics*, vol. 32, no. 4, pp. 4544–4555, 2021.

[4] Y. Zhang, P. Zhu, G. Li, *et al.*, “Easy separation of cuo nanocrystals with high catalytic activity”, *Materials Letters*, vol. 212, pp. 332–335, 2018.

[5] C. Chen, A. Iwaki, A. Suetake, K. Sugiura, K. Kanie, and K. Suganuma, “Low temperature cu sinter joining on different metallization substrates and its reliability evaluation with a high current density”, in *2021 33rd International Symposium on Power Semiconductor Devices and ICs (ISPSD)*, IEEE, 2021, pp. 387–390.

[6] W. L. Choi, Y. S. Kim, K.-S. Lee, and J.-H. Lee, “Characterization of the die-attach process via low-temperature reduction of cu formate in air”, *Journal of Materials Science: Materials in Electronics*, vol. 30, no. 10, pp. 9806–9813, 2019.

[7] D. Ishikawa, B. N. An, M. Mail, *et al.*, “Bonding strength of cu sinter die-bonding paste on ni, cu, ag, and au surfaces under pressureless bonding process”, *Transactions of The Japan Institute of Electronics Packaging*, vol. 13, E19–017, 2020.

[8] Y. Gao, W. Li, C. Chen, *et al.*, “Novel copper particle paste with self-reduction and self-protection characteristics for die attachment of power semiconductor under a nitrogen atmosphere”, *Materials & Design*, vol. 160, pp. 1265–1272, 2018.

[9] J. Zhao, M. Yao, and N.-C. Lee, “Nano-cu sintering paste for high power devices die attach applications”, in *2018 IEEE 68th Electronic Components and Technology Conference (ECTC)*, IEEE, 2018, pp. 557–563.

[10] K. Siow and Y. Lin, “Identifying the development state of sintered silver (ag) as a bonding material in the microelectronic packaging via a patent landscape study”, *Journal of Electronic Packaging*, vol. 138, no. 2, 2016.

[11] Y. Liu, H. Zhang, L. Wang, X. Fan, G. Zhang, and F. Sun, “Effect of sintering pressure on the porosity and the shear strength of the pressure-assisted silver sintering bonding”, *IEEE Transactions on Device and Materials Reliability*, vol. 18, no. 2, pp. 240–246, 2018.

[12] J. Yan, G. Zou, A.-p. Wu, *et al.*, “Pressureless bonding process using ag nanoparticle paste for flexible electronics packaging”, *Scripta Materialia*, vol. 66, no. 8, pp. 582–585, 2012.

[13] F. Yang, W. Zhu, W. Wu, H. Ji, C. Hang, and M. Li, “Microstructural evolution and degradation mechanism of sic–cu chip attachment using sintered nano-ag paste during high-temperature ageing”, *Journal of Alloys and Compounds*, vol. 846, p. 156 442, 2020.

[14] S. Sakamoto and K. Suganuma, “Thermo mechanical reliability of low-temperature low-pressure die bonding using thin ag flake pastes”, in *2012 7th International Conference on Integrated Power Electronics Systems (CIPS)*, IEEE, 2012, pp. 1–2.

[15] M. Wang, Y.-H. Mei, J. Jin, S. Chen, X. Li, and G.-Q. Lu, “Pressureless sintered-silver die-attach at 180° c for power electronics packaging”, *IEEE Transactions on Power Electronics*, vol. 36, no. 11, pp. 12 141–12 145, 2021.

[16] J. Liu, H. Chen, H. Ji, and M. Li, “Highly conductive cu–cu joint formation by low-temperature sintering of formic acid-treated cu nanoparticles”, *ACS applied materials & interfaces*, vol. 8, no. 48, pp. 33 289–33 298, 2016.

[17] L. Del Carro, A. A. Zinn, P. Ruch, F. Bouville, A. R. Studart, and T. Brunschwiler, “Oxide-free copper pastes for the attachment of large-area power devices”, *Journal of Electronic Materials*, vol. 48, no. 10, pp. 6823–6834, 2019.

[18] S. Wang, H. Ji, M. Li, and C. Wang, “Fabrication of interconnects using pressureless low temperature sintered ag nanoparticles”, *Materials Letters*, vol. 85, pp. 61–63, 2012.

[19] J. Zürcher, L. Del Carro, G. Schlottig, *et al.*, “All-copper flip chip interconnects by pressureless and low temperature nanoparticle sintering”, in *2016 IEEE 66th Electronic Components and Technology Conference (ECTC)*, IEEE, 2016, pp. 343–349.

[20] CASAS, *Test method for resistivity of micro and nano metal sintered compact: Four probe method (t/casas 019-2021)*, Retrieved from `http://casa-china.cn/a/research/standard/`, 2021.

[21] CASAS, *Test method for thermal conductivity of micro-nano sintered compact: Laser flash method (t/casas 020-2021)*, Retrieved from `http://casa-china.cn/a/research/standard/`, 2021.

[22] T. F. Chen and K. S. Siow, “Comparing the mechanical and thermal-electrical properties of sintered copper (cu) and sintered silver (ag) joints”, *Journal of alloys and Compounds*, vol. 866, p. 158 783, 2021.

[23] X. Liu, Q. Zhou, X. Zhao, S. W. Koh, H. Ye, and G. Zhang, “Study and application of nano copper sintering technology in power electronics packaging”, in *2021 IEEE 71st Electronic Components and Technology Conference (ECTC)*, IEEE, 2021, pp. 1928–1932.

[24] H. Zhang, Y. Liu, L. Wang, *et al.*, “Effects of sintering pressure on the densification and mechanical properties of nanosilver double-side sintered power module”, *IEEE Transactions on Components, Packaging and Manufacturing Technology*, vol. 9, no. 5, pp. 963–972, 2018.

[25] Y. Mou, H. Cheng, Y. Peng, and M. Chen, “Fabrication of reliable cu-cu joints by low temperature bonding isopropanol stabilized cu nanoparticles in air”, *Materials Letters*, vol. 229, pp. 353–356, 2018.

[26] J.-L. Jo, K. Anai, S. Yamauchi, T. Hattori, and T. Sakaue, “The bonding properties of various surface finishes with cu paste for pressure sintering”, in *2020 IEEE 70th Electronic Components and Technology Conference (ECTC)*, IEEE, 2020, pp. 749–754.

[27] J. Li, X. Li, L. Wang, Y.-H. Mei, and G.-Q. Lu, “A novel multiscale silver paste for die bonding on bare copper by low-temperature pressure-free sintering in air”, *Materials & Design*, vol. 140, pp. 64–72, 2018.

[28] S. Chen, G. Fan, X. Yan, C. LaBarbera, L. Kresge, and N.-C. Lee, “Achieving low-porosity sintering of nano ag paste via pressureless process”, in *2015 IEEE 65th Electronic Components and Technology Conference (ECTC)*, IEEE, 2015, pp. 1795–1802.

[29] C. Chen, Z. Zhang, Q. Wang, *et al.*, “Robust bonding and thermal-stable ag–au joint on enepig substrate by micron-scale sinter ag joining in low temperature pressure-less”, *Journal of Alloys and Compounds*, vol. 828, p. 154 397, 2020.

[30] K. Siow, V. Manikam, and S. Chua, “Process control of sintered ag joint in production for die attach applications”, *Die-Attach Materials for High Temperature Applications in Microelectronics Packaging*, pp. 67–105, 2019.

[31] S. Chen and H. Zhang, “Silver sintering and soldering: Bonding process and comparison”, in *Die-Attach Materials for High Temperature Applications in Microelectronics Packaging*, Springer, 2019, pp. 1–33.

[32] S. Mannan, A. Paknejad, A. Mansourian, and K. Khtatba, “Morphological changes in sintered silver due to atomic migration”, *Die-Attach Materials for High Temperature Applications in Microelectronics Packaging*, pp. 151–163, 2019.

[33] M. Wang, Y. Mei, X. Li, R. Burgos, D. Boroyevich, and G.-Q. Lu, “How to determine surface roughness of copper substrate for robust pressureless sintered silver in air”, *Materials Letters*, vol. 228, pp. 327–330, 2018.

[34] X. Liu and H. Nishikawa, “Improved joint strength with sintering bonding using microscale cu particles by an oxidation-reduction process”, in *2016 IEEE 66th Electronic Components and Technology Conference (ECTC)*, IEEE, 2016, pp. 455–460.

[35] Y. Gao, J. Jiu, C. Chen, K. Suganuma, R. Sun, and Z.-Q. Liu, “Oxidation-enhanced bonding strength of cu sinter joints during thermal storage test”, *Journal of Materials Science & Technology*, vol. 115, pp. 251–255, 2022.

4

Mechanical Properties and Creep Behavior of Cu Sintered Material

To support the stable performance of power electronics devices, the high-temperature reliability of die-attached materials is critical. In this chapter, the constitutive models (yield stress, strain hardening exponent factors) for samples sintered via different applied pressure were obtained, which can be used to describe the room-temperature mechanical properties of the Cu sintered joint. Then, the key mechanical properties such as indentation hardness, elastic modulus, and the creep rate of Cu-sintered die-attach samples were evaluated at various temperatures. The effects of temperature ranging from 150° C to 240° C on these values were investigated. The high-temperature creep behavior was studied and compared for samples sintered with different applied pressures. The results obtained in this chapter can be applied in evaluating the feasibility of the application of the Cu sintering technique at various temperatures in the semiconductor packaging industry.

4.1. INTRODUCTION

IN recent years, the copper sintering technique has emerged as one of the most promising die-attachment solutions in the industry due to its potential high-temperature properties benefits[1]–[9]. Therefore, it is worth to study the thermomechanical properties of sintered DA materials for both the industry and the academy. In material science, hardness and elastic modulus are the important mechanical parameters to describe the resistance to local plastic deformation and the resistance to elastic deformation. For bulk materials, the hardness and elastic modulus can be obtained easily by using the traditional indentation test and tensile test. However, for samples with small sizes, such as die-attach layer, the indentation process and tensile test are hard to carry out on such tiny areas. Some studies have attempted to perform macroscopic indentation tests or tensile experiments using large-size dog-bone samples, while more energy (higher temperature, larger pressure and longer time) input is often required to ensure organic volatilization and particle sintering during the fabrication of such samples. This may cause uneven sintering stages in different areas of the sample. Thus, such macroscopic samples cannot accurately reflect the effects of sintering process parameters.

Recently, the nanoindentation test[10] has drawn more and more attention for the characterization of the mechanical features in the microelectronics packaging field, since it can carry out various parameters-control tests on a micron-size area to evaluate the post-processing properties of the packaging structure. From the indentation testing data, it is possible to obtain the indentation depth, indentation hardness, elastic modulus, and even the constitutive relationship of the sample. Moreover, by installing an additional heating chamber, the test can also be conducted under evaluated temperatures. Therefore, the high-temperature-related creep properties can also be studied via this method. It is reported that the nanoindentation test could be used for the mechanical properties evaluation of the soldering joint and metallic sintered materials[11]–[16]. Leslie et al.[17] and Kraft et al.[18] have applied this technology to the sliver pressureless sintering material to investigate the viscoplastic properties of the sintered joints at room temperature. Long et al.[19] have studied the microstructural effect on the mechanical behavior of the sintered Ag by performing nanoindentations with a Berkovich indenter penetrated up to 2000 nm with different indentation strain rates. Zhang et al.[20] have studied the indentation properties of as-sintered Ag samples with different applied pressure and different testing temperatures. However, up to now, the mechanical reliability of Cu-sintered material at various temperatures has not been fully studied.

In this chapter, the self-developed Cu paste was again adopted to fabricate the sintering die-attach samples. Then, both the room-temperature and high-temperature nanoindentation tests were conducted on the Cu sintering samples prepared by using different sintering pressure to obtain their mechanical properties and reliability. The indentation hardness, indentation modulus, and creep properties were all characterized, and the constitutive models (yield stress, strain hardening exponent factors) were derived. With the above evaluation results, a more in-depth and comprehensive understanding of Cu sintering DA material can be provided, which can definitely boost the application of Cu sintering technology in power electronics more efficiently.

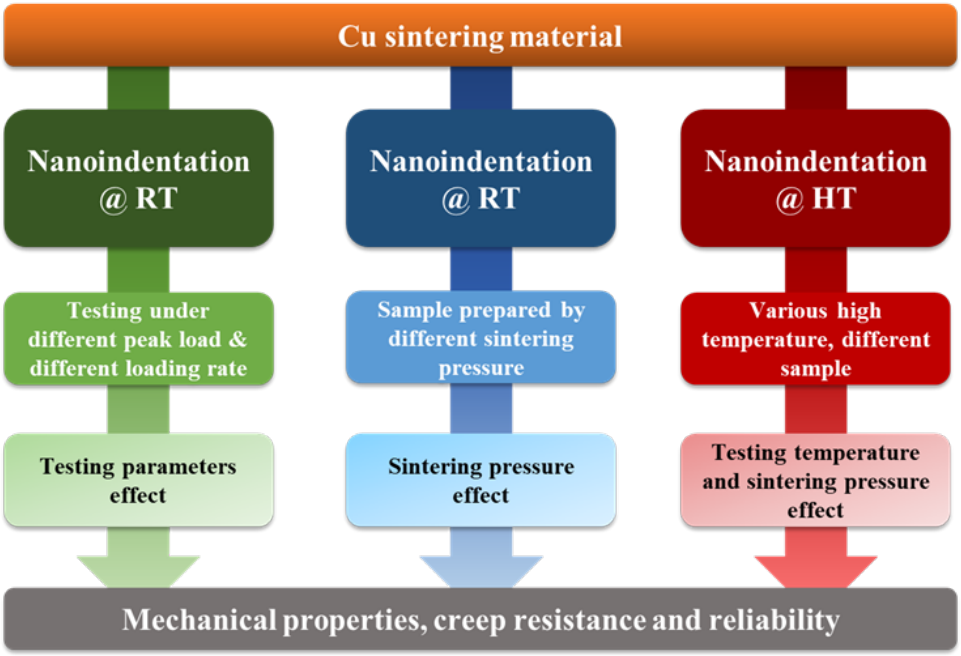
Cu sintering material
Nanoindentation @ RT
Nanoindentation @ RT
Nanoindentation @ HT
Testing under different peak load & different loading rate
Sample prepared by different sintering pressure
Various high temperature, different sample
Testing parameters effect
Sintering pressure effect
Testing temperature and sintering pressure effect
Mechanical properties, creep resistance and reliability

Figure 4.1: The study outline of this chapter.

4.2. Methodology

4.2.1. Sample Preparation

To conduct the nanoindentation test, it is necessary to guarantee the flatness of the surface under testing. In some studies, the cross-section surface of the ion-milled cold mounting sample was adopted. However, it is hard to fulfill the height requirement (< 2 mm) of the nanoindentation heating chamber of the Bruker Hysitron TI980 Nanoindenter in this study. For this reason, there was a specially designed Cu sintered die-attach sample being applied for the nanoindentation test in this chapter, as shown in Fig.4.2. The preparation process is described as follows: First, the Cu paste was printed onto a 10 mm × 10 mm × 1 mm Cu plate. There was a 1 μm Ag coating layer on its surfaces. Then by drying the samples at 150°C for 5 min, the organics would be evaporated. Next, there was a **bare Si dummy dice without any metallic finishing** being placed onto the as-dried paste pad by using the pick & place machine (Tresky T3002 PRO) with 0.5 MPa pressure. The bare Si dice was used to imitate the real dice but without any adhesion with the die-attach layer. The sintering process was then carried out with 10 MPa, 20 MPa and 30 MPa assisted pressure at 250°C for 3 min in Boschman Sinterstar Mini. After sintering, the bare Si die could be easily removed, leaving a dense and well-sintered Cu layer underneath. Finally, in order to produce a finer surface for nanoindentation, the as-sintered samples were polished using an ultra-fine polish texture on a Buehler EcoMet 30. By using the above method, it is not only possible to prepare samples with a large flat test surface that exactly mimics the die-attach process parameters, but also to meet the sample height requirements of the testing equipment.

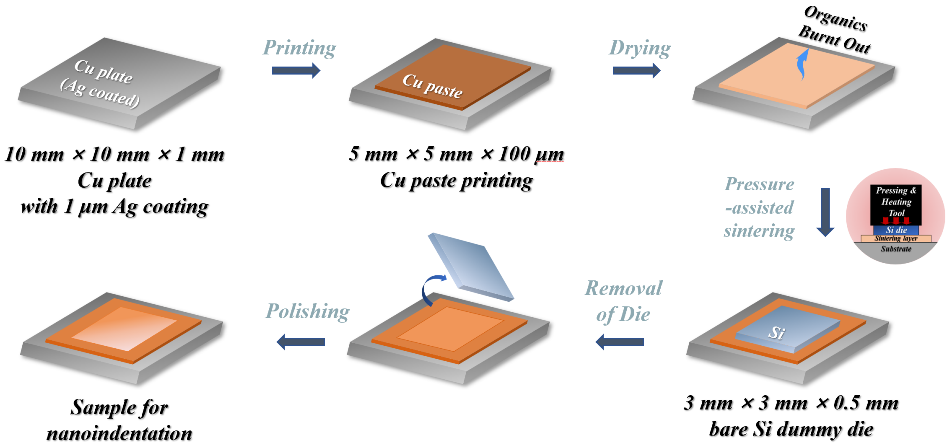
Cu plate
(Ag coated)
10 mm × 10 mm × 1 mm
Cu plate
with 1 μm Ag coating
Printing
Cu paste
5 mm × 5 mm × 100 μm
Cu paste printing
Drying
Organics
Burnt Out
Pressure
-assisted
sintering
Pressing &
Heating
Tool
Si die
Sintering layer
Substrate
Removal
of Die
Si
3 mm × 3 mm × 0.5 mm
bare Si dummy die
Polishing
Sample for
nanoindentation

Figure 4.2: Schematic diagram of the nanoindentation sample preparation process.

4.2.2. NANOINDENTATION TEST AND DISPLACEMENT-LOAD CURVE

THE nanoindentation test was conducted on the Bruker Hysitron TI980 Nanoindenter. The Berkovich indenter was installed. Fig.4.3a is a typical plot of the load shift curve labeled with the testing process and key parameters. Fig.4.3b is the corresponding schematic near the indenter area. It may be noted that the indentation test process can be divided into three sections: loading, holding, and unloading. During the loading section, the indenter will be pushed into the material surface with a constant loading rate (in this study, from 0.1 mN/s to 1.5 mN/s). Then at the pre-defined peak load (in this study, from 10 mN to 150 mN), the indenter will be held for a certain time (in this study, 10 s), and then be released. Real-time load and displacement data, maximum indentation depth, and residual depth will be identified and recorded during testing.

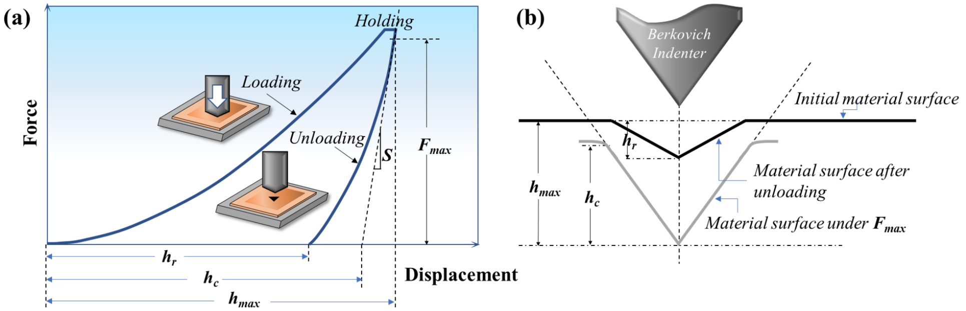
(a)
Force
Holding
Loading
Unloading
S
F_{max}
h_r
h_c
h_{max}
Displacement
(b)
Berkovich
Indenter
Initial material surface
h_r
h_{max}
h_c
Material surface after
unloading
Material surface under F_{max}

Figure 4.3: (a) A typical load-displacement curve of the nanoindentation test. (b) A schematic diagram of the indentation region and the corresponding Berkovich indenter.

4.2.3. Indentation Hardness and Elastic Modulus Calculation

Then the Oliver and Pharr method (OP method)[21] and the method introduced in[22] were used to calculate the indentation hardness and elastic modulus of the samples. First, the indentation hardness can be derived from the following equation:

$$\mathrm{H} = \frac{F_{\max}}{A_C} \tag{4.1}$$

where F_{max} is the peak load from the load-displacement curve and A_C is the projected area of the contact surface. For the Berkovich indenter A_C can be fitted as:

$$A_C = 24.56h_c^2 - 1735h_c + 1.213h_c^{\frac{1}{2}} - 6.599\times 10^5 h_c^{\frac{1}{4}} + 6.182\times 10^5 h_c^{1/8} \tag{4.2}$$

$$h_c = h_{\max} - S\left(h_{\max} - h_r\right) \tag{4.3}$$

where h_c, h_{max}, h_r are the contact depth, the maximum indentation depth and residual depth as shown in Fig.4.3a and b. S is the contact stiffness in the unloading phase. From the microscale view shown in Fig.4.3b, the elastic deformation will recover after the removal of load. Therefore, the residual depth h_r will be slightly smaller than h_{max}.

Next, the elastic modulus can be derived from the initial part of the unloading curve which is assumed to be purely elastic. The following relationship exists between the initial slope of the unloading curve S (also defined as the stiffness of the contact), the reduced elastic modulus E_r, and the indenter contact area A_C:

$$E_r = \frac{1}{\lambda\sqrt{A_C}}\cdot S \tag{4.4}$$

From contact mechanics[23], elastic modulus of the material is related to the reduced elastic modulus through the following equation:

$$\frac{1}{E_r} = \frac{1-\nu^2}{E} + \frac{1-\nu_i^2}{E_i} \tag{4.5}$$

where E_i and ν_i are the elastic modulus and Poisson's ratio for the Berkovich indenter which is known as 1140 GPa and 0.07.

4.2.4. Constitutive Model

To fully describe the mechanical behavior of the material, the constitutive model of such material should be developed[19], [20]. For many engineering pure metals and alloys, their macroscopic elastic-plastic behavior can be approximated by a power-law relationship. Their stress-strain behavior can be expressed as follows:

$$\sigma = \begin{cases} E\varepsilon\left(\sigma \le \sigma_y\right) \\ Y\varepsilon^n\left(\sigma > \sigma_y\right) \end{cases} \tag{4.6}$$

where, E is the elastic modulus, and Y is the strength coefficient. n is the strain hardening index, which reflects the resistance ability of the material to uniform plastic deformation. σ_y is the yield stress, and when $\sigma = \sigma_y$, there is:

$$\sigma_y = E\varepsilon_y = Y\varepsilon_y^n \tag{4.7}$$

where ε_y is the corresponding initial plastic strain. Therefore, according to the equation, when $\sigma > \sigma_y$, the stress-strain behavior can be expressed as:

$$\sigma = Y\varepsilon^n = \frac{\sigma_y}{\varepsilon_y^n}\left(\varepsilon_y + \varepsilon_p\right)^n = \sigma_y\left(1 + \frac{1}{\varepsilon_y}\varepsilon_p\right)^n = \sigma_y\left(1 + \frac{E}{\sigma_y}\varepsilon_p\right)^n \tag{4.8}$$

where, ε_p is actual plastic strain, and together with yield strain ε_y constitute the total strain ε. Therefore, the stress-strain equation can be expressed as:

$$\sigma = \begin{cases} E\varepsilon\left(\sigma \le \sigma_y\right) \\ \sigma_y\left(1 + \frac{E}{\sigma_y}\varepsilon_p\right)^n\left(\sigma > \sigma_y\right) \end{cases} \tag{4.9}$$

Now it is clear that to describe the constitutive model of the material, three physical quantities are required:

- Young's modulus E
- Initial yield stress σ_y
- Strain-hardening index n

In the following sections, all three parameters would be obtained through the nanoindentation test based on Giannakopoulos and Suresh method[24].

4.2.5. CREEP BEHAVIOR

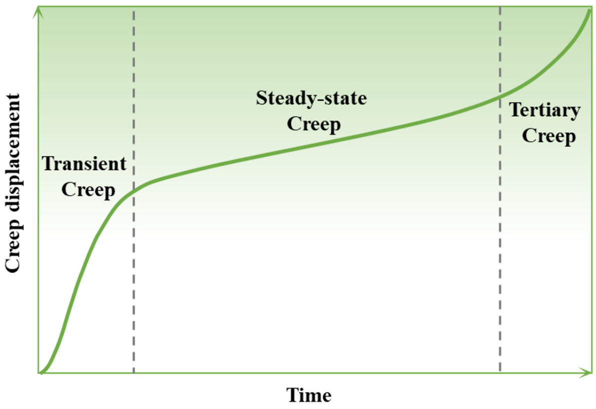

Figure 4.4: A typical time-displacement curve for the creep behavior.

CREEP behavior is a phenomenon of a solid material to deform slowly under persistent stresses[25]. The rate of creep deformation is subject to a combination of intrinsic properties of the material and environmental factors such as temperature, time, and applied load. Fig.4.4 shows a typical curve of creep displacement over time. Normally creep behavior can be divided into three stages[26]. The first stage is also known as initial creep or transient creep. At the beginning of creep, the creep strain rate is always high and then gradually decreases over time. The dominant creep mechanism during this period may be the increase of the dislocation density or the diffusion of material atoms due to the constant load. Then in the secondary phase, or so-called steady-state phase, the creep displacement increases slower but linearly with time since the dislocation density reaches equilibrium. This stage is the longest one and is often used to characterize the creep deformation resistance of materials. In the last stage (also named as the tertiary stage), the strain rate again increases fast because of material failures such as internal cracks or voids formation.

It has been reported that, with the help of sintering technology the junction temperature of power devices can achieve 175°C and even 200°C[27], [28], respectively. Therefore, 150°C, 180°C, 210°C and 240°C were selected to conduct creep study in this study. Then, to find out the sintering pressure effect on the creep resistance, the samples sintered by 10 MPa, 20 MPa and 30 MPa were adopted. The peak load was 70 mN and the holding time was 100 s in these tests.

4.3. NANOINDENTATION STUDY AT ROOM TEMPERATURE

4.3.1. EFFECTS OF PEAK LOAD AT ROOM TEMPERATURE

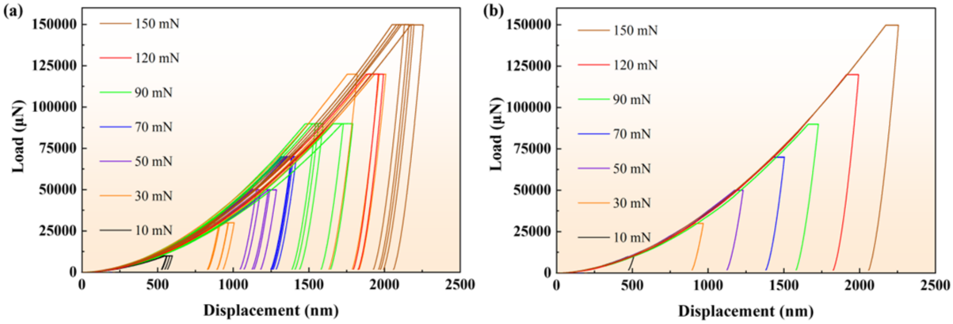

Figure 4.5: (a) The load-displacement curves with different testing peak loads. (b) The clearly aligned load-displacement curves which selected from the complete data.

INDENTATION peak load and loading rate are two testing parameters that may affect the mechanical properties of the material, due to the size effects[29] and substrate effects[30]. It is important to identify the right combination of parameters at the beginning. First of all, to study the peak load effects on mechanical properties, a series of nanoindentation tests were conducted on the Cu sintered samples (prepared by 250°C /3 min/20 MPa) under 10 mN, 30 mN, 50 mN, 70 mN, 90 mN, 120 mN and 150 mN at room temperature. For each parameter, 5 times of indentation were run to check the bias in the results, and in total 35 tests were realized. The strain rate was kept constant at 1.2 mN/s in these tests. The recorded load-displacement curves are shown in Fig.4.5a with different colors for different testing conditions.

It can be noticed that each curve has a similar trend in the loading and unloading phases, which is due to the work hardening of the sintered material as well as the elastic recovery behavior. In addition, fluctuations in the displacement curves under the same load can be observed, which may be a result of deviations brought by the sintered materials with microscopic porosity. This could also explain the deviations in the E-modulus and indentation hardness calculation results presented in the following sections. According to[31], it is possible to select the clearly aligned curves for representing the material response of all peak-load cases as displayed in Fig.4.5b. It can be found that starting from the loading part, the required peak load increases from 10 mN to 150 mN as the maximum indentation depth increases from near 500 nm to over 2000 nm. This is mainly due to the strain-hardening effect of the sintered Cu and the SEM images for the indentation spots (Fig.4.6) also confirm these phenomena.

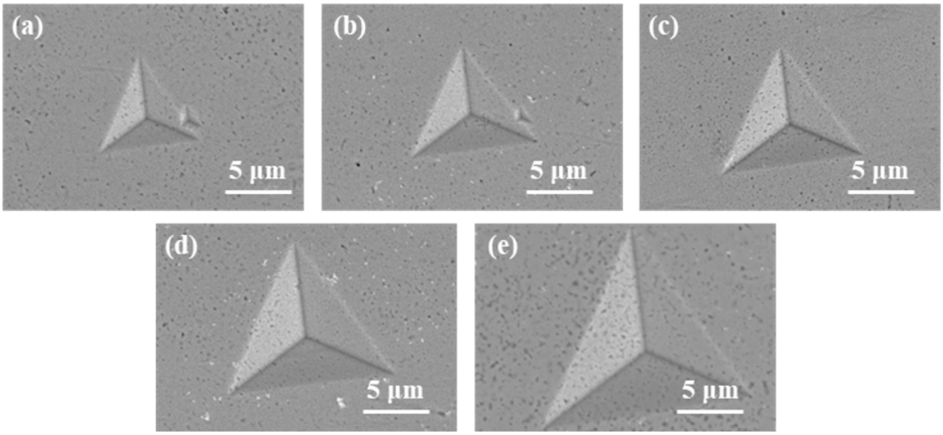

Figure 4.6: The SEM images of the indentation imprints of the tests with (a) 30 mN,(b) 50 mN,(c) 70 mN,(d) 90 mN,(e) 120 mN.

At the holding stage, the displacement still increases as a function of time due to the creep effect. Then when the indentation load is removed, elastic deformation recovery can be observed. The following is the elastic recovery ratio calculated by[29]:

$$\varepsilon = (h_{\max} - h_r)\, h_{\max} \tag{4.10}$$

As shown Table4.1, the residual depth and elastic recovery ratio increase simultaneously with the maximum load. Test results from 10 mN to 70 mN revealed a large increase in these values, indicating that characterization at lower loads may be inaccurate and can cause differences in results due to the choice of test parameters. From 70 mN to 150 mN, the fluctuation of the test result reaches relative stability. Therefore, a peak load of not less than 70 mN should be selected for testing. In addition, the elastic recovery rate of Cu sintered samples is between 5~10% under different indentation depths, indicating that all Cu sintered samples had large plastic deformation.

Fig.4.7 shows the evolution of indentation hardness (blue cubes) and elastic modulus (red circles) of the Cu-sintered die-attach samples at different peak loads. As the peak

Table 4.1: The maximum displacement, residual depth and elastic recovery ratio values of nanoindentation test with different peak load.

Peak load (mN)	Maximum displacement (nm)	Residual depth (nm)	Elastic recovery ratio
10	580.9	547.9	5.68%
30	965.6	892.1	7.61%
50	1285.6	1181.5	8.10%
70	1398.5	1263.4	9.66%
90	1593.7	1438.3	9.75%
120	1819.8	1632.16	10.30%
150	2177.6	1971.3	9.48%

load increases, the hardness value increases from around 1.28 GPa to near 1.59 GPa and the E-modulus decreases from 105 GPa to 95 GPa. As mentioned in the previous section, the maximum load required increases with the increasing indentation depth, and therefore, this change in indentation properties is due to the indentation size effect (ISE). ISE is evident when the indentation depth is below 1000 nm or the corresponding peak load is less than 30 mN, while after 70 mN of peak load (1400 nm of maximum depth), the trend is no longer evident.

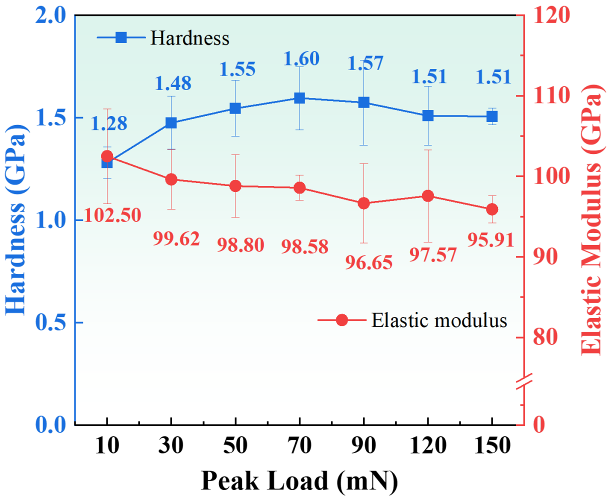

Figure 4.7: The indentation hardness and elastic modulus for different testing peak loads.

A study of the indentation properties of silver sintered materials[19] found that the original porosity of the sintered body reduced the hardness test value. As the peak load increased, the originally porous locations were compacted and the measured hardness values were increased. It is also reported[30], [31] that when the indentation was shallow, the indentation properties were affected by the environment, the substrate, surface oxidation, and deformation in shallow layers, while when the indentation was too large, it was affected by sub-grain, underlying porosity and substrate effect. Therefore, an indentation depth of more than 1500 nm is necessary to remove the influence of ISE and ensure stable experimental results. The stable value of hardness and elastic modulus of the presented work are around 1.59 ± 0.15 GPa and 98.5 ± 1.57 GPa.

4.3.2. Effects of Loading Rate at Room Temperature

The load-displacement curves of Cu sintered sample at various loading rate from 0.1 mN/s to 1.5 mN/s is displayed in Fig.4.8a. It can be found that with higher loading rate, the curve moves to the left, and the loading part of the curve becomes steeper. At the same time, both the displacement of the holding phase and the maximum indentation depth gradually decrease with the increasing loading rate. This is mainly due to the variation of elastic and plastic properties with the increasing of the loading rates. It can also realize that the curves which were tested at the rate faster than 0.9 mN/s overlap with each other. Fig.4.8b shows that with the increase of loading rate from 0.1 mN/s to 0.9 mN/s, both of the indentation hardness and elastic modulus increased gradually. But from 0.9 mN/s, the two properties start to became stable at around 1.59 ± 0.154 GPa and 99.5 ± 0.86 GPa.

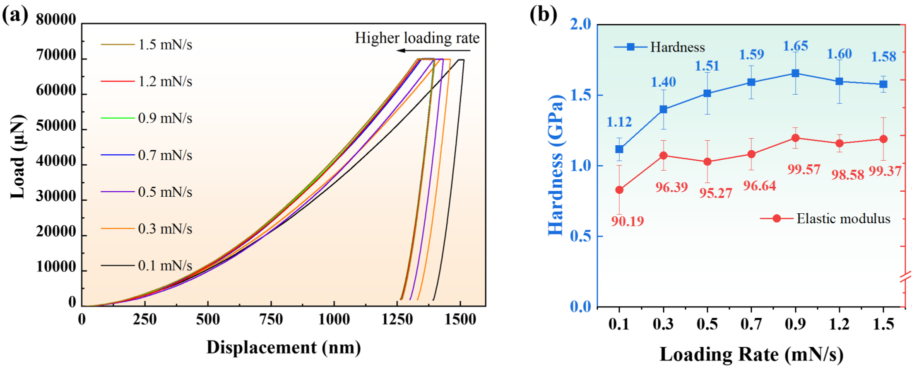

Figure 4.8: (a) The load-displacement curves and (b) the indentation hardness and elastic modulus for different testing loading rate.

During the indentation test, different testing loading rates actually result in plastic deformation of the sample at different strain rates. In many studies it has been found that the strain rate sensitivity of hardness was stronger than that of elastic modulus[19], [29], [32]. One of the reasons could be the thermal activation process of gliding dislocation responsible for the deformation[33]. When the strain rate is accelerated, the dislocation gliding is not activated in time, so that plastic deformation cannot occur immediately, which would macroscopically result in higher hardness. In addition, some studies also found lots of material "pile-up" effects at the edge of the indentation spots during the low-speed test, which caused the increase of true contact area A_C. According to the calculation equation of the indentation hardness and elastic modulus, higher A_C value will directly reduce the H and E. In conclusion, considering both the effects of ISE and loading rate, 70 mN with 1.2 mN/s were selected as the testing parameters for the subsequent high temperature experiments.

4.3.3. EFFECT OF SINTERING PRESSURE AT ROOM TEMPERATURE

The nanoindentation load-displacement curves for Cu sintered samples prepared by different sintering pressure are shown in Fig.4.9. It is clear that the samples which were sintered by larger pressure contained steeper loading parts and smaller indentation depths, indicating higher resistance to plastic deformation. From the previous chapters, it is found that pressure is the most important factor that can influence the bonding performance of die-attachment. Fig.4.9b also confirms that higher sintering pressure can also enhance the elastic modulus and indentation hardness of the sample. It is believed that this effect comes from the more densification and stronger sintering networking formed in higher applied pressure scenario. Moreover, the effect of sintering pressure becomes less significant at pressures above 20 MPa, which is also consistent with the results in previous chapter.

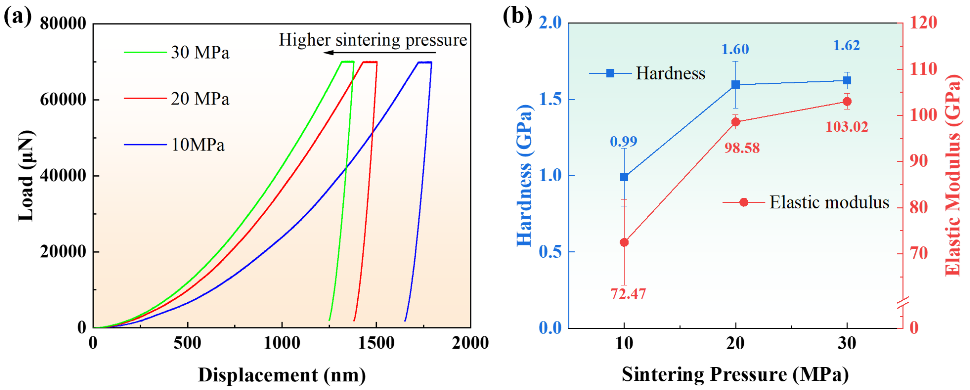

Figure 4.9: (a) The load-displacement curves and (b) the indentation hardness and elastic modulus of Cu sintered samples prepared by different sintering pressure.

4.3.4. CONSTITUTIVE MODELING DERIVATION

In this section, the constitutive model of the Cu sintered samples prepared by different pressure will be derived. As mentioned in the methodology section, three physical quantities are required to obtain the constitutive model of the material, which are: Young's modulus E, initial yield stress σ_y, and strain-hardening index n. Since the elastic modulus E has been obtained in the last section, the main tasks in this section are the derivation of the yield stress σ_y and strain-hardening index n.

For the calculation of yield stress σ_y, the Giannakopoulos[24] method is always used. As shown in the Fig.4.10, the volume under the indenter can be divided into different regions based on the different deformation characteristics. The region directly under the indenter is the "plastic cutting region" as marked by dark green color, where pure plastic deformation happens. Then in the area far way from the surface, it is the pure elastic region, as marked by light green color. When releasing the indenter, the deformation will recover totally. Between them, it is the elasto-plastic deformation region. There is a unique characteristic plastic strain between the pure plastic region and elasto-plastic region, as the red dash line in the Fig.4.10. Giannakopoulos et al.[24] derived the value

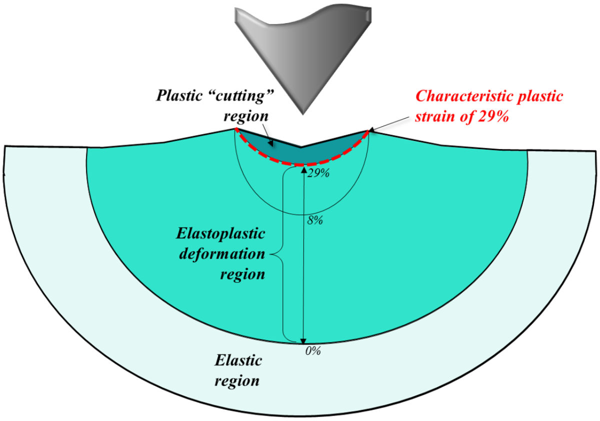
Plastic "cutting" region
Characteristic plastic strain of 29%
29%
8%
Elastoplastic deformation region
0%
Elastic region

Figure 4.10: The schematic diagram of different regions with elastic or plastic flow at the tip of a indenter.

of this characteristic strain by finite element simulation as 29%.

The ratio of the residual depth (h_r) to the maximum indentation depth (h_{max}) is indicative of the extent of plastic deformation and strain hardening[34], [35], as depicted by the equation:

$$\frac{\sigma_{0.29}-\sigma_y}{0.29E_r} = 1-0.142\frac{h_r}{h_{max}} - 0.957\left(\frac{h_r}{h_{max}}\right)^2 \tag{4.11}$$

What's more, the loading phase of the nanoindentation curve can be fitted by least squares method to a quadratic function $F = Ch^2$, where C is the indentation curvature which is a measure of the "resistance" of the material to indentation. Three-dimensional finite-element simulations of elasto-plastic indentation along with experiments provide the following result[24]:

$$C = \frac{P}{h^2} = M_1\sigma_{0.29}\left(1+\frac{\sigma_y}{\sigma_{0.29}}\right)\left[M_2+\ln\left(\frac{E_r}{\sigma_y}\right)\right] \tag{4.12}$$

The constant in the equation are $M_1 = 6.618$ and $M_2 = -0.875$ for the Berkovich indenter.

Then by combining the above two equations, the $\sigma_{0.29}$ and σ_y can be obtained. Last but not the least, for the calculation of strain hardening rate, the stress and strain values of two points are needed:

$$n = \frac{\ln\left(\frac{\sigma_2}{\sigma_1}\right)}{\ln\left(\frac{\varepsilon_2}{\varepsilon_1}\right)} \tag{4.13}$$

From the discussion above, it is rational to select 0.2% yielding point and 29% characteristic point for this calculation. Hence, we have:

$$\varepsilon_{0.29} = 0.29 \tag{4.14}$$

$$\varepsilon_y = 0.002 \tag{4.15}$$

$$n = \frac{\ln\left(\frac{\sigma_{0.29}}{\sigma_y}\right)}{\ln\left(\frac{\varepsilon_{0.29}}{\varepsilon_y}\right)} = \frac{\ln\sigma_{0.29} - \ln\sigma_y}{\ln\left(\frac{0.29}{0.002}\right)} \approx \frac{\ln\sigma_{0.29} - \ln\sigma_y}{4.98} \tag{4.16}$$

The calculated σ_y and n values are summarized in the following equations. As sintering pressure increases, the yield strength and strain-hardening index increase as well. These quantitative results can be used to explain the dependence of plastic deformation resistance on the sintering pressure.

$$\sigma_{10MPa} = \begin{cases} 72.47\varepsilon(\sigma \le 0.330GPa) \\ 0.330\left(1 + 219.6\varepsilon_p\right)^{0.313}(\sigma > 0.330GPa) \end{cases} \tag{4.17}$$

$$\sigma_{20MPa} = \begin{cases} 98.58\varepsilon(\sigma \le 0.533GPa) \\ 0.533\left(1 + 184.8\varepsilon_p\right)^{0.339}(\sigma > 0.533GPa) \end{cases} \tag{4.18}$$

$$\sigma_{30MPa} = \begin{cases} 103.02\varepsilon(\sigma \le 0.540GPa) \\ 0.540\left(1 + 190.8\varepsilon_p\right)^{0.343}(\sigma > 0.540GPa) \end{cases} \tag{4.19}$$

4.4. NANOINDENTATION STUDY AT HIGH TEMPERATURE

4.4.1. DISPLACEMENT-LOAD CURVES AT HIGH TEMPERATURE

IN this section, the indentation tests of the Cu sintered sample prepared by 10 MPa, 20 MPa and 30 MPa were conducted at 150°C, 180°C, 210°C, and 240°C to study the effect of the elevated temperature. Fig.4.11 displays the displacement-load curves of the different samples at various temperatures. First, within each diagram the displacement-load curve tested at lower temperatures are much steeper and contains a smaller indentation depth than that at higher temperatures. This indicates that higher test (working) temperatures will result in earlier and greater plastic deformation even at the same load. This is one of the reasons why sintered materials have a greater risk of failure when working at high temperatures.

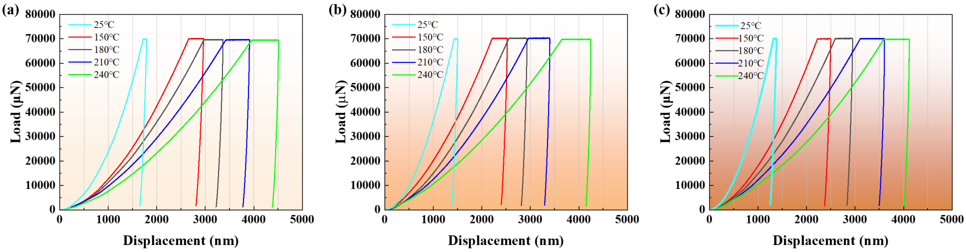

Figure 4.11: The load-displacement curves tested at 150°C, 180°C, 210°C, and 240°C of samples sintered by applying (a) 10 MPa, (b) 20 MPa, and (c) 30 MPa assisted pressure.

Second, through a cross-comparison among Fig.4.11a, b and c, we found that the samples prepared by higher sintering pressure contain shorter indentation depth, and show higher plastic resistance. This is consistent with previous pressure effects on bonding properties, which can be attributed to better sintering neck growth, lower porosity generation, and a more complete sintering phase in high-pressure scenarios. Also from the SEM images of the indentation area in Fig.4.12, the effects of the testing temperature on the indentation size and plastic deformation are evident. However, the sintered samples prepared by higher pressures exhibited better resistance to plastic deformation at the same test temperature. This means that to achieve the same indentation size or damage level, the high-pressure sintered sample needs to be applied higher load, or worked for a longer period of time.

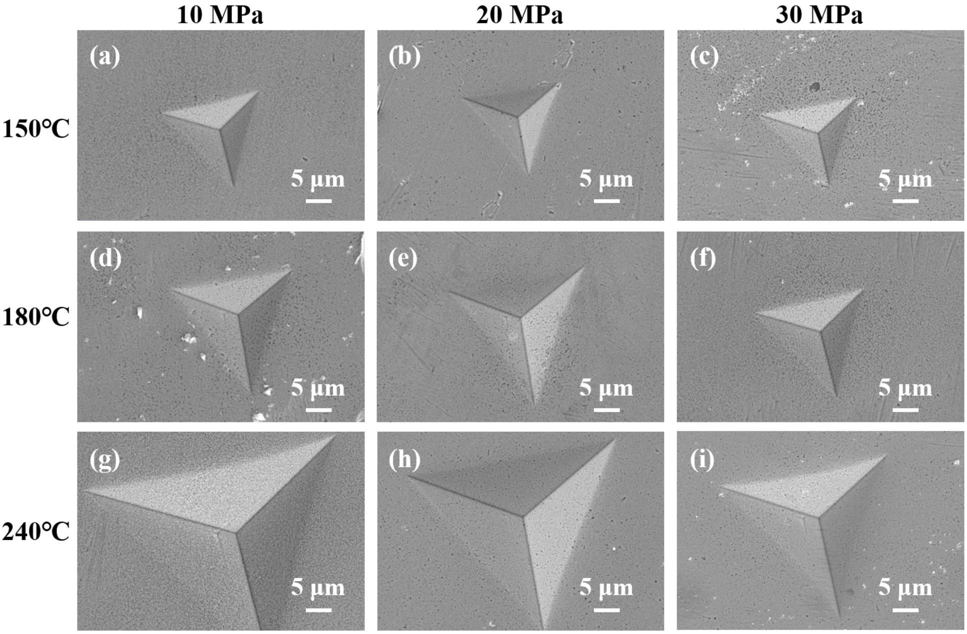

Figure 4.12: The SEM images of the indentation imprints of the different samples and testing temperatures: (a) to (c) at 150°C. (d) to (f) at 180°C. (g) to (i) at 240°C. From left to right are the sample sintered by 10 MPa, 20 MPa and 30 MPa.

4.4.2. HARDNESS AND ELASTIC MODULUS AT HIGH TEMPERATURE

INDENTATION HARDNESS

THE indentation hardness results for different Cu sintered samples (10 MPa to 30 MPa) under different testing temperatures (150°C to 240°C) are shown in Fig.4.13. First, the sample prepared with the lowest pressure (10 MPa) contained the lowest indentation hardness at each temperature. By increasing the sintering pressure to 20 MPa, both parameters were elevated a lot. However, there was little difference between the results of 20 MPa and 30 MPa. Then, the indentation hardness shows an obvious decrease trend with the increase of temperature for 20 MPa and 30 MPa scenarios. This is consistent with the findings in the displacement-load curves in the previous section, which indi-

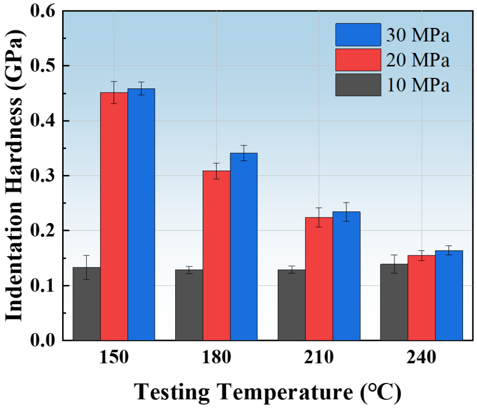

Figure 4.13: The indentation hardness of Cu sintered samples tested at 150°C to 240°C.

cates that the softening of materials and the reduced resistance to plastic deformation at high temperatures require special attention.

The softness or hardness of the metal material depends to a large extent on the ease of dislocation movement. The hindering effect on the dislocation motion will be weakened at high temperatures, and more dislocations will be thermally activated to move. By fitting the data of the 20 MPa and 30 MPa cases in Fig.4.13a, it reveals an exponential degradation law of hardness regarding the temperature as shown in Fig.4.14. The fitted exponential degradation equation of hardness is as follows:

$$H = a_1 \times \exp(-B \times T) + c_1 \tag{4.20}$$

where H is indentation hardness, and B is the factor that can reflect the sensitivity of the hardness value to the temperature. The negative sign means that the hardness value decreases with increasing temperature. The larger the absolute value of the coefficient B, the more temperature sensitive the hardness of the Cu sintered sample is, and the faster the hardness decreases with increasing temperature. a_1 and c_1 are the factors that can affect the absolute value of hardness.

Firstly, the fitting results show that the R-Square values for both curves are near 0.998, indicating that the confidence of the fitting results is relatively high. It can be assumed that the fitted curves agree with the exponential degradation law because the dislocation density is strongly influenced by the thermally induced vacancies at high temperatures. The vacancies will increase exponentially when temperature is increased, which follows the Arrhenius relationship[20], [36]:

$$N_v = N \times \exp\left(-\frac{Q_v}{RT}\right) \tag{4.21}$$

where N_v is the number of vacancies, N is the number of atoms. Q_v is the activation energy required for vacancy generation, R is the universal gas constant, and T is the temperature. Comparing the values of the three fitting factors, it can be concluded that

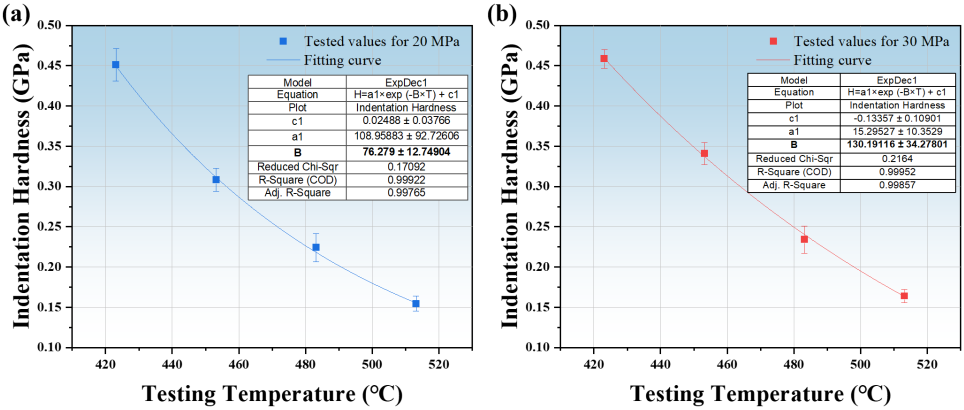

Figure 4.14: The fitting curves for indentation hardness of the 20 MPa and 30 MPa sintered samples.

higher sintering pressure is effective in increasing hardness, but also leads to the increased temperature sensitivity of hardness. This phenomenon was also found in other works[20], [32].

For the samples prepared by 10 MPa pressure, the indentation hardness changed very little with increasing temperature. This is very much like the relatively smooth phase of change at the end of the exponential relationship graph line. If so, the 10 MPa sample reached the smooth phase earlier than the samples sintered by higher pressure, which indicates that samples prepared at low pressure are less resistant to a decrease in hardness with increasing temperature. It is difficult to derive the fitting function for the hardness values of the 10 MPa sample, since at 240°C there was a small abnormal increase. This is probably due to the fact that the 10 MPa sample was not fully sintered as mentioned in previous section, and therefore a further densification process occurred during the high temperature (near 250°C) indentation test, leading to an improvement in hardness property. Although the increased hardness seems to be a positive sign, this type of phenomenon should be avoided, as in practice this will lead to changes in the material's properties in a way that defies the original design, creating failures.

ELASTIC MODULUS

THEN the elastic modulus evolution against various temperatures of the different Cu sintered samples is shown in Fig.4.15. Similar with the hardness dependence on pressure, the elastic modulus can be enhanced by increasing the sintering pressure. However, the elastic modulus decreased linearly with increasing temperature as follows:

$$E = d + e \times T \tag{4.22}$$

where, d and e are the fitting constants which can be obtained from Fig.4.13b. d can reflect the elastic modulus at low temperatures and factor e can reflect the temperature sensitivity of elastic modulus of the sintered material. A regression fit of the elastic modulus versus test temperature was performed for the Cu-sintered samples prepared by different pressures to obtain the elastic modulus dependence on temperature:

$$E_{10MPa} = 54.35 - 3.76 \times T \tag{4.23}$$

$$E_{20MPa} = 111.45 - 0.115 \times T \tag{4.24}$$

$$E_{30MPa} = 123.82 - 0.143 \times T \tag{4.25}$$

The larger the absolute value of the coefficient e, the more temperature sensitive the elastic modulus of the Cu sintered sample is, and the faster the elastic modulus decreases with increasing temperature. The negative sign means that the elastic modulus value decreases with increasing temperature. Since the elastic properties of the material can be affected by the atomic activity and distance between atoms, the elevated atomic activity at higher temperatures leads to a decrease in elastic resistance. Similar trends have been reported in different works as well[20], [32]. In addition, by comparing the sensitivity factor e for different samples, a similar trend to the hardness sensitivity factor was observed, that too high or too low sintering pressure may have a negative impact on the temperature sensitivity of the elastic resistance. Therefore, the sintering conditions should be selected taking into account their practical effects on different properties.

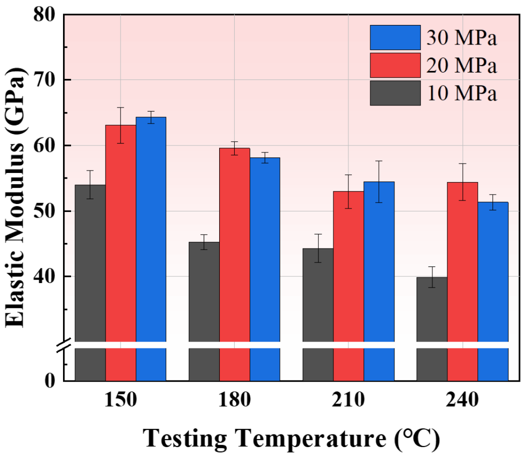

Figure 4.15: The elastic modulus of Cu sintered samples tested at 150°C to 240°C.

4.4.3. CREEP EFFECT AT HIGH TEMPERATURE

FINALLY, the creep behavior of Cu sintered samples at 150°C to 240°C were studied via the nanoindentation test. To conduct this study, the 70 mN of peak load was kept constant for another 100 s to record the creep distance. Fig.4.16 shows the creep displacement curves against creep time at various temperatures. All three figures show a similar trend that the more severe creep plastic deformation occurred when tested at higher testing temperatures.

At the beginning of each curve, the slope is high, as the sample was in the initial creep phase. The dominant creep mechanism during this period may be the increase of the dislocation density or the atomic diffusion due to the constant load. Then, it can

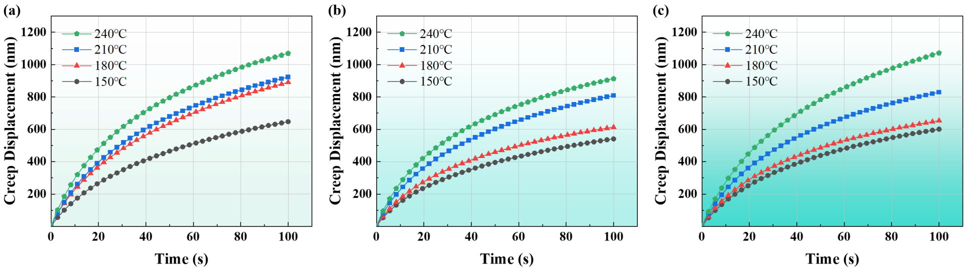

Figure 4.16: The high-temperature creep time-displacement curves for Cu sintering samples prepared by applying (a) 10 MPa, (b) 20 MPa and (c) 30 MPa assisted pressure.

be found that the creep rate is becoming slower after 10 s, which is due to the transition from the initial creep stage to the secondary stage. At this stage, the creep displacement increases slower but linearly with time since the dislocation density reaches equilibrium. Then by analyzing the slope of the linear part, the creep rate evolution can be obtained. It can be seen that the creep rate is increased along with the increasing temperature. That means, at a higher temperature, the Cu-sintered sample is more likely to creep faster. Meanwhile, we also found that when sintering pressure was enhanced from 10 MPa to 20 MPa, the creep rate decreased at all temperatures. Therefore, the resistance of creep can be improved by increasing the sintering pressure. But the increasing effect comes to a marginal over 20 MPa, which is also consistency with the previous discussion.

4.5. CONCLUSION

IN this chapter, key mechanical properties such as indentation hardness, elastic modulus and creep rate of Cu sintered samples were evaluated to verify the feasibility of this technique for application in die-attachment processes. First of all, the peak load (from 10mN to 150 mN) and loading rate (from 0.1 mN/s to 1.5 mN/s) effect on the indentation hardness and elastic modulus were investigated. The tested displacement-load curves were used to analyze the elastic-plastic properties and to compute these key mechanical parameters. The ISE is found to be evident when the indentation depth is below 1000 nm and the corresponding peak load is less than 50 mN. But after 70 mN of peak load (1500 nm of maximum depth), the mechanical properties were gradually constant. Loading rate has a similar effect on these parameters. As it increases from 0.1 mN/s to 0.9 mN/s, both the indentation hardness and the elastic modulus gradually increase as well. But from 0.9 mN/s, the two properties start to become stable at around 1.59 ± 0.154 GPa and 99.5 ± 0.86 GPa. The potential causes are mainly the work hardening effect, pores densification, and pile-up phenomena during the indentation test. Therefore, to ensure stable experimental results, an indentation depth of more than 1500 nm and a loading rate over 0.9 mN/s are necessary. By using the stable testing parameters, the constitutive models (yield stress, strain hardening exponent factors) for samples sintered via different applied pressure were obtained, which can be used to describe the room-temperature mechanical properties of the Cu-sintered joint. Next, the effects of temperature ranging from 150°C to 240°C on the indentation hardness and elastic modulus were investigated. In addition, the creep behavior including the steady-state creep strain rate has been studied and compared for samples sintered with different applied pressures. Higher temperatures were found to result in more severe creep deformations. However, higher sintering pressure can effectively improve the creep resistance against plastic deformation. But the increasing effect comes to a marginal over 20 MPa, which provides a hint to the selection of the sintering process parameters in practice.

REFERENCES

[1] B. Zhang, A. Damian, J. Zijl, *et al.*, “In-air sintering of copper nanoparticle paste with pressure-assistance for die attachment in high power electronics”, *Journal of Materials Science: Materials in Electronics*, vol. 32, no. 4, pp. 4544–4555, 2021.

[2] Y. Zhang, P. Zhu, G. Li, *et al.*, “Easy separation of cuo nanocrystals with high catalytic activity”, *Materials Letters*, vol. 212, pp. 332–335, 2018.

[3] J. Yan, G. Zou, A. Wu, J. Ren, A. Hu, and Y. N. Zhou, “Polymer-protected cu-ag mixed nps for low-temperature bonding application”, *Journal of electronic materials*, vol. 41, no. 7, pp. 1886–1892, 2012.

[4] C. Chen, A. Iwaki, A. Suetake, K. Sugiura, K. Kanie, and K. Suganuma, “Low temperature cu sinter joining on different metallization substrates and its reliability evaluation with a high current density”, in *2021 33rd International Symposium on Power Semiconductor Devices and ICs (ISPSD)*, IEEE, 2021, pp. 387–390.

[5] T. F. Chen and K. S. Siow, “Comparing the mechanical and thermal-electrical properties of sintered copper (cu) and sintered silver (ag) joints”, *Journal of alloys and Compounds*, vol. 866, p. 158 783, 2021.

[6] S. K. Bhogaraju, O. Mokhtari, F. Conti, and G. Elger, “Die-attach bonding for high temperature applications using thermal decomposition of copper (ii) formate with polyethylene glycol”, *Scripta Materialia*, vol. 182, pp. 74–80, 2020.

[7] Y. Gao, H. Zhang, W. Li, *et al.*, “Die bonding performance using bimodal cu particle paste under different sintering atmospheres”, *Journal of Electronic Materials*, vol. 46, no. 7, pp. 4575–4581, 2017.

[8] Y. Mou, Y. Peng, Y. Zhang, H. Cheng, and M. Chen, “Cu-cu bonding enhancement at low temperature by using carboxylic acid surface-modified cu nanoparticles”, *Materials Letters*, vol. 227, pp. 179–183, 2018.

[9] Y. Kobayashi, T. Shirochi, Y. Yasuda, and T. Morita, “Preparation of metallic copper nanoparticles in aqueous solution and their bonding properties”, *Solid state sciences*, vol. 13, no. 3, pp. 553–558, 2011.

[10] C. A. Schuh, “Nanoindentation studies of materials”, *Materials today*, vol. 9, no. 5, pp. 32–40, 2006.

[11] X. Kong, F. Sun, M. Yang, and Y. Liu, “High temperature creep properties of low-ag cu/sn-ag-cu-bi-ni/cu solder joints by nanoindentation method”, *Soldering & Surface Mount Technology*, 2016.

[12] N.-R. Kang, E.-J. Gwak, H. Jeon, E. Song, and J.-Y. Kim, "Microstructural effect on time-dependent plasticity of nanoporous gold", *International Journal of Plasticity*, vol. 109, pp. 108–120, 2018.

[13] X. Long, X. Zhang, W. Tang, S. Wang, Y. Feng, and C. Chang, "Calibration of a constitutive model from tension and nanoindentation for lead-free solder", *Micromachines*, vol. 9, no. 11, p. 608, 2018.

[14] G. He, W. Hongcheng, and Y. Yao, "Creep of sintered porous micron-silver: Nanoindentation experiment and theoretical analysis", *Journal of Materials Science*, vol. 56, no. 32, pp. 18 281–18 299, 2021.

[15] D. Chen, G.-Y. Zhou, Z. Liu, and S.-T. Tu, "Nanoindentation experimental study on mechanical properties of as-cast bni-2 solder alloy", *Procedia Engineering*, vol. 130, pp. 652–661, 2015.

[16] J. Fan, H. Zhai, Z. Liu, *et al.*, "Microstructure evolution, thermal and mechanical property of co alloyed sn-0.7 cu lead-free solder", *Journal of Electronic Materials*, vol. 49, no. 4, pp. 2660–2668, 2020.

[17] D. Leslie, A. Dasgupta, and C. Morillo, "Viscoplastic properties of pressure-less sintered silver materials using indentation", *Microelectronics Reliability*, vol. 74, pp. 121–130, 2017.

[18] S. Kraft, S. Zischler, N. Tham, and A. Schletz, "B3. 3-properties of a novel silver sintering die attach material for high temperature-high lifetime applications", *Proceedings SENSOR 2013*, pp. 242–247, 2013.

[19] X. Long, B. Hu, Y. Feng, C. Chang, and M. Li, "Correlation of microstructure and constitutive behaviour of sintered silver particles via nanoindentation", *International Journal of Mechanical Sciences*, vol. 161, p. 105 020, 2019.

[20] H. Zhang, Y. Liu, L. Wang, F. Sun, X. Fan, and G. Zhang, "Indentation hardness, plasticity and initial creep properties of nanosilver sintered joint", *Results in Physics*, vol. 12, pp. 712–717, 2019.

[21] W. C. Oliver and G. M. Pharr, "An improved technique for determining hardness and elastic modulus using load and displacement sensing indentation experiments", *Journal of materials research*, vol. 7, no. 6, pp. 1564–1583, 1992.

[22] X. Hou and N. M. Jennett, "A method to separate and quantify the effects of indentation size, residual stress and plastic damage when mapping properties using instrumented indentation", *Journal of Physics D: Applied Physics*, vol. 50, no. 45, p. 455 304, 2017.

[23] P. Wriggers and T. A. Laursen, *Computational contact mechanics*. Springer, 2006, vol. 2.

[24] A. Giannakopoulos and S. Suresh, "Determination of elastoplastic properties by instrumented sharp indentation", *Scripta materialia*, vol. 40, no. 10, pp. 1191–1198, 1999.

[25] S. Raj and T. Langdon, "Creep behavior of copper at intermediate temperatures—i. mechanical characteristics", *Acta Metallurgica*, vol. 37, no. 3, pp. 843–852, 1989.

[26] W. Blum, P. Eisenlohr, and F. Breutinger, “Understanding creep—a review”, *Metallurgical and Materials Transactions A*, vol. 33, no. 2, pp. 291–303, 2002.

[27] K. Yasui, S. Hayakawa, M. Nakamura, *et al.*, “Improvement of power cycling reliability of 3.3 kv full-sic power modules with sintered copper technology for t j, max= 175° c”, in *2018 IEEE 30th International Symposium on Power Semiconductor Devices and ICs (ISPSD)*, IEEE, 2018, pp. 455–458.

[28] Z. Zhang, C. Chen, A. Suetake, M.-C. Hsieh, and K. Suganuma, “Reliability of ag sinter-joining die attach under harsh thermal cycling and power cycling tests”, *Journal of Electronic Materials*, vol. 50, no. 12, pp. 6597–6606, 2021.

[29] X. Niu, G. Dong, X. Li, X. Geng, and J. Zhou, “Effect of indentation depth and strain rate on mechanical properties of sn0.3ag0.7cu”, *Microelectronics Reliability*, vol. 128, p. 114 429, 2022.

[30] R. Saha and W. D. Nix, “Effects of the substrate on the determination of thin film mechanical properties by nanoindentation”, *Acta materialia*, vol. 50, no. 1, pp. 23–38, 2002.

[31] L. Madej, A. Legwand, M. Setty, *et al.*, “Evaluation of capabilities of the nanoindentation test in the determination of flow stress characteristics of the matrix material in porous sinters”, *Archives of Civil and Mechanical Engineering*, vol. 22, no. 1, pp. 1–10, 2022.

[32] J. Fan, T. Gu, P. Wang, W. Cai, X. Fan, and G. Zhang, “Constitutive modeling of sintered nano-silver particles: A variable-order fractional model versus an anand model”, in *2021 22nd International Conference on Thermal, Mechanical and Multi-Physics Simulation and Experiments in Microelectronics and Microsystems (EuroSimE)*, IEEE, 2021, pp. 1–4.

[33] R. Kasada, D. Ishii, M. Ando, H. Tanigawa, M. Ohata, and S. Konishi, “Dynamic tensile properties of reduced-activation ferritic steel f82h”, *Fusion Engineering and Design*, vol. 100, pp. 146–151, 2015.

[34] S. Suresh and A. Giannakopoulos, “A new method for estimating residual stresses by instrumented sharp indentation”, *Acta materialia*, vol. 46, no. 16, pp. 5755–5767, 1998.

[35] A. Giannakopoulos and S. Suresh, “Determination of elastoplastic properties by instrumented sharp indentation”, *Scripta materialia*, vol. 40, no. 10, pp. 1191–1198, 1999.

[36] J. Fan, D. Jiang, H. Zhang, *et al.*, “High-temperature nanoindentation characterization of sintered nano-copper particles used in high power electronics packaging”, *Results in Physics*, vol. 33, p. 105 168, 2022.

5

APPLICATION AND CHARACTERIZATION OF CU SINTERED SIC POWER MODULES

In this chapter, the reliability of the Cu-sintered die-attach units and the static/dynamic characteristics of the Cu-sintered SiC MOSFET power modules were studied. The self-developed Cu paste and the pressure-assisted sintering die-attach process (250° C/3 min/20 MPa) were adopted to conduct the study. As a benchmark, a silver-sintered SiC module was set in parallel. First of all, the effects of the 150° C/1000 hours high-temperature storage test and -40° C ~ 150° C /1000 cycles thermal cycling test on the shear strength, drain-source on-state resistance (R_{DSon}*) and thermal resistance (*$R_{th(jc)}$*) reliability were investigated. Then, the output and switching performance of the Cu and Ag sintered SiC MOSFET power modules were evaluated. The experimental results indicated that the mechanical and electrical performance of the Cu-sintered SiC module was at the same level as the Ag-sintered module. Considering the comprehensive cost-performance balance, the presented Cu sintering technology is quite promising for the wide-bandgap semiconductors power electronics packaging application.*

5.1. INTRODUCTION

POWER electronics device is a greatly integrated solid-state semiconductor electronics being employed to control and converse the high-power electric power to the demanding form for the end user [1]. Thanks to the outstanding properties of WBG semiconductors, the performance and efficiency of power devices could be further expanded when the conventional Si-based device reaches its physical limits. In order to further improve the efficiency and integration of power devices, active devices often need to be packed together with passive devices as power modules. In addition to discrete devices with a single chip, power modules usually contain multiple semiconductor dies that are connected to form a circuit of a certain structure, providing higher power density.

However, since the power module typically contains multi-layer structures with different materials such as semiconductor chip, metallic die-attachment layer, and power ceramic substrate, these materials are subject to severe shear stresses during the switching operation of power devices due to their coefficient of thermal expansion (CTE) mismatch[2], [3]. Moreover, the switching loss caused by non-ideal packaging structure or the unsatisfied heat-dissipation capacity of the packaging material can significantly increase the junction temperature of the power device during operation[4], [5], which may further accelerate device failure. These problems will result in a greater challenge to the reliability of the entire module. Over the decades, many efforts have been made to improve the heat dissipation capability and reliability of the power module, including the designs of packaging structures[4], [6]–[9] and the innovation of materials[10]–[14].

Among all packaging layers, the die-attach (DA) layer is the first layer directly connected to the power chip which affects the performance of the power module significantly. Also, since the power module has to operate under high temperatures and high power fluctuation conditions, the DA layer will not only transmit a huge amount of heat and electrical signals but also undergo large thermal stress brought by the power chip and the substrate. Therefore, an in-depth study of DA materials and processes is necessary for both the industry and the academy. In recent years, nano-silver sintering technology has become relatively mature to be studied and applied in the power module products[15]–[19]. A number of studies have been conducted to evaluate the performance of the silver-sintered power modules, such as thermal resistance[20]–[22], output/switching performance[21], [22], and thermomechanical reliability[23]–[25]. However, there are two significant limitations of sintered Ag joint, namely high material costs and electrochemical migration. As we have learned from the previous chapters, copper sintering technology is expected to replace sintered silver in power device packaging in recent years due to its excellent performance and cost advantages[26]–[31]. However, until now, the study of copper sintering was still in its infancy in the academy and in the industry. Therefore, in order to promote the industrial application of copper sintering technology, research on the suitability of the packaging process, output and switching performance, thermal performance, and reliability after use in power module packaging should be carried out as soon as possible.

In this chapter, the reliability of the Cu-sintered die-attach units and the static and dynamic characteristics of the Cu-sintered SiC MOSFET power modules were studied. The self-developed Cu paste and the pressure-assisted sintering die-attach process (at 250°C, with 20 MPa for 3 min) were adopted to conduct the study. As a benchmark, a silver-sintered SiC module was set in parallel. First of all, the effects of the 150°C/1000 hours high-temperature storage test and -40°C ~ 150°C /1000 cycles thermal cycling test on the shear strength, drain-source on-state resistance (R_{DSon}) and thermal resistance ($R_{th(jc)}$) reliability were investigated. Then, the output and switching performance of the Cu and Ag sintered SiC MOSFET power modules were evaluated. The experimental results indicated that both the mechanical and electrical performance of the Cu-sintered SiC module were at the same level as the Ag-sintered module. Considering the comprehensive cost-performance balance, the presented Cu sintering technology is quite promising for the wide-bandgap semiconductors power electronics packaging application.

5.2. METHODOLOGY

To verify the feasibility of Cu sintering technology in power electronics packaging, different forms of Cu sintered units and power modules were fabricated and tested in this chapter. They can be divided into three categories, as shown in Fig.5.1:

- Cu DA sandwich unit.
- SiC DA sandwich unit.
- SiC power module.

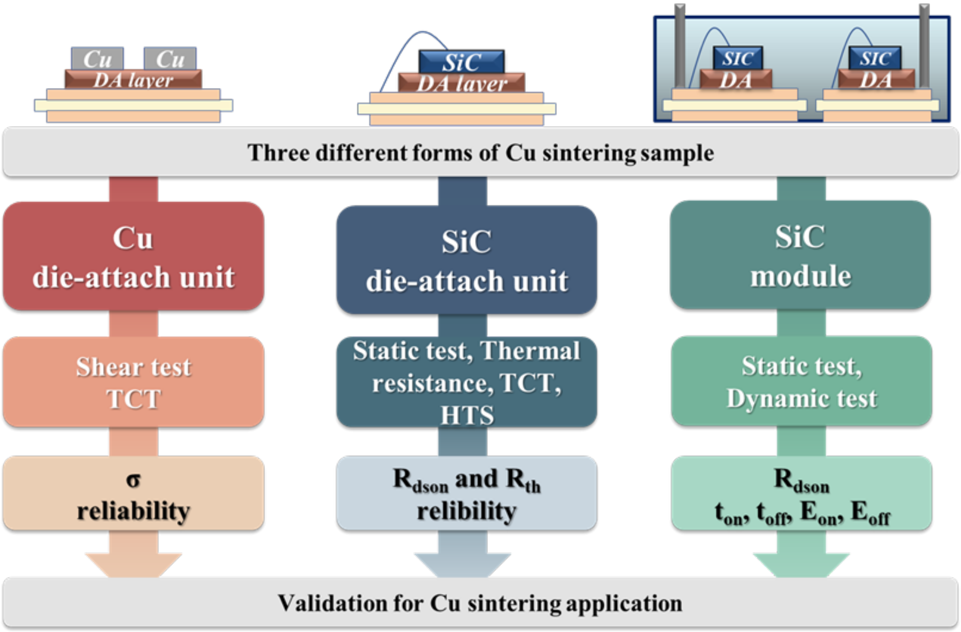
Cu
Cu
DA layer
SiC
DA layer
SIC
DA
SIC
DA
Three different forms of Cu sintering sample
Cu die-attach unit
SiC die-attach unit
SiC module
Shear test TCT
Static test, Thermal resistance, TCT, HTS
Static test, Dynamic test
σ reliability
R_{dson} and R_{th} relibility
R_{dson}
t_{on}, t_{off}, E_{on}, E_{off}
Validation for Cu sintering application

Figure 5.1: The different Cu sintered samples and the corresponding testing methods. From left to right: Cu DA units, SiC DA units, and SiC power modules.

5.2.1. Cu-Sintered Cu DA Units

First of all, the simplified Cu plate die-attached sandwich sample was adopted for the evaluation of shear strength and its reliability since the Ag-coated copper plate can withstand large shear forces to provide quantifiable strength results. To intimate the joining condition for the real chip, the Cu plates were cut to a similar size and coated with the same Ag metallization layer similar to the SiC MOSFET. To prepare the Cu DA units, the Cu paste developed in Chapter 3 was adopted in this study. Before the sintering process, the Cu paste was printed onto the AMB substrate (Ferrotec Corp., self-designed layout) with 13.5 mm × 13.5 mm × 100 μm pad size, as shown in Fig.5.2a. Then, the substrates were delivered into a vacuum oven for the drying process at 150°C for 5 min to remove the organic solvent. Also, the sintering process parameters (250°C, 3 min, 20 MPa) optimized in the previous chapters were used here. For each substrate, five Cu plates were sintered on it. Then the 1000-hour HTS test at 150°C and 1000-cycle TC test between -40°C~150°C were carried out. The temperature profile for the TC test is shown in Fig.5.2b. The dwell time for the peak temperature was 15 min, and the time span for one cycle was around 45 min. For each specific storage time and cycle, the shear strength was evaluated using XYZ Tech shear tester (Condor 150-3-HF), as shown in Fig.5.2c.

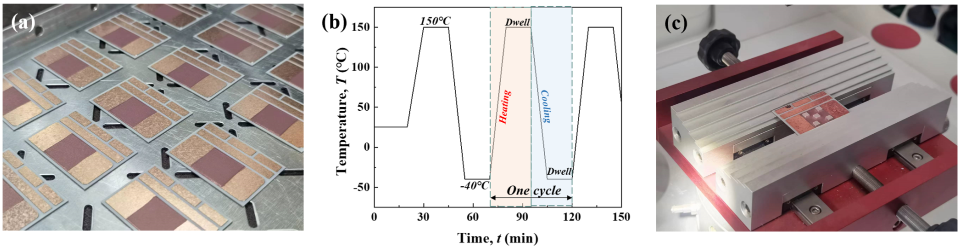

Figure 5.2: (a) The printed Cu paste on the AMB substrate. (b) The Cu sintered DA units under shear tests. (c) A schematic temperature profile for the thermal cycling test.

5.2.2. Cu-Sintered SiC DA Units

Then, the real SiC MOSFET (PNJ P3M12017BD 1200V, 107A, 7.26 mm × 4.26 mm, R_{DSon}=18$m\Omega$ as in TDS) and AMB substrate (Ferrotec Corp., self-designed layout) were adopted to fabricate the functional testing small units, in order to evaluate the effect of HTS and TCT reliability further on the functional performance of the Cu sintered DA technique. The SiC MOSFET was attached to the top surface of the AMB via the same optimized Cu sintering process (250°C, 3 min, 20 MPa.) in the N_2 atmosphere. For ensuring the current capacity, six Al bonding wires (diameter of 5 mils for each) were connected onto the source pad of the SiC chip, as in Fig.5.3. At least three pieces of die-attached units for each test group were used to calculate the results bias. The R_{DSon} and R_{th} results were evaluated for each specific storage time span and testing cycle. Combined with all results for the Cu DA units and SiC DA units, the mechanical and thermal reliability of the Cu sintered unit can be validated.

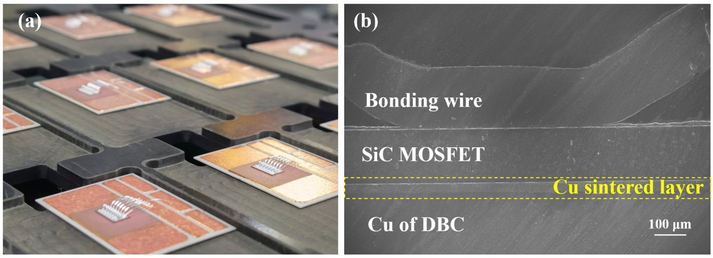

Figure 5.3: (a) The Cu sintered SiC DA units after the wire-bonding process. (b) The SEM cross-section image of the SiC unit.

5.2.3. CU-SINTERED SIC POWER MODULES

FINALLY, the Cu sintering technique was applied in SiC power modules to obtain its comprehensive property, as shown in Fig.5.4. In this study, a 1200V-100A single-chip module (SOT 227, industrial and EV OBC application) and a 1200V-200A half-bridge SiC module (62 mm, industrial and EV application) were fabricated respectively. The commercial SiC MOSFET (Rohm S4103UCCF 1200V, 95A, 4.81 mm × 4.80 mm, R_{DSon}=22 $m\Omega$ as shown in TDS) and AMB substrate (Ferrotec Corp.) were utilized for the module fabrication. The wire bonding, silicon-gel encapsulation and supersonic soldering of the busbar were conducted on the standardized packaging line. Static and dynamic tests were performed on these modules, with the Ag-sintered modules as a benchmark.

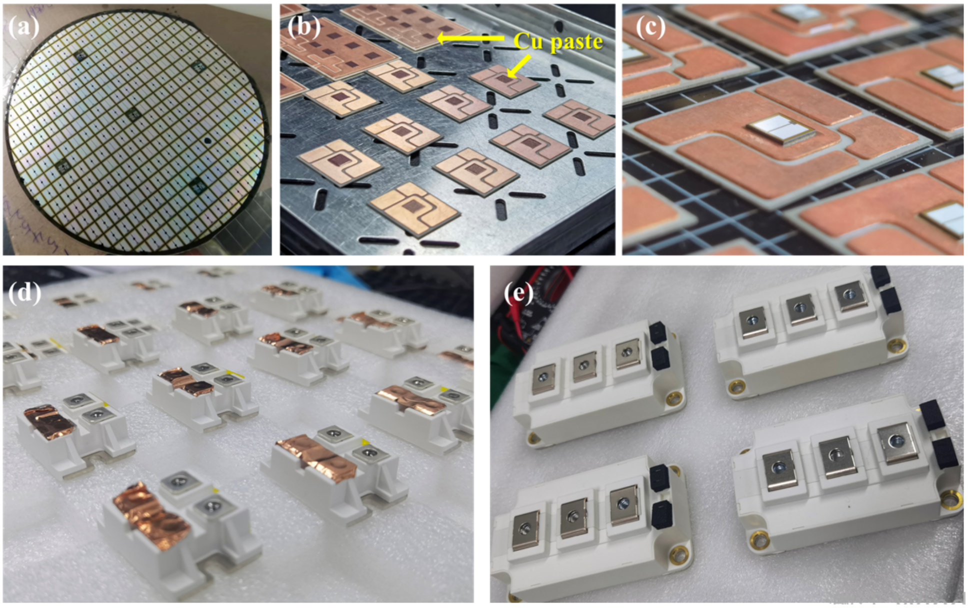

Figure 5.4: The fabrication process of Cu sintered SiC power modules: (a) SiC MOSFET wafer. The (b) as-printed and (c) as-sintered substrates. The Cu sintered (d) SOT227 modules and (e) 62 mm modules.

5.3. TCT AND HTS RELIABILITY OF SHEAR STRENGTH

First of all, the Cu sintered units (250°C, 3 min and 20 MPa) were adopted to study the evolution of the shear strength during the HTS (150°C) tests. The shear strength of the sample was evaluated for every 250 hours of the HTS, and the results are summarized in Fig.5.5a. The Cu sintered disc samples (250°C, 3 min and 20 MPa) were also prepared and sent to the same HTS test to be used as the supporting information for this study. It shows that the sample contained high shear strength, i.e., > 91.8 MPa, before the HTS test. Then the shear strength increases significantly with the holding time, up to over 120 MPa. Such phenomena have been reported in other studies[32], which was defined as the oxidation-enhancement property of Cu sinter joints. To verify the oxidation effect, the thermal conductivity of the disc samples was measured after different storage time, as shown in Fig.5.5b. Studies[33] have shown that the thermal conductivity of copper oxide is only one-tenth that of pure copper. Therefore, if a violent copper oxidation reaction occurs during the HTS test, the thermal conductivity will drop significantly. However, in our study, the difference in the thermal conductivity before (orange columns) and after (dark red columns) the HTS test was marginal for each disc sample, as shown in Fig.5.5b. We, therefore, speculate that oxidation of copper may have been present, but did not result in the production of significant amounts of copper oxides. A greater influence on the evolution of the properties may be the further sintering of the material under high-temperature preservation conditions.

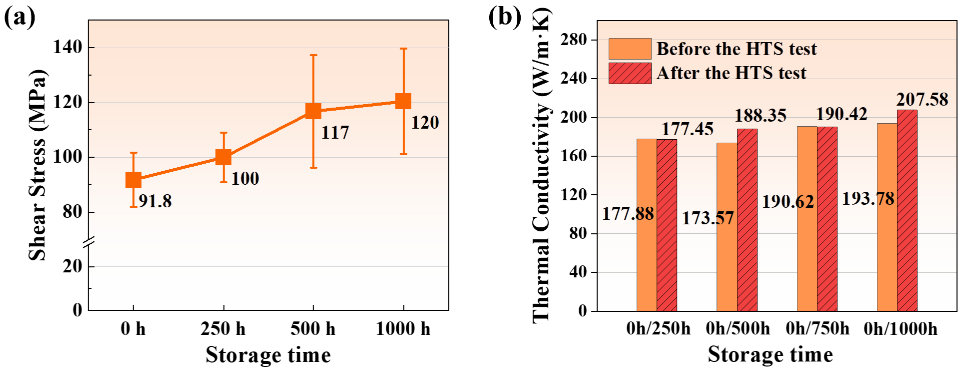

Figure 5.5: (a) The shear stress evolution and (b) the thermal conductivity evolution during the 1000-hours HTS test.

Fig.5.6 shows the SEM cross-section images of the Cu-sintered units after 0, 500 hours, and 1000 hours HTS test. A slight degree of pore growth as well as densification can be observed on the side where the sintered body and the sintered layer were connected to the substrate. This may be an effect similar to further sintering from long-term high-temperature preservation. Both of the possible reasons mentioned above could probably enhance the body density and the bonding strength of the Cu-sintered joint during the high-temperature storage process. The increased bond strength proves the better reliability of copper joints and validates their industrial potential and the longer-term experiments are still in progress.

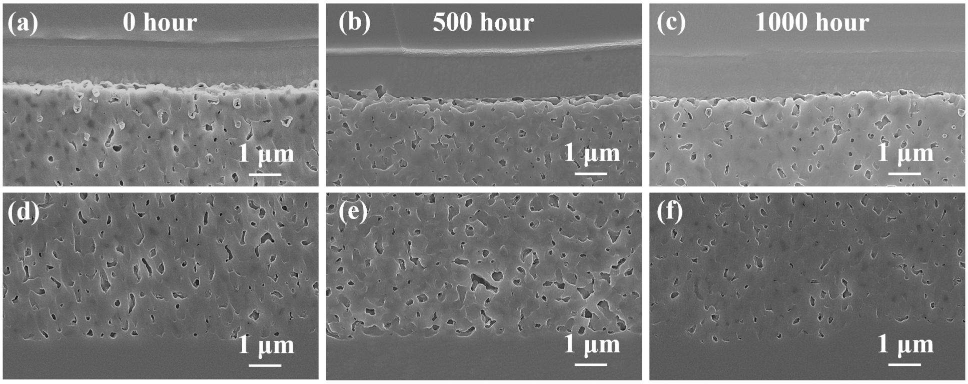

Figure 5.6: The SEM cross-section images of the Cu sintered units after 0 500 hours and 1000 hours HTS test. (a) to (c) are the region near the Cu plate. (d) to (f) are the region near the AMB substrate.

In addition, Fig.5.7 displays the shear stress evolution during the 1000-cycles TC test. It shows that after 250 cycles, the shear strength increased slightly to more than 100 MPa. After this time, the shear strength remained essentially constant. Fig.5.8 shows the SEM cross-section images of the corresponding samples after different cycles. No significant changes in microstructure nor interfacial delamination due to temperature cycling were found on the side where the copper plate was connected to the sintered layer (Fig.5.8a to d) and on the side where the sintered layer was connected to the substrate (Fig.5.8e to h). It seems that only some densification can be observed within the sintered body.

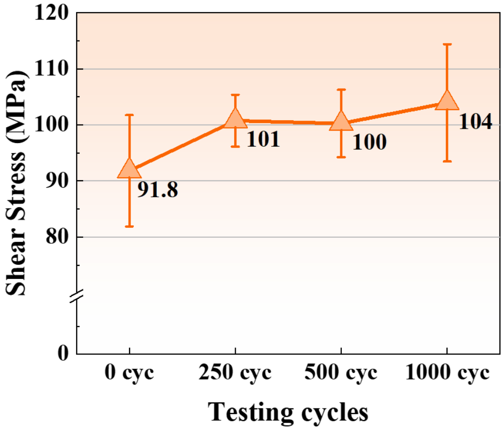

Figure 5.7: The shear stress evolution during the 1000-cycles TC test.

On the one hand, this slight improvement may come from further sintering during the TCT heating phase. On the other hand, the result also indicates that the residual stress due to the CTE mismatch of the multilayer material is smaller than the strength of the sintered copper itself and the joining between the sintered copper and the interface, and therefore it does not impair the connection effect. For SiC chips, the CTE of copper is closer to the value of the chip than Ag and SAC solders. Considering this perspective, sintered copper may be more suitable for the packaging of SiC chips.

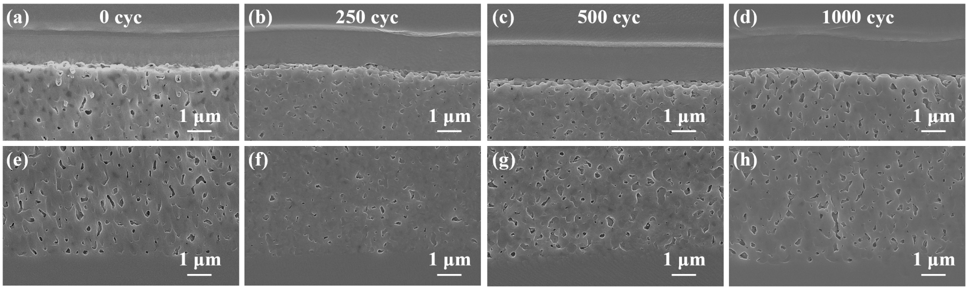

Figure 5.8: The SEM cross-section images of the Cu sintered units after 0, 250, 500 and 1000 TCT cycles. (a) to (d) are the region near the Cu plate. (e) to (h) are the region near the AMB substrate.

5.4. HTS Reliability of R_{DSon}

Then, the real SiC MOSFET (PNJ P3M12017BD 1200V,107A, 7.26 mm × 4.26 mm, R_{DSon} = 18 $m\Omega$ as in TDS) and AMB substrate (Ferrotec Corp., self-designed layout) were adopted to fabricate the functional small testing units for electrical and thermal performance evaluation. First, the 1000-hour HTS test at 150°C was carried out. For every 250 hours of storage time, the I–V characteristics curves and the R_{DSon} (drain-source on-state resistance) of tested SiC DA unit were measured at V_{GS} = 15 V and I_{DS} = 50 A. The R_{DSon} can be calculated by:

$$R_{DS(\mathrm{on})} = \frac{V_{DS}}{I_{DS}} \tag{5.1}$$

Fig.5.9a and b show the testing circuit for the output characteristic and R_{DSon} measurement setup of the unit. In this test, the TESEC, T5108-CU tester was adopted. The gate and source were externally connected by a gate driver.

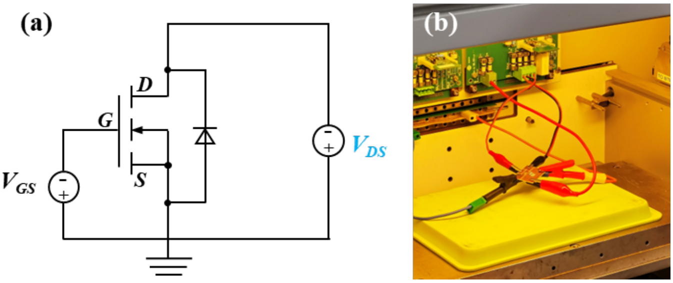

Figure 5.9: (a) The test circuit for I-V characteristics of the Cu sintered SiC units. (b) The Cu sintered SiC units under the output characteristics measurement.

Fig.5.10 shows results of the R_{DSon} from 0 hr to 1000 hr after the HTS test. Firstly, by observing the R_{DSon} data in the case of 0 hr, they are close to the typical value of the SiC bare die (18 $m\Omega$) in its datasheet, indicating low interfacial resistance and high electrical conductivity of the DA layer. It also suggests that the output properties of the device can be well protected under the present sintering process. Based on the analysis in the previous section, copper oxidation could be harmful to electrical resistivity and thermal conductivity. In the present study, the R_{DSon} values of the unit are always about 18.54 ± 0.24 $m\Omega$, and the changing rate is less than 1.3% during the 1000-hour storage at 150°C. The measured R_{DSon} results are consistent with the reliability results of the die-shear strength. It turns out that the problem of Cu oxidation in the high-temperature storage process will not significantly affect the key properties.

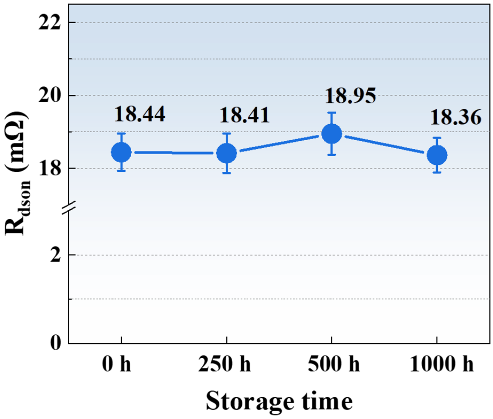

Figure 5.10: The R_{DSon} evolution during the 1000-hours HTS test.

5.5. TCT RELIABILITY OF R_{th}

THERMAL resistance (R_{th}) is an important parameter that can indicate the heat dissipation capability of the packaging structure. In order to improve the thermal performance of the power module, packaging materials containing lower thermal resistance values should be utilized. Two types of thermal resistance parameters are well used in the industry: steady-state thermal resistance (R_{th}) and transient thermal resistance (Z_{th}). The steady-state thermal resistance is tested in thermal equilibrium conditions, where the junction temperature is determined from a given ambient temperature and power loss. The transient thermal resistance is a function of time and is also related to the thermal capacity of the component. In order to obtain the specific contribution of each layer to the total thermal resistance, the transient dual interface test method involving the structure function is always applied. According to JEDEC-JESD51-1, the accurate measurement of thermal resistance is achieved by an electrical test method (ETM). It can be divided into three main steps.

Derivation of the TSP: To begin with, the so-called temperature sensitivity parameter (TSP, or K factor) has to be measured by using the body diode of the MOSFET. This

TSP is used to describe the relationship between the voltage and junction temperature of the device, which is necessary for the determination of the junction temperature in the following test. The testing circuit is shown in Fig.5.11a. When V_{GS} was shut down with – 10V, a small measurement current I_M (10 mA) was set on the device under testing (DUT) at different temperatures, and the V_{DS} was measured for each temperature. Then the slope of the temperature-voltage curve was calculated as TSP. The measured data for the TSP are shown in Fig.5.11b, and the fitted value of the TSP is 0.62718 mV/°C.

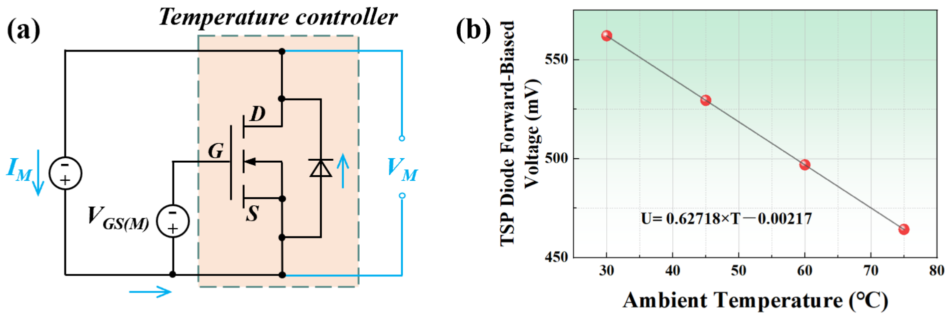

Figure 5.11: (a) The test circuit for the TSP (K factor) of the Cu sintered SiC units. (b) The obtained temperature-voltage relationship and the fitted TSP value.

Derivation of the structure function: The testing circuit for the structure function is shown in Fig.5.12a. A large heating current I_H (5 A) was set onto the DUT to heat up the device. The testing time was 100 s and the heating power was 30 W. When the temperature was stable, the I_H was switched to I_M again, and from which point the time and forward voltage data were recorded. Next, the forward voltage was converted to temperature by using the above-obtained TSP to acquire the transient cooling curve. Then, the transient cooling curve was calculated numerically to get the relationship between the thermal resistance and thermal capacitance, which is known as the cumulative structural function[34], as shown in Fig.5.12b.

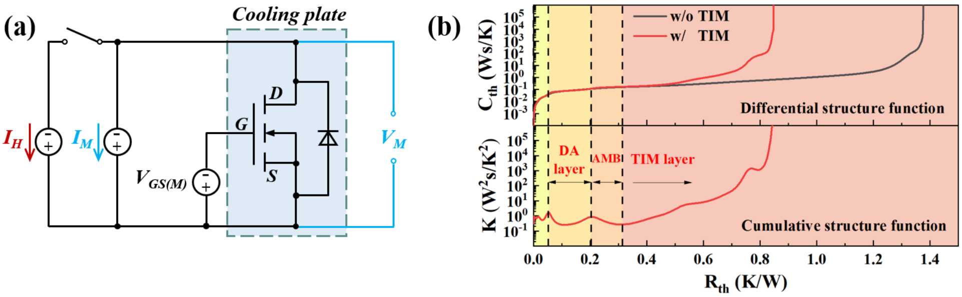

Figure 5.12: (a) The test circuit for the structure function. (b) The obtained differential (above) and cumulative (bottom) structure function curves.

Using dual interface method to extract thermal resistance values: Finally, the same test and calculation were conducted again to a testing unit with the thermal interface material (TIM) between the AMB bottom surface and cooling plate of the equipment. This step is necessary since the only difference between two samples was the TIM, and therefore, the location of the TIM on the curve can be easily determined by positioning the branch point of two overlapped structure function curves, as shown in Fig.5.12b. Before this point, it is the sum of R_{th} of the SiC testing unit, including SiC MOSFET, sintered die-attach layer and AMB substrate. Next, it is possible to distinguish the different substances under the chip by analyzing the slope change along the curve by calculating the differential structure function, since the thermal capacitance is constant along the vertical heat dissipation path, but the thermal resistance increases.

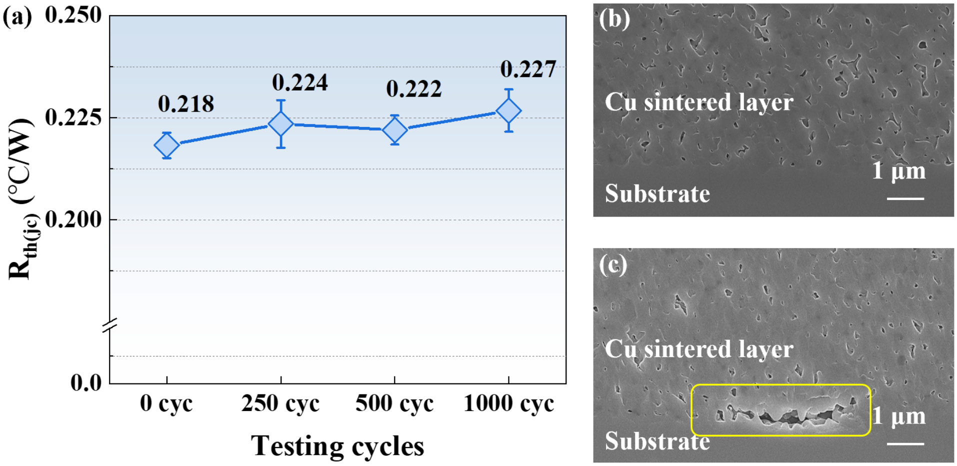

Figure 5.13: (a) The R_{th} evolution of the Cu sintered SiC DA units during the TC tests. The SEM cross-section images of the SiC DA units (b) before and (c) after 1000-cycles of TCT.

The calculated $R_{th(jc)}$ results were summarized in the Fig.5.13a. As can be seen from figure, the SiC MOSFET DA unit made by Cu sintering process has a very low thermal resistance value (0.218°C/W), which is similar to other sintered Ag and Cu samples tested in our previous work[35]. According to the study in Chapter 3, the sintered copper layer has a high thermal conductivity and the interface between the sintered layer and the die or the substrate is very dense, both of which contribute to its low thermal resistance. As the TCT experiment proceeds, a slight increase in the $R_{th(jc)}$ value of about 4% can be seen. In considerable agreement with the results of the shear strength reliability experiment and the thermal conductivity reliability experiment measured in the previous sections, the thermal stress due to TCT may not have caused destructive damage to the Cu sintered SiC unit nor significantly affected the thermal conductivity of the DA layer. However, unlike the shear experimental results, there is still a slight increase in the thermal resistance, which is probably due to a small region of failure at the interface of the sintered copper, as shown in Fig.5.13b and c. However, according to the module failure criterion (>20%), this small change is negligible for the whole device.

5.6. STATIC AND DYNAMIC TEST OF SIC POWER MODULES

FINALLY, in order to evaluate the adaptability of copper sintering technology to the module packaging process and the impact on the comprehensive performance of the module, we conducted static and dynamic tests on copper sintered SiC power modules under different application scenarios. In this part, a 1200V-100A single-chip module (SOT 227, for industrial and EV OBC application) and a 1200V-200A half-bridge SiC module (62 mm, for industrial and EV application) were fabricated respectively. The well-applied commercial SiC MOSFET (Rohm S4103UCCF 1200V, 95A, 4.81 mm × 4.80 mm, R_{DSon}=18-22 $m\Omega$ as shown in TDS) and AMB substrate (Ferrotec Corp.) were utilized for the module fabrication. The wire bonding, silicon-gel encapsulation and supersonic soldering of the busbar were conducted on the standardized packaging line. Static and dynamic tests were performed on these modules, with the Ag-sintered modules as a benchmark.

5.6.1. STATIC TEST (I-V CHARACTERISTICS) OF SIC POWER MODULES

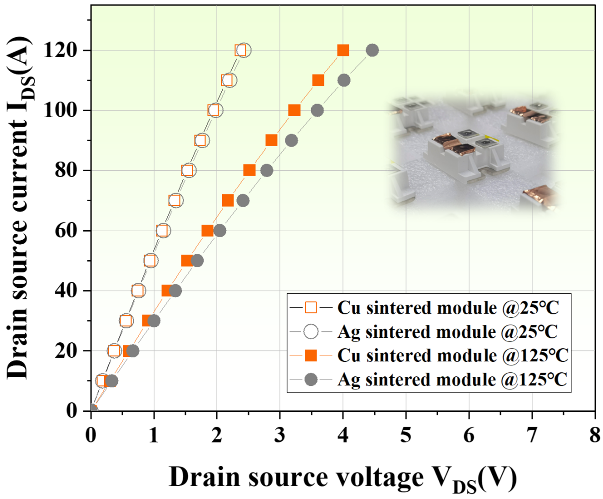

Figure 5.14: The I-V characteristics at 25°C and 125°C of the Cu and Ag sintered power module.

FIRST, the output characteristic of both Cu and Ag sintered SiC SOT227 modules were tested at 25°C and 125°C. The testing condition in both cases were V_{GS}= 18V and I_{DS}= 100A. Fig.5.14 presents the comparison of the I-V curves between the Cu (orange) and Ag (grey) sintered modules at room temperature and high temperature. The I-V curves for the copper sintered module are all slightly higher than that for the silver sintered module. Then we calculated the R_{DSon} for each module and found that the R_{DSon} value for Ag sintered module (19.42 $m\Omega$) is slightly higher than that for Cu sintered module (19.84 $m\Omega$). One possible reason for this is that the commercial sintered silver we used has silver particles that are micron-sized flakes, which might have a lower stacking density compared to our quasi-nanoparticle Cu material, resulting in higher resistance in the sintered layer. However, since the difference in absolute values between the two samples is small, it could also be just an experimental deviation. These results indicate that the Cu sintered module contained similar output performance as the Ag sintered one.

At 125°C, both I-V curves were shifted to the right compared with the curves at room temperature, and the R_{DSon} values increase to 32.3 $m\Omega$ and 35.92 $m\Omega$ for the Cu and Ag sintered modules. The absolute value of Cu and Ag sintered samples are summarized in Table5.1, which is consistent with the properties of the bare die, proving the excellent electrical conductivity that both sintered techniques could provide. (Note: The static drain-source on-state resistance of the bare chip is 22 $m\Omega$ and 33 $m\Omega$ at 25°C and 125 °C, respectively. Testing condition is V_{GS}= 18 V, I_{DS}= 36 A)

Table 5.1: The gate-source threshold voltage, drain-source on-state resistance values at 25°C and 125°C of Cu and Ag sintered modules.

Parameter	Condition	Cu sintered module	Ag sintered module	Unit
Gate-source threshold Voltage V_{GSth}	I_{DS}= 105mA, V_{DS}= V_{GS}, at T_{vj} = 25°C	4.4	4.3	V
Drain-source on-state resistance R_{DSon}	V_{GS}= 18V, I_{DS}= 100A, at T_{vj} = 25°C	19.43	19.84	$m\Omega$
Drain-source on-state resistance R_{DSon}	V_{GS}= 18V, I_{DS}= 100A, at T_{vj} = 125°C	33.54	35.92	$m\Omega$

5.6.2. Dynamic Test of SiC Power Modules

NEXT, a 1200V-200A half-bridge power module with four chips connected in parallel was fabricated for the double-pulse testing (DPT) [36]–[38], which can evaluate the circuit conversion characteristics and switching losses of the device. During the test, two pulse signals will be input to the gate driver of DUT. The first pulse is relatively wide (which means a longer time) to obtain a certain current. Then the sharp falling part of the first pulse is used for characterizing the turn-OFF parameters. Finally, the rising wave of the second pulse is used for the measurement of the turn-ON parameters.

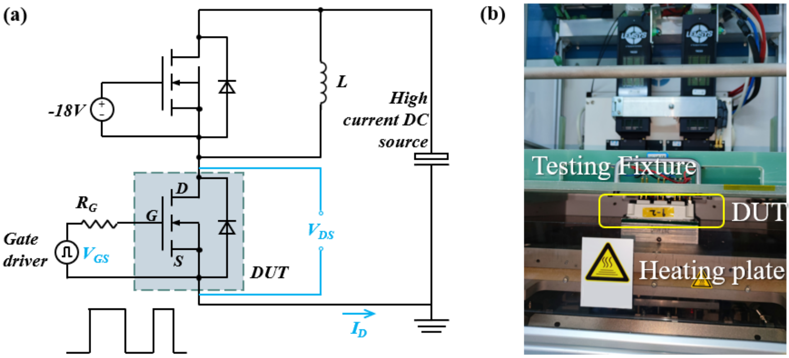

Figure 5.15: (a) The test circuit and (b) testing setup for the switching characteristics DPT.

Circuit and testing condition: Fig.5.15a shows the equivalent schematic circuit of the test setup, and Fig.5.15b is the photo for the DUT during the DPT. The DPT is usually done in the form of a half bridge. In this study, the high-side MOSFET was kept off by giving a -18V gate-source driving voltage. The low-side MOSFET was controlled by a double pulse gate signal. The LEMSYS tester (TRD 2015) was adopted to conduct the test. As shown in Fig.5.16 and Fig.5.17, the bus voltage V_{DS} and the collector current I_C were 300 V and 200 A. The gate resistance R_G, the external inductor L, and the gate voltage V_{GE} were 20 Ω, 1000 μH, and +18/0 V, respectively. The tests were conducted at both 25°C and 125°C. The time of the first and second pulse was 1 μs and 0.3 μs, respectively. The duration between the two pulses was 5 μs.

Results: First, as shown in Fig.5.16c and d, the blue and the red lines correspond to V_{DS} and I_C data, while the solid and dashed lines correspond to the results obtained at room temperature and 125°C. As shown in Fig.5.16c, when tested at 125°C, the V_{DS} and I_C waveforms show a left shift, indicating a shorter turn-ON delay time and a faster di/dt and dv/dt of the Cu sintered SiC module. It is reported that SiC MOSFET always turns on faster (higher current rise slope di/dt) at high temperature than at room temperature[39]. The underlying reason is that the threshold voltage of SiC devices has a negative temperature coefficient, and thus the turn-ON delay time of SiC MOSFET decreases with increasing temperature. Under the same driving conditions, the higher temperature leads to a faster turn-ON of the SiC MOSFET.

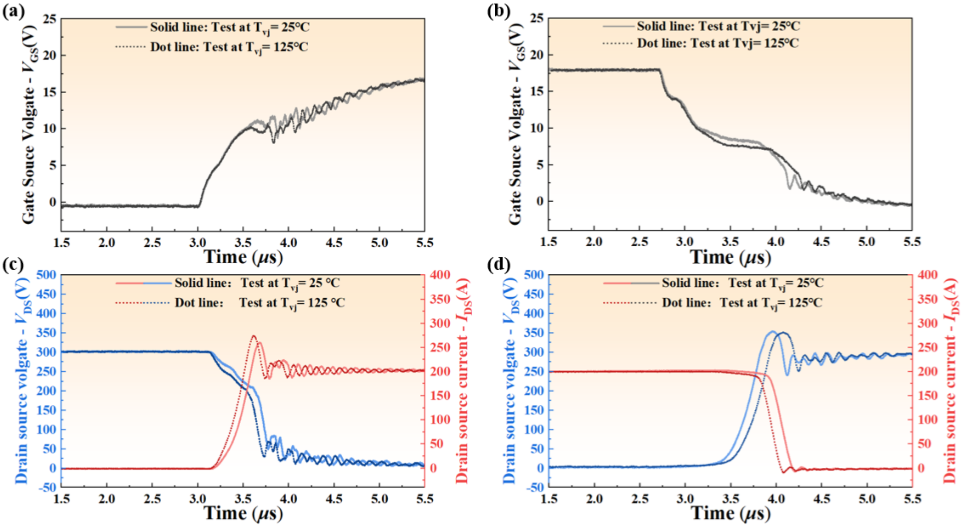

Figure 5.16: The switching waveforms of Cu sintered SiC modules.

In contrast, it can be found from Fig.5.16d that the turn-OFF waveforms for I_{DS} and V_{DS} at 125°C has a right shift compared with the results at room temperature. This is because the Mille Plateau voltage of the SiC device has a negative temperature coefficient, which eventually leads to a positive temperature coefficient characteristic of the turn-OFF delay time of the SiC MOSFET device[39]. As the temperature increases, the turn-OFF delay time increases with it.

Fig.5.17 shows the switching results of the Ag sintered SiC module containing a simi-

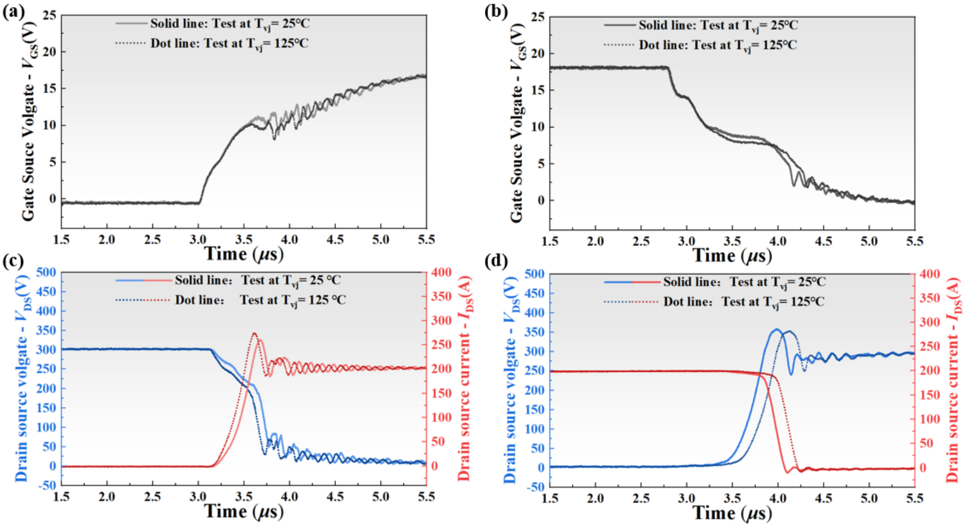

Figure 5.17: The switching waveforms of Ag sintered SiC modules.

lar trend as found in Cu sintered ones. Then we extracted the delay time and the switching loss of both modules, and summarized them into Fig.5.18. It reveals that the switching times and losses of both modules are similar with no significant level of difference. These results indicate that the changed switching time and losses should be related to the temperature-dependent characteristics of the SiC device, which are not affected by the die-attachment materials. In this way, it confirms that the copper sintering technique presented in this study is a promising solution for WBG power electronics packaging applications, considering the advantages of copper materials in terms of overall cost performance.

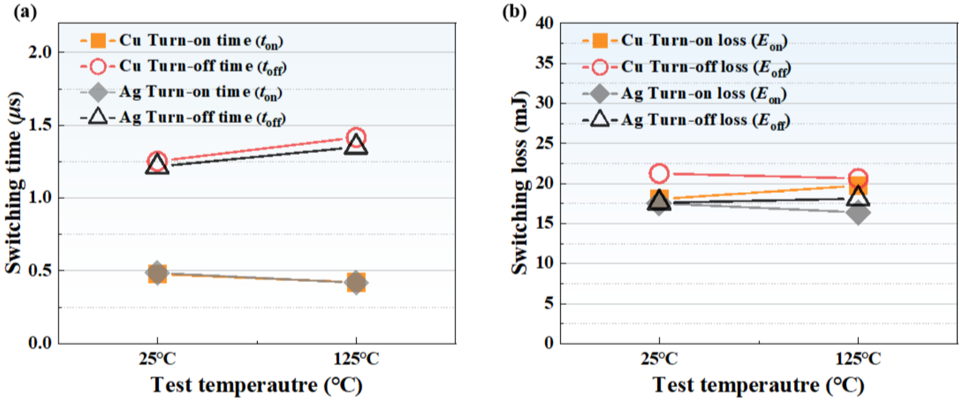

Figure 5.18: (a) The switching time and (b) switching loss of the Cu and Ag sintered SiC power modules.

5.7. CONCLUSION

IN this chapter, the reliability of the Cu-sintered die-attach samples and the output as well as switching characteristics of the Cu-sintered SiC MOSFET power modules were studied. The effects of the 150°C/1000 hours HTS test and -40°C ~ 150°C /1000 cycles TCT on the shear strength, R_{DSon} and $R_{th(jc)}$ reliability were investigated. In the beginning, the Cu sintered samples show high shear strength, low $R_{th(jc)}$ and low R_{DSon}, i.e., over 91.8 MPa, 0.218°C/W and 18.44$m\Omega$. As the reliability experiments progressed, these three key properties did not exhibit degradation. Then, the output and switching performance of the Cu and Ag sintered SiC MOSFET power modules were evaluated. The experimental results indicated that both of the output characteristics switching performance of Cu-sintered SiC module are at the same level as Ag-sintered module did and consistent with the standard commercial one. Considering the comprehensive cost-performance balance, it is believed that the presented Cu sintering technology is quite promising for WBG power electronics packaging application.

REFERENCES

[1] M. Rashid, *Power electronics handbook: devices, circuits, and applications, ed.* Academic Press. Elsevier, 2010.

[2] K. Dai and L. Shaw, “Thermal and stress modeling of multi-material laser processing”, *Acta Materialia*, vol. 49, no. 20, pp. 4171–4181, 2001.

[3] J. H. Pang, D. Chong, and T. Low, “Thermal cycling analysis of flip-chip solder joint reliability”, *IEEE Transactions on components and packaging technologies*, vol. 24, no. 4, pp. 705–712, 2001.

[4] C. Chen, F. Luo, and Y. Kang, “A review of sic power module packaging: Layout, material system and integration”, *CPSS Transactions on Power Electronics and Applications*, vol. 2, no. 3, pp. 170–186, 2017.

[5] L. Boettcher, S. Karaszkiewicz, D. Manessis, and A. Ostmann, “Development of embedded power electronics modules”, in *2012 4th Electronic System-Integration Technology Conference*, IEEE, 2012, pp. 1–6.

[6] Z. Chen, Y. Yao, D. Boroyevich, K. D. Ngo, P. Mattavelli, and K. Rajashekara, “A 1200-v, 60-a sic mosfet multichip phase-leg module for high-temperature, high-frequency applications”, *IEEE Transactions on Power Electronics*, vol. 29, no. 5, pp. 2307–2320, 2013.

[7] M. Wang, F. Luo, and L. Xu, “A double-end sourced multi-chip improved wire-bonded sic mosfet power module design”, in *2016 IEEE Applied Power Electronics Conference and Exposition (APEC)*, IEEE, 2016, pp. 709–714.

[8] R. Wang, D. Boroyevich, P. Ning, *et al.*, “A high-temperature sic three-phase ac-dc converter design for> 100/spl deg/c ambient temperature”, *IEEE Transactions on Power Electronics*, vol. 28, no. 1, pp. 555–572, 2012.

[9] C. Chen, Y. Chen, Y. Li, Z. Huang, T. Liu, and Y. Kang, "An sic-based half-bridge module with an improved hybrid packaging method for high power density applications", *IEEE Transactions on Industrial Electronics*, vol. 64, no. 11, pp. 8980–8991, 2017.

[10] A. Ostmann, "Evolution and future of embedding technology", in *IMAPS/NMI workshop" disappearing die–embed your chips*, 2016.

[11] K. Klein, E. Hoene, and K.-D. Lang, "Packages for fast switching hv gan power devices", in *PCIM Europe 2014; International Exhibition and Conference for Power Electronics, Intelligent Motion, Renewable Energy and Energy Management*, VDE, 2014, pp. 1–8.

[12] D. Xiang, L. Ran, P. Tavner, S. Yang, A. Bryant, and P. Mawby, "Condition monitoring power module solder fatigue using inverter harmonic identification", *IEEE Transactions on Power Electronics*, vol. 27, no. 1, pp. 235–247, 2011.

[13] S. W. Yoon, M. D. Glover, and K. Shiozaki, "Nickel–tin transient liquid phase bonding toward high-temperature operational power electronics in electrified vehicles", *IEEE Transactions on Power Electronics*, vol. 28, no. 5, pp. 2448–2456, 2012.

[14] G. Chen, L. Yu, Y.-H. Mei, X. Li, X. Chen, and G.-Q. Lu, "Reliability comparison between sac305 joint and sintered nanosilver joint at high temperatures for power electronic packaging", *Journal of Materials Processing Technology*, vol. 214, no. 9, pp. 1900–1908, 2014.

[15] K. Guth, N. Heuck, C. Stahlhut, *et al.*, "End-of-life investigation on the. xt interconnect technology", in *Proceedings of PCIM Europe 2015; International Exhibition and Conference for Power Electronics, Intelligent Motion, Renewable Energy and Energy Management*, VDE, 2015, pp. 1–8.

[16] K. Sugiura, T. Iwashige, K. Tsuruta, *et al.*, "Reliability evaluation of sic power module with sintered ag die attach and stress-relaxation structure", *IEEE Transactions on Components, Packaging and Manufacturing Technology*, vol. 9, no. 4, pp. 609–615, 2019.

[17] S. Jones-Jackson, R. Rodriguez, Y. Yang, L. Lopera, and A. Emadi, "Overview of current thermal management of automotive power electronics for traction purposes and future directions", *IEEE Transactions on Transportation Electrification*, vol. 8, no. 2, pp. 2412–2428, 2022.

[18] J. Reimers, L. Dorn-Gomba, C. Mak, and A. Emadi, "Automotive traction inverters: Current status and future trends", *IEEE Transactions on Vehicular Technology*, vol. 68, no. 4, pp. 3337–3350, 2019.

[19] L. M. Chew, W. Schmitt, J. Nachreiner, and D. Schnee, "Sintered ag joints on copper lead frame to220 by pressure sintering process with improved reliability and bonding strength", in *2017 21st European Microelectronics and Packaging Conference (EMPC) & Exhibition*, IEEE, 2017, pp. 1–5.

[20] Y. Mei, T. Wang, X. Cao, G. Chen, G.-Q. Lu, and X. Chen, "Transient thermal impedance measurements on low-temperature-sintered nanoscale silver joints", *Journal of electronic materials*, vol. 41, no. 11, pp. 3152–3160, 2012.

[21] M. Wang, Y. Mei, X. Li, R. Burgos, D. Boroyevich, and G.-Q. Lu, “Pressureless silver sintering on nickel for power module packaging”, *IEEE Transactions on Power Electronics*, vol. 34, no. 8, pp. 7121–7125, 2019.

[22] M. Wang, Y.-H. Mei, J. Jin, S. Chen, X. Li, and G.-Q. Lu, “Pressureless sintered-silver die-attach at 180° c for power electronics packaging”, *IEEE Transactions on Power Electronics*, vol. 36, no. 11, pp. 12 141–12 145, 2021.

[23] H. Zhang, Y. Liu, L. Wang, F. Sun, X. Fan, and G. Zhang, “Indentation hardness, plasticity and initial creep properties of nanosilver sintered joint”, *Results in Physics*, vol. 12, pp. 712–717, 2019.

[24] G. Chen, L. Yu, Y. Mei, X. Li, X. Chen, and G.-Q. Lu, “Uniaxial ratcheting behavior of sintered nanosilver joint for electronic packaging”, *Materials Science and Engineering: A*, vol. 591, pp. 121–129, 2014.

[25] X. Li, X. Chen, and G.-Q. Lu, “Isothermal low cycle fatigue behavior of nano-silver sintered single lap shear joint”, in *2012 13th International Conference on Electronic Packaging Technology & High Density Packaging*, IEEE, 2012, pp. 1209–1215.

[26] Y. Kobayashi, T. Shirochi, Y. Yasuda, and T. Morita, “Preparation of metallic copper nanoparticles in aqueous solution and their bonding properties”, *Solid state sciences*, vol. 13, no. 3, pp. 553–558, 2011.

[27] Y. Kamikoriyama, H. Imamura, A. Muramatsu, and K. Kanie, “Ambient aqueous-phase synthesis of copper nanoparticles and nanopastes with low-temperature sintering and ultra-high bonding abilities”, *Scientific reports*, vol. 9, no. 1, pp. 1–10, 2019.

[28] J. Yan, G. Zou, A. Wu, J. Ren, A. Hu, and Y. N. Zhou, “Polymer-protected cu-ag mixed nps for low-temperature bonding application”, *Journal of electronic materials*, vol. 41, no. 7, pp. 1886–1892, 2012.

[29] J. Xiong, Y. Wang, Q. Xue, and X. Wu, “Synthesis of highly stable dispersions of nanosized copper particles using l-ascorbic acid”, *Green Chemistry*, vol. 13, no. 4, pp. 900–904, 2011.

[30] M. Meddad, M. Badawi, M. Mazroui, *et al.*, “Sintering and deposition of homo- and heteronanoparticles of aluminum and nickel on aluminum (100) substrate”, *Chemical Physics*, vol. 541, p. 111 037, 2021.

[31] Y. Zhang, C. Cui, B. Yang, *et al.*, “Size-controllable copper nanomaterials for flexible printed electronics”, *Journal of Materials Science*, vol. 53, no. 18, pp. 12 988–12 995, 2018.

[32] Y. Gao, J. Jiu, C. Chen, K. Suganuma, R. Sun, and Z.-Q. Liu, “Oxidation-enhanced bonding strength of cu sinter joints during thermal storage test”, *Journal of Materials Science & Technology*, vol. 115, pp. 251–255, 2022.

[33] M. Liu, M. C. Lin, and C. Wang, “Enhancements of thermal conductivities with cu, cuo, and carbon nanotube nanofluids and application of mwnt/water nanofluid on a water chiller system”, *Nanoscale research letters*, vol. 6, no. 1, pp. 1–13, 2011.

[34] V. I. Smirnov, V. A. Sergeev, A. Gavrikov, and A. Shorin, “Modulation method for measuring thermal impedance components of semiconductor devices”, *Microelectronics Reliability*, vol. 80, pp. 205–212, 2018.

[35] R. Sattari, D. Hu, X. Liu, H. van Zeijl, S. Vollebregt, and G. Zhang, “Transient thermal measurement on nano-metallic sintered die-attach joints using a thermal test chip”, *Applied Thermal Engineering*, p. 119 503, 2022.

[36] F. Hou, W. Wang, R. Ma, *et al.*, “Fan-out panel-level pcb-embedded sic power mosfets packaging”, *IEEE Journal of Emerging and Selected Topics in Power Electronics*, vol. 8, no. 1, pp. 367–380, 2019.

[37] Z. Zhang, F. Wang, L. M. Tolbert, B. J. Blalock, and D. J. Costinett, “Evaluation of switching performance of sic devices in pwm inverter-fed induction motor drives”, *IEEE Transactions on Power Electronics*, vol. 30, no. 10, pp. 5701–5711, 2014.

[38] Z. Chen, Y. Yao, D. Boroyevich, K. D. Ngo, P. Mattavelli, and K. Rajashekara, “A 1200-v, 60-a sic mosfet multichip phase-leg module for high-temperature, high-frequency applications”, *IEEE Transactions on Power Electronics*, vol. 29, no. 5, pp. 2307–2320, 2013.

[39] Z. Chen, Y. Yao, M. Danilovic, and D. Boroyevich, “Performance evaluation of sic power mosfets for high-temperature applications”, in *2012 15th International Power Electronics and Motion Control Conference (EPE/PEMC)*, IEEE, 2012, DS1a–8.

6

CONCLUSIONS AND RECOMMENDATIONS

6.1. CONCLUSIONS

IN this dissertation, a systematic study of the copper sintering technique regarding the materials, process, simulation, applications and testing was conducted by applying the self-developed copper sintering paste. The key developments and findings are summarized here.

Sintering mechanism of Cu particles on the power substrate: The coalescence kinetics and microstructure evolution of Cu NPs sintering between two substrates at low temperature were investigated by MD simulation. The crystal structure, atomic diffusion, dislocation behavior and porous defects were studied by using OVITO tools, MSD curves, CNA and DXA analysis. It was found that the dominant sintering mechanisms for the particles without applied pressure at low temperature was mainly surface diffusion. However, when the pressure effect of the upper substrate on the particles was introduced, the dominant sintering mechanism of the particles changes to plastic flow induced by dislocation production and motion in the particles. In addition, the spontaneous rotation of particles occurred during the coalescence to eliminate the inter-particle lattice mismatch, while the passive rotation behavior of the L3 particles also occurred due to the pinning effect of the substrate. Apart from that, the pinning effect also created giant pores between particles and substrates. Some of these pores can be filled via both plastic deformation and surface diffusion of atoms for the smaller particles. Finally, to investigate the size effect on the sintering kinetics, the atomic motion and microstructrual evolution of 3 nm, 4 nm and 5 nm models were compared. It was found that the models of smaller-size particles typically contained higher shrinkage ratios, larger sintering necks and smaller pores. More severe atomic motion, and more drastic crystal structure transitions at each stage was found in smaller size particles. The research results show that the sintering densification and pores structure can be improved by using the applied pressure in the sintering process. Particle sintering progress is greatly accelerated by enhancing the plastic flow mechanism. However, attention should also be paid to the problems such as rotational residual stresses brought about by the pinning effect of the substrate, which may require further heat treatment to eliminate.

Die-attachment process and joining strength: A self-developed Cu paste was fabricated with predefined printing, drying and sintering workability. A reductive pretreatment was conducted in advance to the raw Cu particles to remove the original oxidation. Laser flash measurements, four-probe methods, and die shear tests were performed to obtain the thermal, electrical, and bonding properties of Cu sintered die attachment techniques. The effects of temperature, pressure, and time on the integrated properties and the microstructural evolution of the sinter joints are then investigated. With only 1 min of the sintering process, the thermal (5.82 W/m·K) and electrical conductivity ($0.003/(\mu\Omega\cdot\text{cm})$) of the sample is extremely small and cannot satisfy the semiconductor packaging requirements. Increasing the sintering time to 4 minutes can effectively improve the conductivity characteristics to 231.15 W/m·K and $0.255/(\mu\Omega\cdot\text{cm})$. There is a similar trend for the effect of temperature that both properties were improved from 126.53 W/m·K to 272.87 W/m·K, and from $0.124/(\mu\Omega\cdot\text{cm})$ to $0.282/(\mu\Omega\cdot\text{cm})$ by increasing the sintering temperature from 210°C to 270°C. Then, in order to evaluate the impact of the Cu sintering process parameters on joining performance and microstructure evolution of the die-attach samples, the shear test was conducted with various sintering temperature, pressure and time. It was also found that sintering temperature between 210°C and 230°C, or assisted pressure less than 10 MPa could provide bonding strength of around 30 MPa. Such low strength is due to both the partially burnt out of organics and incomplete Cu particles sintering. By increasing pressure to 20 MPa and 30 MPa, it shows the enhanced die shear strength of 100.1 MPa and 116 MPa, accomplished with a sintering temperature of 250°C for 3 min. When increased temperature to 270°C, the shear strength was extremely enhanced to over 120 MPa. Moreover, time can insignificantly affect the microstructure and bonding strength in less than 4 min. Material microstructural characterization demonstrates that high bonding is coming from the positive effect of pressure and temperature on promoting the necking growth, sintering networking formation, pores isolation and brittle-ductile fracture transition. Considering the small improvement effect by further increasing of temperature and pressure, 250°C/3 min/20 MPa process recipe is well recommended for the application.

Sintered material mechanical reliability: Key mechanical properties such as indentation hardness, elastic modulus and creep rate of Cu sintered samples are evaluated separately to verify the feasibility of this technique for application in die-attachment processes. First of all, the peak load (from 10mN to 150 mN) and loading rate (from 0.1 mN/s to 1.5 mN/s) effect on the indentation hardness and elastic modulus were investigated. The tested displacement-load curves were used to analyze the elastic-plastic properties and compute these key mechanical parameters. The ISE is found to be evident when the indentation depth is below 500 nm and the corresponding peak load is less than 10 mN. But after 70 mN of peak load (1500 nm of maximum depth), the changing trend is no more evident. Loading rate has similar effect on these parameters. As the it increases from 0.1 mN/s to 0.9 mN/s, both the indentation hardness and the elastic modulus gradually increase as well. But from 0.9 mN/s, the two properties start to became stable at around 1.59 ± 0.154 GPa and 99.5 ± 0.86 GPa. The potential causes are mainly work hardening effect, pores densification, and pile-up phenomena during the indentation test. Therefore, to ensure stable experimental results, an indentation depth of more than 1500 nm and a loading rate over 0.9 mN/s are necessary. By using the stable testing parameters, the constitutive models (yield stress, strain hardening exponent factors) for samples sintered via different applied pressure were obtained, which can be used to describe the room-temperature mechanical properties of the Cu sintered joint. Next, the effects of temperature ranging from 150°C to 240°C on the indentation hardness and elastic modulus were investigated. The temperature dependence of both parameters was fitted to account for this effect. In addition, the creep behavior including the steady-state creep strain rate has been studied and compared for samples sintered with different applied pressures. Higher temperatures were found to result in more severe creep deformations. However, higher sintering pressure can effectively improve the creep resistance against plastic deformation. But the increasing effect comes to marginal over 20 MPa, which provides a hint to the selection of the sintering process parameters in practical.

Application in SiC module packaging and functional testing: Pressure-assisted Cu sintering die-attachment process (250°C/3 min/20 MPa) was adopted to prepare Cu and SiC die-attach units and several SiC power modules. First of all, the effects of the 150°C/1000 hours high temperature storage test and -40°C ~ 150°C /1000 cycles thermal cycling test on the shear strength, drain-source on-state resistance (R_{DSon}) and thermal resistance ($R_{th(jc)}$) reliability were investigated. It was found that the sample had an initial shear strength of 91.8 MPa before the reliability test. Then the shear strength increased significantly with the storage time during the HTS test, up to over 120 MPa. The oxidation-enhancement effect as well as the high-temperature densification process may enhance the body density and the bonding strength of the Cu sintering joint during the high-temperature storage process. Furthermore, during the TC test, the shear strength increased slightly to more than 100 MPa and remained essentially constant till 1000 cycles. The SEM cross-section images prove that no significant changes in microstructure nor interfacial delamination due to temperature cycling were found on the side where the copper plate was connected to the sintered layer and on the side where the sintered layer was connected to the substrate. Then, the R_{DSon} and $R_{th(jc)}$ reliability was investigated through HTS test and TC test respectively. Firstly, The R_{DSon} data in the case of 0 hr is found to be close to the typical value of the SiC bare die (18 $m\Omega$) in its datasheet, indicating low interfacial resistance and high electrical conductivity of the DA layer. During the 1000-hour storage at 150°C, the R_{DSon} values of the unit are always about 18.54 ± 0.24 $m\Omega$. It turns out that the problem of particle oxidation is not significant in the high-temperature storage process. Then the $R_{th(jc)}$ of Cu sintered layer was obtained by conducting the dual-interface method. It is found that the SiC MOSFET DA unit made by Cu sintering process has a very low thermal resistance value (0.218°C/W), which is similar to other sintered Ag and Cu samples tested in our previous work. As the TC experiment proceeds, a slight increase in the R_{th} value of about 4% can be seen, which may be due to a small region of failure at the interface of the sintered copper. However, according to the module failure criterion (>20%), this small change is negligible for the whole device. Finally, the static and dynamic tests of Cu-sintered SiC module were conducted on the Cu sintered SiC modules. As a benchmark, a same SiC module that was die-attached by Ag sintering process was set in parallel. The experimental results indicated that both of the output characteristics and switching performance of Cu-sintered SiC module are at the same level as Ag-sintered module did and consistent with the standard commercial one. Considering the comprehensive cost-performance balance, the presented Cu sintering technology is quite promising for WBG power electronics packaging application.

6.2. RECOMMENDATIONS IN FUTURE WORKS

THE present project has systematically studied the material properties, sintering mechanisms and application feasibilities of the Cu sintering technique. However, due to the limited experimental and computational conditions, there are still some work that should be continued in the future:

Regarding the sintering mechanism, the present work mainly focuses on the study of the interaction between the substrate and Cu NPs using the MD method. In the future, the simulation results at different scales should be obtained by combining the first nature principle as well as finite element simulation techniques to verify each other. In addition, to provide more evidence for the simulation results, in-situ characterization methods can be used to observe the atomic behavior of the nanoparticle and substrate surfaces during realistic sintering processes.

For the study of mechanical reliability, the constitutional models of Cu-sintered materials was obtained by nanoindentation experiments. If available, these parameters can be used to construct a finite element simulation model to implement a reliability study of the thermomechanical properties of a Cu-sintered joint under different conditions.

For the die-attachment process, the current work studied the bonding performance on bare Cu substrate. In the industry, Ag, Au and Ni are also used in different scenarios, therefore, it is important to evaluate the joining performance of Cu sintering techniques on these surfaces. Atomic diffusion can be studied by experiments and simulations. Moreover, additional sizes of Cu nanoparticles may be applied to further lower down the sintering temperature. However, the comprehensive improper coalescence, oxidation, and low workability brought by smaller NPs should be considered.

Finally, for reliability and application, longer time and extra cycles of thermal reliability test should be conducted. Moreover, functional SiC, Si and GaN die can be used as the chips to investigate the CTE mismatch effect on the delamination. Correspondingly, in-situ measurement methods can be developed for fast reliability testing on functional chips.

A

SUPPORTING INFORMATION CHAPTER 2

INITIAL VELOCITY OF THE UPPER SUBSTRATE

The initial velocity (1Å/ps, -z direction) was only set to the to the atoms in the first two layers of the upper substrate instead of the whole substrate. There were around 30 layers of atoms in the upper substrate, and according to the *Law of Conservation of Kinetic Energy:*

$$m_i \cdot v_i = m_{sub} \cdot v_{sub} \tag{A.1}$$

$$v_{sub} = \frac{1}{15} v_i = \frac{1}{15} (\text{Å}/ps) \approx 6.7 (\text{m/s}) \tag{A.2}$$

where m_i and v_i represent the mass and initial velocity of the preset atoms group in the upper substrate. m_{sub} and v_{sub} represent the mass and final velocity of the upper substrate. The purpose of this setting is first to imitate the downwards movement tendency caused by the gravity of upper substrate, and also to accelerate the simulation process. This small initial velocity to the upper substrate was given only at the beginning of the simulation. It is worth noting that only the initial velocity less than 2Å/ps (13.3 m/s for substrate) would be considered since this is a rational value that the substrate is able to obtain after 1~2 s by gravity. Additionally, high initial velocity (for example over 5 Å/ps) may cause huge equivalent pressure to the sintering layer which would change the sintering mechanism of the whole system. This equivalent pressure should be avoided within the scope of current research.

To further verify how the presetting velocity value would affect the results, the comparative computational research was conducted. Four typical values were chosen (0.5, 1, 1.5, 2 Å/ps) for this study. Specifically, the effect of initial velocity on the Shrinkage Ratio (SR, ζ_x) and Coalescence Index (CI, ζ_z), crystal structures and dislocation distribution were studied. This simulation study was conducted by using the 3 nm model (3 × 3 × 1 array) at 300 K with 300 ps.

First it is found that higher initial velocity can increase slope of the ζ_z curve and help to reach the steady state earlier. However, the values of the steady state for all four models are similar with only ±1.5% difference. This indicates that the selected initial velocity values would not influence the final vertical shrinkage effect and macroscopic density of sintered layer.

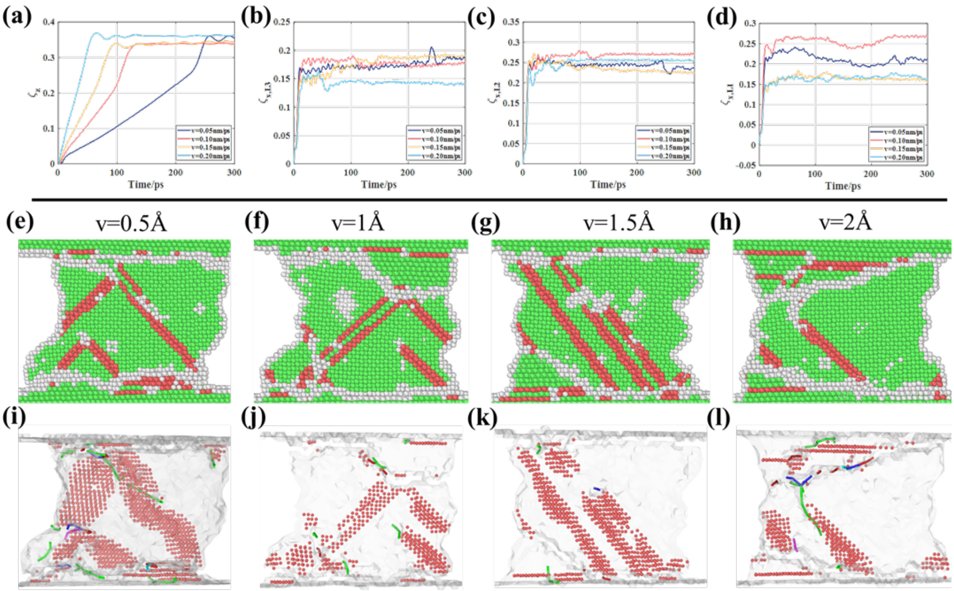

Figure A.1: Macro- and microstructural evolution during 300 ps sintering. (a) The vertical shrinkage (CI, ζ_z). (b) to (d) The horizontal shrinkage of L3, L2 and L1 (SR, ζ_x). (e) to (l) The Cross-section and dislocation distribution snapshots of models with 0.5, 1, 1.5, 2 Å/ps initial velocity respectively.

Secondly, the results of $\zeta_{(x,L3)}$ and $\zeta_{(x,L2)}$, show that the velocity has less effect on the initial stage (before 10 ps) of L3 and L2 horizontal shrinkage. This is reasonable because the substrate first touched with L1. When entering steady stage (after 10 ps), the shrinkage ratio value for 0.5~1.5 Å/ps models were within ±1% difference, whereas the value for 2 Å/ps model was significantly smaller. This means horizontal shrinkage of L1 for 2 Å/ps model was weaker than the other models. By observing the atomic configuration in different time period, it is found that for 2 Å/ps model, the upper substrate touched with L1 particles earlier. Contacting at too-early stage caused the formation of the interlocking between L1 and substrate earlier, which blocked the horizontal movement of the L1 particles.

From the crystal structure distribution and dislocation distribution figures we found that the FCC, HCP and amorphous crystal structure of each model have no big difference as well. All models contain large amount of HCP in the final stage, which is similar as the results in the main text. Moreover, it is found that higher velocity caused more severe realignment at the interface region as shown in the figures. Such structure is also found in the main text. In summary, within 0.5~2 Å/ps, there is no significant difference for the results. Higher or lower initial velocity would not be suitable for this work.

Comparison of different simulation models

In this study, a special sandwiched-like model containing two substrates and multiple particles in between was applied. Previous studies have dealt with typical models which applied different amounts of NPs and substrate as shown in the following table[1]–[15]. It turns out that in order to study the interaction between substrate and NPs in the practical die-attachment application, the model of double substrates with multiple NPs is a reasonable selection.

Table. A1 Summary of simulation models on study of NPs coalescence

Nr. of Substrate	Nr. of NPs	Model	Previous research topic and Ref.	Present study
None	Double	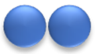	· Study of the general sintering behavior and mechanism between two or more NPs [1–5] · Effects of specific structures on the coalescence process [3–5]	· Contribution of substrate on the sintering process
None	Multiple	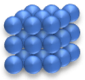		
Single	Single	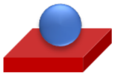	· Study of the interaction between single NP with substrate, misorientation effects, sintering of nanoflake (small)-NP, wetting and diffusion behavior [6–8]	· Additional interaction between different NPs and substrates simultaneously
Single	Multiple	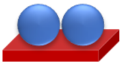	· Study of coalescence behaviors of NPs-substrate system and the homo- or heterogeneous effects [9–11]	· Effects of NPs and substrate from different direction.
Double	Single	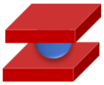	· Study of transient liquid phase sintering [12]	· Additional interaction between multiple NPs and substrates simultaneously. · Observation on the evolution of different type of pores.
Double	Double	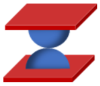	· Sintering process with the assisted-pressure and Stress-dislocation interaction during compression [13,14]	· More study on size and temperature effect. · Observation on the evolution of different type of pores.
Double	Multiple	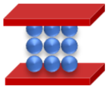	· The diffusion between NP and substrate [15]	· More study on size and temperature effect. · Observation on the evolution of different type of pores.

REFERENCES

[1] Z. Liu, Q. Cheng, Y. Wang, Y. Li, and J. Zhang, "Sintering neck growth mechanism of fe nanoparticles: A molecular dynamics simulation", *Chemical Engineering Science*, vol. 218, p. 115 583, 2020.

[2] M. Meddad, M. Badawi, M. Mazroui, *et al.*, "Sintering and deposition of homo- and heteronanoparticles of aluminum and nickel on aluminum (100) substrate", *Chemical Physics*, vol. 541, p. 111 037, 2021.

[3] X. Ren, X. Li, C. Huang, H. Yin, and F. Wei, "Molecular dynamics simulation of thermal welding morphology of ag/au/cu nanoparticles distributed on si substrates", *Ferroelectrics*, vol. 564, no. 1, pp. 19–27, 2020.

[4] J. Wang, S. Shin, A. Hu, and J. K. Wilt, "Diffusion kinetics of transient liquid phase bonding of ni-based superalloy with ni nanoparticles: A molecular dynamics perspective", *Computational Materials Science*, vol. 152, pp. 228–235, 2018.

[5] D. Hu, Z. Cui, J. Fan, X. Fan, and G. Zhang, "Thermal kinetic and mechanical behaviors of pressure-assisted cu nanoparticles sintering: A molecular dynamics study", *Results in Physics*, vol. 19, p. 103 486, 2020.

[6] J. Wang, S. Shin, A. Hu, and J. K. Wilt, "Diffusion kinetics of transient liquid phase bonding of ni-based superalloy with ni nanoparticles: A molecular dynamics perspective", *Computational Materials Science*, vol. 152, pp. 228–235, 2018.

[7] D. Ishikawa, B. N. An, M. Mail, *et al.*, "Bonding strength of cu sinter die-bonding paste on ni, cu, ag, and au surfaces under pressureless bonding process", *Transactions of The Japan Institute of Electronics Packaging*, vol. 13, E19–017, 2020.

[8] A. Malti, A. Kardani, and A. Montazeri, "An insight into the temperature-dependent sintering mechanisms of metal nanoparticles through md-based microstructural analysis", *Powder Technology*, vol. 386, pp. 30–39, 2021.

[9] S. Li, Y. Liu, F. Sun, and H. Fang, "Multi-particle molecular dynamics simulation: Shell thickness effects on sintering process of cu-ag core-shell nanoparticles", *Journal of Nanoparticle Research*, vol. 23, no. 1, pp. 1–14, 2021.

[10] J. Wang and S. Shin, "Sintering of multiple cu–ag core–shell nanoparticles and properties of nanoparticle-sintered structures", *Rsc Advances*, vol. 7, no. 35, pp. 21 607–21 617, 2017.

[11] S. Yang, W. Kim, and M. Cho, "Molecular dynamics study on the coalescence kinetics and mechanical behavior of nanoporous structure formed by thermal sintering of cu nanoparticles", *International Journal of Engineering Science*, vol. 123, pp. 1–19, 2018.

[12] L. Zhan, X. Zhu, X. Qin, M. Wu, and X. Li, "Sintering mechanism of copper nanoparticle sphere-plate of crystal misalignment: A study by molecular dynamics simulations", *Journal of Materials Research and Technology*, vol. 12, pp. 668–678, 2021.

[13] S. Li, Y. Liu, H. Ye, *et al.*, "Sintering mechanism of ag nanoparticle-nanoflake: A molecular dynamics simulation", *journal of materials research and technology*, vol. 16, pp. 640–655, 2022.

[14] V. M. Samsonov, A. G. Bembel, I. V. Popov, S. A. Vasilyev, and I. V. Talyzin, “Solid-state wetting at the nanoscale: Molecular dynamics and surface diffusion approach”, *Surface Innovations*, vol. 5, no. 3, pp. 161–169, 2017.

[15] H. Dong, K.-S. Moon, and C. Wong, “Molecular dynamics study on the coalescence of cu nanoparticles and their deposition on the cu substrate”, *Journal of electronic materials*, vol. 33, no. 11, pp. 1326–1330, 2004.

B

SUPPORTING INFORMATION CHAPTER 3

THE REDUCTIVE TREATMENT RESULTS

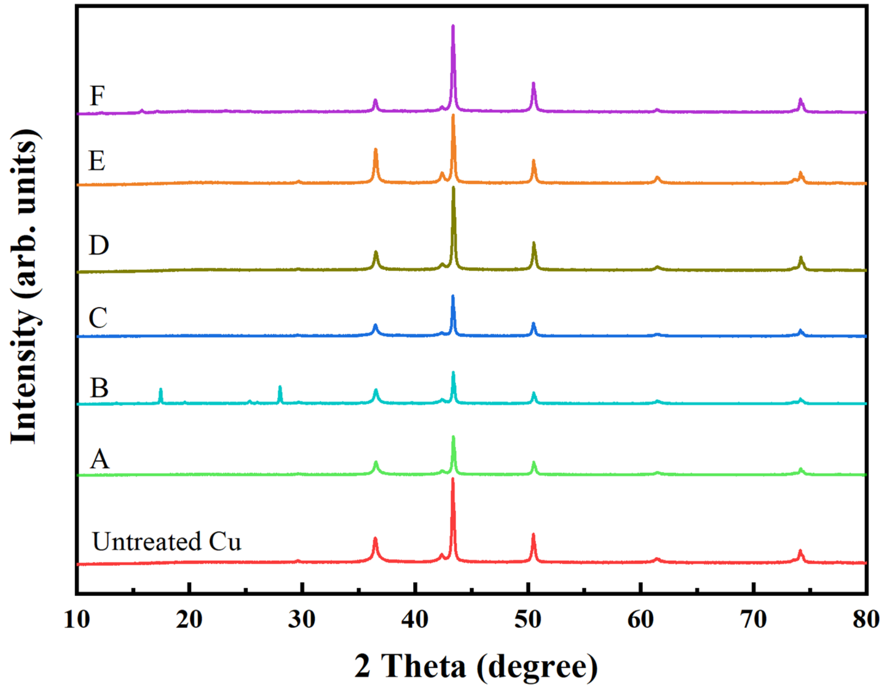

Figure B.1: XRD results for the original Cu NPs, and the Cu NPs treated by different reductive agents.

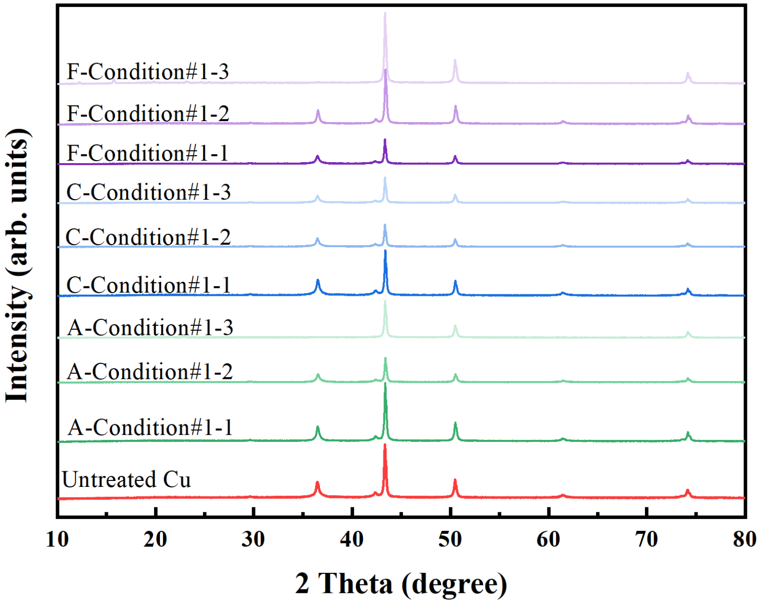

Figure B.2: XRD results for the Cu NPs treated by reductive agents A, C and F with treating condition 1-1, 1-2 and 1-3.

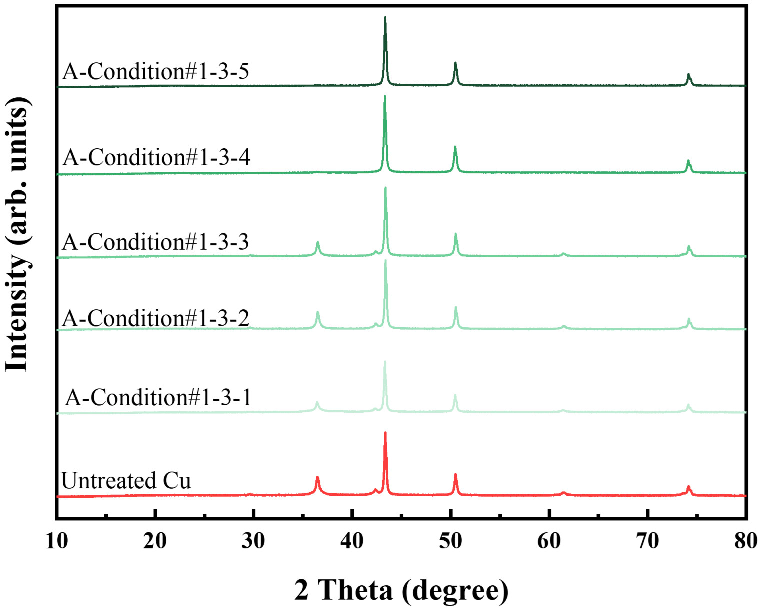

Figure B.3: XRD results for the Cu NPs treated by reductive agents A with treating condition 1-3-1, 1-3-2 and 1-3-3.

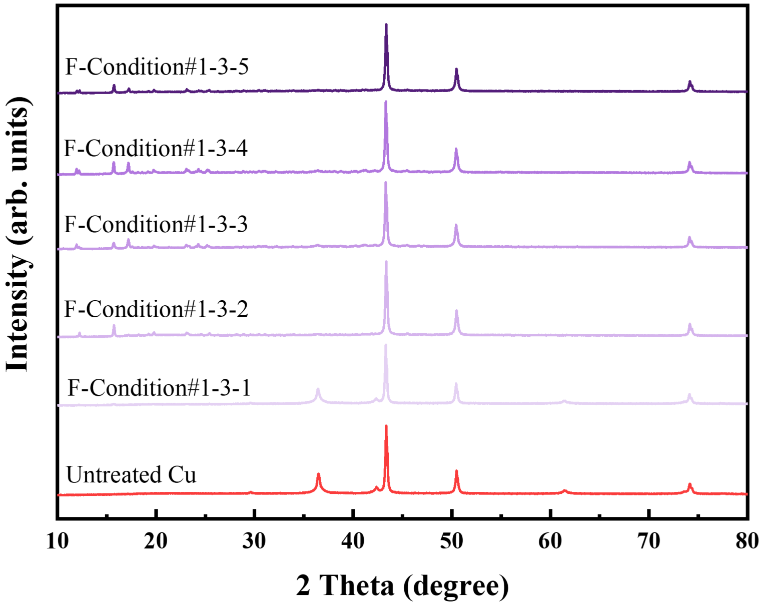

Figure B.4: XRD results for the Cu NPs treated by reductive agents F with treating condition 1-3-1, 1-3-2 and 1-3-3.

THE RESISTIVITY RESULTS

Table B.1: Resistivity of the Cu-sintered parts (Bulk copper as a reference: 1.72 $\mu\Omega \cdot$ cm)

Sample	R($\mu\Omega \cdot$ cm)	sta.dev.
250-3-5	17.398	0.04
250-3-10	4.066	0.02
250-3-20	4.37	0.02
250-3-30	3.15	0.01
250-1-20	362	17
250-2-20	6.87	0.02
250-4-20	3.91	0.02
210-3-20	8.084	0.04
230-3-20	6.726	0.01
270-3-20	3.55	0.03

THE SHEAR STRENGTH OF CU-SINTERED DA SAMPLES ON DIFFERENT METALLIC FINISHES

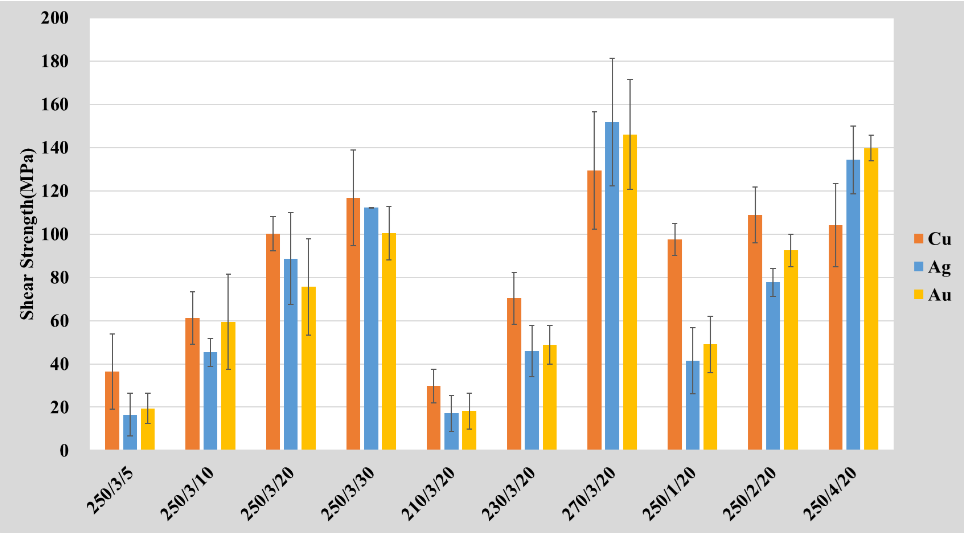

Figure B.5: The shear strength results for the samples sintered on the Cu, Ag and Au coated substrate.

C

SUPPORTING INFORMATION CHAPTER 4

CONSTITUTIVE EQUATIONS OF AG-SINTERED MATERIALS

As a comparison with sintered copper, the work of Zhang, et al.[1] was shown here. In his study, the nanoindentation characterization of nano-silver sintered joints prepared under different pressure conditions was performed and the following constitutive equations at room temperature were obtained. The testing conditions were with 5 mN of peak load and 0.2 s^{-1} of strain rate.

$$\sigma_{10MPa} = \begin{cases} 39.93\varepsilon(\sigma \leq 0.33GPa) \\ 0.33\left(1+122.65\varepsilon_p\right)^{0.47}(\sigma > 0.33GPa) \end{cases} \tag{C.1}$$

$$\sigma_{20MPa} = \begin{cases} 66.73\varepsilon(\sigma \leq 0.64GPa) \\ 0.64\left(1+104.64\varepsilon_p\right)^{0.48}(\sigma > 0.64GPa) \end{cases} \tag{C.2}$$

$$\sigma_{30MPa} = \begin{cases} 81.93\varepsilon(\sigma \leq 0.0.67GPa) \\ 0.67\left(1+122.69\varepsilon_p\right)^{0.48}(\sigma > 0.67GPa) \end{cases} \tag{C.3}$$

---

[1] Zhang, Hao, et al. "Indentation hardness, plasticity and initial creep properties of nanosilver sintered joint." Results in Physics 12 (2019): 712-717.

D

SUPPORTING INFORMATION CHAPTER 5

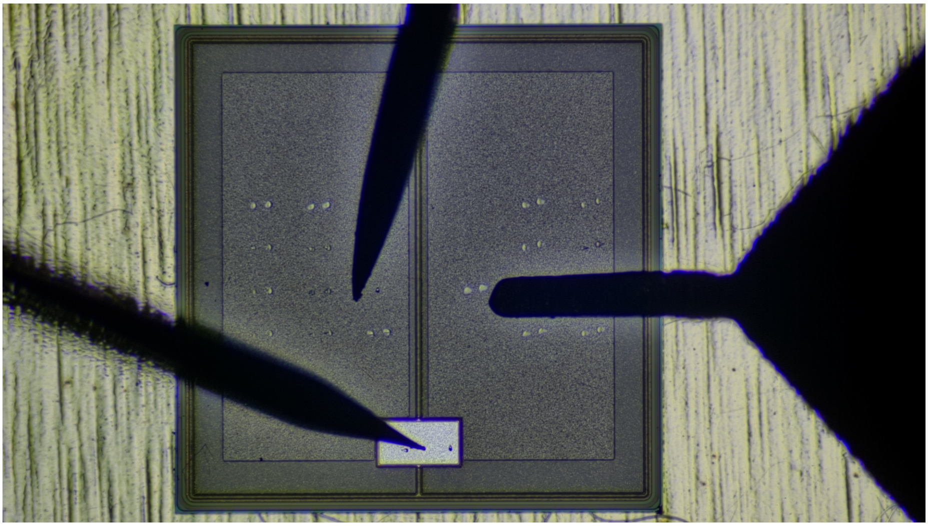

Figure D.1: The SiC chip under probe testing.

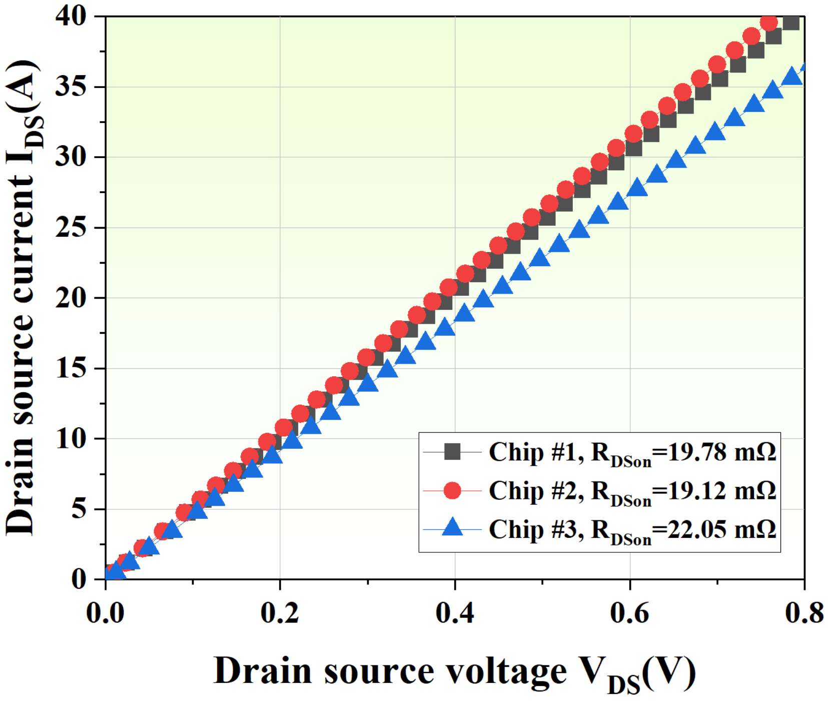

Figure D.2: The I-V curves for the SiC chips.

ACKNOWLEDGEMENTS

After four of the most magical years in human history, my PhD journey has come to an end. It has definitely been a memorable journey, as the process has been full of changes and challenges, but I have been fortunate to gain many experiences and achievements with the help of many excellent peers. I believe that I could not have accomplished these objects without their help, and I would like to express my most sincere gratitude to these wonderful people who have helped me.

First of all, I would like to express my most sincere gratitude to my promotor, Prof. Guoqi Zhang, for giving me the opportunity to pursue my PhD at Delft University of Technology. His passion, meticulousness, and critical spirit for research and work have profoundly influenced me during my PhD career. He has a unique vision and broad impact on the semiconductor industry.In the early stage of my PhD career, he suggested that I combine creative thinking with engineering methods to explore materials science and power electronics breakthroughs, which became my goal during my PhD career. With his encouragement, I became actively involved in numerous research projects in universities and industries. He was not only a supervisor, but also a role model in my life. It is my honor to have had the chance to study under his supervision.

I would like to dedicate my sincere gratitude to my other promotor, Prof. dr. Huaiyu Ye. As a mentor, he is full of innovative ideas in our research project. During his guidance, he gave me a lot of valuable suggestions on scientific research and project cooperation. In my daily work, he was very encouraging for me to come up with my ideas and put them into practice. When I met with project difficulties, no matter the time or distance, he was always willing to provide me with the best support I needed. I always remember the moment when we built the lab from scratch, recruited team members, and finished the team's first copper sintered sample. Without his guidance and persistent help, this project and dissertation would not have been possible.

I'm very grateful to my co-promotor, Prof. J.A. Ferreira. Thank you for your guidance on my preliminary research. He raised many valuable questions and suggestions on the innovative ideas, scientific problems and industrial value of my doctoral project, which triggered my thinking on the research methods. He was also a humble, easygoing mentor. Every conversation with him was joyous and relaxed.

I am very grateful to my academic supervisor, Prof. Jiajie Fan from the Fudan University, for his guidance and inspiration in my research. He organized the research teams with outstanding students from China and TU Delft to conduct research on power electronics, nano copper reliability and material simulation. He continuously shares industry news, academic achievements and cooperation opportunities to the team, and encourages everyone to collaborate. It was my pleasure to work with the wonderful members in these teams.

It was my pleasure to work with my brilliant colleagues in Nano Cu group in ECTM: Dong Hu, Xinrui Ji, Xiao Hu, Joost van Ginkel, and recently we also have Max Mastrangeli and Ahmed Abdelwahab. We established this team in 2020, and from that moment we had the opportunity to gather colleagues from multidisciplinary backgrounds and come up with more interesting ideas. We shared our expertise and resources from different labs, different companies and even different countries. I would like to thank Dong Hu for his assistance with material validation on discrete device, the thermal impedance test, the dip method, and so on. He also shared lots of knowledge on material science, semiconductor packaging and molecular dynamics simulation with me. I was very happy to cooperate with him. I would also like to thank Xinrui Ji, for testing the feasibility of my material in microelectronics packaging application. Thanks for sharing me with the fancy lift-off process. I would also thank Xiao Hu and Joost van Ginkel for their discussion on thermal conductivity mechanism, testing methods, nanoparticle generator and so on. From each time of our discussion, I learnt a lot from you.

I am fortunate that I have worked in several research groups. It was also my pleasure to work with my brilliant colleagues in SUSTECH: Chunjian Tan, Shaogang Wang, Shizhen Li, Qianming Huang, Xu Zhao, Xiaoli, Zhuolei Han, Ouyang, Hai Chi, Chenshan Gao, Huiru Yang, Quan Zhou, Qipeng Liu. I did most of my work here during my research in China. It was a very awesome group. I would like to thank Chunjian for the cooperation on our huge or tiny projects. We completed a lot of challenging projects and I believe we will have more collaborations in the future. I thank Shaogang and his team members for teaching me fundamental semiconductor and electronics knowledge and testing methods. I was very happy to cooperate with him. I want to thank Shizhen for your dedication on our collaborative works. Your hardworking also influenced me a lot. I would also like to thank my lovely teammates, Xu, Zhuolei, Xiaoli and Ouyang. We've been through a lot of lows and highs together. Without everyone's joint efforts, our project could not have been completed.

It was my pleasure to work with my brilliant colleagues online or face-to-face in ECTM: Prof. dr. Lina Sarro, Dr. Willem van Driel, Dr. Rene Poelma, Dr. Hongyu Tang, Dr. Fengze Hou, Dr. Jianwen Sun, Dr. Zhen Cui, Dr. Hao Zhang, Dr. Boyao Zhang, Dr. Bo Sun, Dr. Amir Mirza, Dr. Leandro Sacco, Dr. Lucas Middelburg, Dr. Aleksandar Jovic, Ziqiao Huang, Jiarui Mo, Hande Aydogmus, Milica Dostanic, Tianyi Jing, Leo Guo, Paul Motreuil-Ragot, Joost van Ginkel, Zichuan Li, Hongzhi Du, Joost Romijn. I would like to thank all other professors, PhDs, post-docs, master students, and technicians inside or outside our department for their presentations, feedback, cooperation, help, and friendship.

My sincere thanks go to my friends, who helped me a lot during this four years. You gave me a lot of guidance in my major, career choice and life, you are also my role models: Dr. Jing Zhang, Dr. Pan Liu, Dr. Wenbo Wang, Mr. Jun Li, Ms. Yan Li. Many thanks to my best friends, Xiao Shen, Dong Zhao, Chenshan Gao, Yuchen Wei, Gela Teng, Lu Yang, Peng Li, Yang Zhang, Te Bo, Cheng Gu, Yiqiao Xiao. You are always supporting me and trusting me.

I would like to give special thanks to my wife, Xiazi, who is always there for me when I needed her most. Her optimism, kindness, sense of humor, enthusiasm for life, understanding for me, unwavering love for me, are the most valuable wealth in my life. I also want to thank my big family, whose integrity, filial piety and humility have influenced me since childhood. This is a loving family. During my study, they have always cared about my life and mood and they provided me with a lot of help to overcome the troubles I met. I would also like to thank my parents, who have been supporting me throughout my life. Whenever I meet with difficulties on work or life, they are always the first to support me and encourage me. I want to thank them for their unconditional support since I left my hometown early to study in Beijing, Germany, the Netherlands and Shenzhen. I cannot accomplish this difficult task without your love.

Curriculum Vitæ

Xu Liu

12-06-1992	Born in Inner Mongolia, China.

Education

2011–2015	Bachelor of Material Physics University of Science and Technology Beijing, China Thesis: Study of 2D MoS_2 on the SiO_2 substrate
2015–2018	Master of Science RWTH Aachen University, Germany Thesis: Study on the adhesion between thick film and Si_3N_4 substrate Promotor: Prof. Dr. rer. nat. Rainer Telle
2018–2022	PhD. in Microelectronics Delft University of Technology, the Netherlands Pressure-assisted Cu Sintering for SiC Die-attachment Application Promotor: Prof.dr.G.Q.Zhang

Project Experience

2018–2022	Southern University of Science and Technology, Shenzhen, China Key-Area R&D Program of GuangDong: Cu Sintering for Power Electronics
2020–2022	Southern University of Science and Technology, Shenzhen, China National Key R&D Program of China: Foundamental and in-depth Study
2017–2018	Heraeus Electronics, Hanau, Germany Innovation and in-depth Study of AMB Power Substrate
2017	Heraeus Electronics, Hanau, Germany Innovation of Power Substrate

LIST OF PUBLICATIONS

JOURNAL PAPERS

1. **X. Liu**, S. Li, J. Fan, J. Jiang, Y. Liu, H. Ye, & G. Zhang, *Microstructural evolution and bonding mechanisms of nano copper sintering for power electronics packaging industrial application*, Journal of Materials Research and Technology **19**, 1407 (2022).

2. **X. Liu**, S. Li, C. Tan, C. Gao, Y. Liu, H. Ye, & G. Zhang, *Coalescence kinetics and microstructure evolution of Cu nanoparticles sintering on substrates: a molecular dynamics study*, Journal of Materials Research and Technology **17**, 1132 (2022).

3. J. Chen, **X. Liu**, X. Zeng, H. Ye, & G. Zhang, *A facile method to prepare oriented boron nitride-based polymer composite with enhanced thermal conductivity and mechanical properties*, Composites Communications **29**, 101038 (2022).

4. C. Gao, **X. Liu**, H. Yang, Q. Zhou, Y. Zhang, A. Yang, H. Ye, Y. Liu, L. Zhang, & G. Zhang, *A theoretical study of Ti-$MoSe_2$ as a noninvasive type-1 diabetes diagnosis material for detecting acetone from exhaled breath*, Vacuum **182**, 109729 (2020).

5. R. Sattari, D. Hu, **X. Liu**, H. van Zeijl, S. Vollebregt, & G. Zhang, *Transient thermal measurement on nano-metallic sintered die-attach joints using a thermal test chip*, Applied Thermal Engineering, **Available online**, 119503 (2022).

6. **X. Liu**, S. Wang, D. Hu, P, French, H. Ye, & G. Zhang, *Pressure-assisted Cu sintering die-attach at low temperature for SiC power electronics packaging*, IEEE Transactions on Power Electronics, Under review.

CONFERENCE PAPERS

1. **X. Liu**, Q. Zhou, X. Zhao, S. Koh, H. Ye, & G. Zhang, *Study and application of nano copper sintering technology in power electronics packaging*, In 2021 71st IEEE Electronic Components and Technology Conference (ECTC), San Diego, CA, 1928 (2021).

2. **X. Liu**, Q. Zhou, Q. Liu, H. Tang, C. Gao, B. Xie, S. Koh, H. Ye, & G. Zhang, *Study on the effect of mixing proportion of micro- and nano-copper particles on sintering properties*, In 2020 21st International Conference on Electronic Packaging Technology (ICEPT), Guangzhou, China, 1 (2020).

3. S. Zhen, **X. Liu**, J. Jiang, C. Tan, C. Gao, Y. Liu, H. Ye, & G. Zhang, *Effects of shell thickness on the thermal stability of Cu-Ag core-shell nanoparticles: a molecular dynamics study*, In 2022 23rd International Conference on Thermal, Mechanical and Multi-Physics Simulation and Experiments in Microelectronics and Microsystems (EuroSimE), St Julian, Malta.

4. C. Zhang, **X. Liu**, J. Li, G. Song, & H. Ye, *Simulation Study on Thermal Mechanical Properties of Different Embedded Packaging Structures and Materials of GaN Devices*, In 2020 21st International Conference on Electronic Packaging Technology (ICEPT), Guangzhou, China.

5. C. Tan, S. Wang, **X. Liu**, J. Jiang, H. Ye, & G. Zhang, *High-Voltage and High-Current IGBT Press-pack Module for Power Grid*, In 2022 23rd International Conference on Thermal, Mechanical and Multi-Physics Simulation and Experiments in Microelectronics and Microsystems (EuroSimE), St Julian, Malta.

6. X. Ji, H. Zeijl, J. Romijn, J. Ginkel, **X. Liu**, & G. Zhang, *Low Temperature Sapphire to Silicon Flip Chip Interconnects by Copper Nanoparticle Sintering*, In 2022 IEEE 9th Electronics System-Integration Technology Conference (ESTC), Sibiu, Romania.

7. **X. Liu**, S. Wang, H. Chi, D. Hu, Q. Huang, H. Ye, & G. Zhang, *Mechanical, electrical and thermal reliability analysis of Cu sintered die-attach SiC power device*,In 2023 73rd IEEE Electronic Components and Technology Conference (ECTC), Orlando, Florida, accepted.

8. D. Hu, A. Roshanghias, **X. Liu**, E. Bruin, S. Vollebregt, J. Fan, T. Basler, & Guoqi Zhang, *Reliability analysis on Ag and Cu nanoparticles sintered discrete power device with various frontside and backside interconnect*,In 2023 73rd IEEE Electronic Components and Technology Conference (ECTC), Orlando, Florida, accepted.

PATENTS

1. **X. Liu**, H. Ye, W. Zhang, G. Aori, J. Li, G. Zhang, *Nano metal film module preparation method and substrate preparation method thereof*, WO PCT **WO2020215739A1**, 2020.

2. **X. Liu**, H. Ye, W. Zhang, G. Aori, J. Li, F. Han, G. Zhang, *Chip interconnection structure and preparation method therefor* , WO PCT **WO2020215738A1**, 2020.

3. **X. Liu**, H. Ye, G. Zhang, *Multi-size mixed nano-particle paste and preparation method thereof*, WO PCT **WO2020199637A1**, 2019.

4. **X. Liu**, H. Ye, G. Zhang, *A kind of nanoporous metal membrane Prefabricated block and preparation method thereof*, CN **CN109979905A**, 2019.

5. **X. Liu**, H. Ye, T. Tian, G. Zhang, *Clamp system for packaging power device*, CN **CN112053973A**, 2020.

6. **X. Liu**, H. Ye, T. Tan, G. Zhang, *Newly developed pressure-assisted sintering equipment for packaging power device*, CN **CN112071775A**, 2020.

7. **X. Liu**, H. Ye, G. Aori, G. Zhang, *Preparation method of embedded packaging device*, CN **CN112768362A**, 2020.

8. H. Ye, **X. Liu**, G. Zhang, *Multi-sized nanoparticle mixed metal film and manufacturing method therefor*, WO PCT **WO2020199638A1**, 2019.

9. W. Zhang, **X. Liu**, G. Aori, H. Ye, G. Zhang, *Low-temperature sintering copper paste and sintering process thereof*, CN **CN110202137B**, 2019.

STANDARDS

1. **X. Liu**, et al., *Test method for thermal conductivity of micro-nano sintered compact: laser flash method*, **T/CASAS 020-2021**.

2. **X. Liu**, et al., *Test method for resistivity of micro and nano metal sintered compact: four probe method*, **T/CASAS 019-2021**.

3. **X. Liu**, et al., *Test method for shear strength of micro and nano metal sintered joints*, **T/CASA 018-2021**.

4. **X. Liu**, et al., *Terminology of micro-nano metallic sintering technology for wide-bandgap semiconductor*, **T/CASAS 0117-2021**.